Title
Resolving Non-Adiabatic Dynamics in Small Molecules with Few-Femtosecond Sensitivity

Author
Champenois, Elio Gilbert

Publication Date
2017

Peer reviewed|Thesis/dissertation

Resolving Non-Adiabatic Dynamics in Small Molecules with Few-Femtosecond Sensitivity

by

Elio Gilbert Champenois

A dissertation submitted in partial satisfaction of the

requirements for the degree of

Doctor of Philosophy

in

Applied Science & Technology

in the

Graduate Division

of the

University of California, Berkeley

Committee in charge:

Professor Roger Falcone, Chair
Professor David Attwood
Professor Daniel Neumark

Fall 2017

Resolving Non-Adiabatic Dynamics in Small Molecules with Few-Femtosecond Sensitivity

Abstract

Resolving Non-Adiabatic Dynamics in Small Molecules with Few-Femtosecond Sensitivity

by

Elio Gilbert Champenois

Doctor of Philosophy in Applied Science & Technology

University of California, Berkeley

Professor Roger Falcone, Chair

The molecules that make up the world around us display large responses to the ultraviolet (UV), vacuum ultraviolet (VUV), and extreme ultraviolet (XUV) region of the electromagnetic spectrum, and the absorption of this light can serve as a catalyst for chemistry. In these ultrafast photochemical reactions, the motion of the nuclei following excitation often enables electronic relaxation that facilitates further rearrangements such as dissociation or isomerization. In some small molecular systems, including ethylene and methanol, such effects become important on the sub-10 femtosecond time scale. Although several time-resolved spectroscopic tools, including transient absorption, Raman spectroscopy, and photoion or photoelectron imaging, have enabled the study of many photochemical reactions, resolving the evolution of an initially excited vibrational wavepacket on these short time scales has proved difficult. This thesis discusses an approach to studying sub-angstrom nuclear motion and non-adiabatic dynamics that follow photoexcitation with few-femtosecond sensitivity by quantifying dynamical spectral shifts in time-resolved photoelectron spectra (TRPES) obtained with ultrafast pump and probe light pulses in the VUV/XUV.

The laser system, beamline, and experimental end station are described in detail. Using a state-of-the-art 1 TW peak power, 30 W average power infrared laser, we implement a bright source of VUV/XUV light, based on high harmonic generation and needed for pump-probe spectroscopy. This source can deliver high energy ultrafast pulses in the VUV region allowing for efficient excitation of gas phase molecular targets at a 1 kHz repetition rate. The evolution of this prepared excited population can be followed through subsequent perturbative photoionization with another high energy photon. Separation of the light spectrally and temporally into pump and probe pulses with filters and a split-mirror interferometer is discussed. Time-resolved photoelectron and photoion imaging experiments are conducted using a velocity map imaging spectrometer optimized for VUV/XUV pump-probe measurements.

Ultrafast dynamics following excitation with the 5^{th} harmonic at 156 nm in ethylene (C_2H_4) to the $\pi\pi^*$ state and in methanol (CH_3OH) to the 2 ^{1}A" state are studied. In ethylene, photoexcitation has been predicted to lead to torsion of the molecule from its initial planar geometry to a fully twisted configuration in $\sim$10 fs. By examining small changes

in the onset time of signal at different photoelectron kinetic energies in the TRPES, this torsional motion is resolved experimentally with few-femtosecond sensitivity. The transient population of the low-lying π3s Rydberg state, predicted to be enabled by this torsional motion, is also observed. In methanol, the ultrafast relaxation and dissociation dynamics following excitation are studied through combination of the experimental TRPES with theoretical calculations of the energies of the first few excited states along two identified reaction pathways. We resolve sub-angstrom C–O bond stretching leading to a conical intersection within 15 fs of excitation.

Pour papa et maman

Contents

List of Figures

List of Tables

Acknowledgments

None of this work would have been possible without the help and support of many people throughout my graduate studies. After my brief stint in several mostly operational laser labs, my advisors Ali Belkacem and Roger Falcone gave me an invaluable opportunity to learn by building and operating an entire lab from scratch and by working at the wonderful Lawrence Berkeley National Laboratory with excellent scientists with expertise in every field imaginable. I am amazed by and grateful for their uncanny ability to immediately extract and appreciate the key aspects pertaining to something I had been working on for weeks and to make use of their vast experimental experience to give me actionable advice. I have also appreciated their constant consideration and reminder of the "bigger picture" that is often lost day to day working on an experimental setup. I am also thankful to Professor Dave Attwood, whose role for me evolved from a caring and always personable academic advisor, to a world-leading resource on XUV and X-ray science, and, finally, back to an advisor, this time on career paths. I am grateful for all of the help, much of which I assume I didn't even witness since it was behind the scenes, I've received from Yeen Mankin, Pat Berumen, and Ariana Castro, who got me through all of the hoops of graduate school.

I am indebted to all of my coworkers over the years, who have taught me the vast majority of the skills and knowledge that I have gained throughout graduate school while also making my time in the lab enjoyable. From laser alignment to beamline hardware assembly to science discussions, James Cryan was an amazing mentor and teacher on all fronts for my first few years, always willing to take a step back to the white board. Rafal Rakowski and Champak Khurmi taught me much of what I know about high harmonic generation and showed me that it takes a lot of time and manual labor, both with pen and paper and with mirror knobs and pressure valves, to get it working properly. Niranjan Shivaram brought a fresh set of experimental ideas, experience and tutelage in fields of ultrafast science I had not yet been in contact with, and an inspiring work ethic that shows itself in the constant evolution and improvement as well as high uptime (despite broken pump lasers, air handling, or water supply) of the lab since he joined us. I am also thankful for my time working with Travis Wright. He taught me a lot from first hand experience about working with an XUV beamline and did the bulk of the design for the spectrometer that enabled our science, all the while staying positive and cheerful, through highs and lows.

Working with other students has been a great experience, as nothing beats learning alongside your peers. I will always fondly remember my time in the laser labs or at the ALS with Felix Sturm, Neal Yang, Alison Saunders, Kirk Larsen, Ave Gatton, and Saijoscha Heck. Brant Abeln and Zach Streeter were also great to overlap with, always willing to trade their theoretical viewpoints for my experimental one, or to talk about football. Scott Ellis, Kenny Gotlieb, Kasra Nowrouzi, and Camila Bacellar were also a great source of support and knowledge outside of the AMOS group.

I am thankful for many scientists at LBNL. Dan Slaughter and Thorsten Weber gave me several opportunities to branch out as a scientist through collaboration and always used their influence to move the group in a direction benefiting everyone. Bill McCurdy, Tom

Rescigno, Dan Haxton, Loren Greenman, and Robert Lucchese were always available and willing to offer their scientific knowledge and theoretical expertise to answer my vast amount of questions. I want to personally thank Loren for all of the work he put in to help make sense of the methanol experiments and also helping me get up to speed and comfortable with using quantum chemistry codes.

I am particularly thankful for my friends outside of graduate school who have kept me going. I acknowledge all who have joined me on the soccer pitch and helped keep me mentally healthy by chasing a ball on a grass field a few times a week. Finally, I am indebted to my siblings, Flora, Lucas, and Bianca, for always being there for me and giving me great perspective, and to my parents, for the many opportunities, unequivocal support, and unconditional love they have given me.

Chapter 1

Ultrafast Molecular Photodynamics

Humanity has experienced exponential growth over the last few centuries in terms of both population, economy, and technology. Energy has played a central role in this development: enabling it only due to levels of its production (and consumption) growing at similar or even greater rates. Our main sources of energy have been from resources with a finite supply on Earth, including petroleum, natural gas, coal, and uranium, with only a small portion coming sources deemed renewable [1]. According to many estimates, our rate of consumption has already exceeded that allowed by our planet: Earth Overshoot Day, on which the global human ecological footprint surpassed the estimated Earth's yearly capacity to regenerate planetary energy resources, occurred on August 2^{nd} this year[2]. Technological advancement has the ability to address this issue through the development of novel or more efficient methods for harvesting renewable energy.

One currently underutilized source, accounting for less than 1% of total consumption [1], is solar energy. The total power of the sun's light impinging on Earth is several orders of magnitude larger than our current rate of energy consumption. But sunlight contributes much more than our direct usage in photovoltaics and thermal sources. On top of allowing us to see the world we live in, photons from the sun power much of the natural world around us: photosynthesis, with which plants and other organisms acquire and chemically store energy, is possible due to chemical reactions initiated by the absorption of light [3]. Large efforts are currently underway to design systems emulating photosynthesis in a power and cost-effective way, with the hope of revolutionizing our energy industry [4].

Chemistry driven by light is not isolated to photosynthesis, however. From atoms, to isolated molecules, to liquids, to solids, everything in and around us absorbs light. While the energy associated with this absorption can be lost just as it was gained through fluorescence, in many cases, it is instead converted to other forms of energy by initiating changes in the system that absorbed it. Such photochemical reactions play an important role in a wide array of areas, ranging from atmospheric chemistry and energy storage [5] to human vision [6], and therefore studying and understanding them is of great significance.

In the remainder of this chapter, I will introduce the molecular physics framework that we will turn to to first ask and then try to answer questions about these photochemical

reactions.

1.1 Reaction Pathways: From the Kinetic Picture to Molecular Dynamics

At the coarsest level, a chemical reaction can be described as the process by which certain input species (or reactants, here A and B) are transformed into different output species (or products, here C and D) via the forming and/or breaking of chemical bonds:

$$A + B \rightarrow C + D. \tag{1.1}$$

Taking the proper identification of these products and reactants as a given, a simple observation of this forward process is all that is needed to recognize such a reaction. However, beyond this simple representation lies much more, especially if we would like to answer the fundamental question, "Why and how does this reaction proceed?"

The first additional detail that should be considered is whether or not a certain reaction can further be broken down as the sequential combination of two or more reactions. Since these can be used to reconstruct the original reaction, it can be argued that they are more fundamental. Understanding of these separately can be combined to understand the original system. The identification of these so called transient states of the system, which act as a bridge from the reactants to the products, is in general not trivial, but is crucial to learning about and eventually describing the mechanisms that allow for the original reaction to occur.

Next, we should consider energy: Is energy required for a reaction to proceed? Does the reaction result in excess energy? In either case, in what form is this energy found? The endo- or exothermicity of the reaction gets part of the way to answering these questions and, along with a temperature, may be the best recourse when describing an ensemble. However, at the molecular level, energy can instead be directly included when labeling the reactants, transients, and products. Being explicit about the internal state of each specie (e.g. molecular vibrations or electronic excitations[1]) accurately represents internal energy. Translational kinetic energy is extracted by specifying body motions relative to some reference frame, while potential energy can typically be excluded by choosing asymptotically large relative positions. External sources of energy, such as a photon, can simply be treated as an additional unique specie.

Finally, since these reactions will proceed in time, it is important to consider this time evolution. Gaining knowledge of the time scale on which each individual reaction occurs can help predict or explain what is observed in the above case of multiple sequential reactions. This becomes even more important when considering a system in which there are multiple reactions possible all starting with the same reactants, as the fastest occurring pathway will dominate. As a simple yet general and powerful approximation, chemical kinetics assumes a stochastic behavior to model this time dependence[7]. This approach leads to the appearance

[1] See section 1.2

of rates for each step along a reaction pathway. Using these rates, we can build kinetic models for the reaction as a whole. Single molecule reactions initiated by interaction with light, which will be the point of study of most of this text, can thus be re-expressed, as a simple example, as:

$$AB + \hbar\omega \rightarrow AB^* \xrightarrow{k_1} A + B, \tag{1.2a}$$

$$\xrightarrow{k_2} AB \tag{1.2b}$$

where the molecule AB absorbs one photon $\hbar\omega$ leading to the electronically excited AB^* that eventually either dissociates into A and B with some released kinetic energy or relaxes back to the original AB state with some additional vibrational energy. Using chemical kinetics, an exponential decrease of the excited state population will be observed, with accompanying exponential increases in the two product channels. The final ratio of dissociated to bound final states will depend on the kinetic rates k_1 and k_2.

Validating these kinetic models is possible by validating the stochastic nature of these individual reaction steps. While simple chemical reactions are the building blocks for large scale biological or industrial processes, dynamics are the fundamental makeup of these reactions. The above kinetic treatment is powerful and, in general, accurate, especially when dealing with a system ensemble. However, it must miss part of the picture. We required, among other attributes, that the potential and kinetic energy of the system be specified at each step of a reaction. But these quantities, which depend on the positions and velocities of the individual species, evolve continuously rather than sequentially. Since the nuclei and electrons in a system are constantly adjusting to find their new equilibrium, we must go beyond this quasi-statistical approach and turn to molecular dynamics [8, 9].

1.2 The Molecular Hamiltonian and the Born-Oppenheimer Approximation

In order to formally study these reactions at this highly descriptive level, a framework is needed. Since it is the position and motion of nuclei and electrons that govern these molecular dynamics, we turn to a quantum mechanical treatment. To describe the state of a molecule, we seek a wavefunction which will depend on the positions of both the m electrons $\mathbf{r}_i$ ($i \in 1, m$) and n nuclei $\mathbf{R}_k$ ($k \in 1, n$) in the system:

$$\Psi(t) = \Psi(\mathbf{r}_1, \mathbf{r}_2, ..., \mathbf{r}_m, \mathbf{R}_1, \mathbf{R}_2, ..., \mathbf{R}_n; t), \tag{1.3}$$

and which we can expand as a combination of eigenstates to the molecular Hamiltonian that will show up in the Schrödinger equation:

$$\hat{\mathrm{H}}_{mol}\Psi = E\Psi \tag{1.4a}$$

$$\hat{\mathrm{H}}_{mol} = \sum_{k}^{n} -\frac{\hbar^2\nabla_k^2}{2M_k} + \sum_{l>k}^{n} \frac{Z_k Z_l e^2}{4\pi\epsilon_0|R_k - R_l|} + \sum_{i}^{m} -\frac{\hbar^2\nabla_i^2}{2m_e} + \sum_{j>i}^{m} \frac{e^2}{4\pi\epsilon_0|r_i - r_j|} + \sum_{ik}^{mn} -\frac{Z_j e^2}{4\pi\epsilon_0|r_i - R_k|} \tag{1.4b}$$

$$= \hat{\mathrm{T}}_N + \hat{\mathrm{V}}_N + \hat{\mathrm{T}}_e + \hat{\mathrm{V}}_e + \hat{\mathrm{V}}_{eN}. \tag{1.4c}$$

Here M_k and Z_k are the mass and charge, respectively, of the k-th nucleus while m_e and e are the mass and charge of the electron. Although this equation is known, both analytical and numerical solutions are out of reach for all but the smallest of molecules with very few electrons[10]. The problem becomes much more tractable by assuming that the wavefuntion can be separated into a part that depends solely on the nuclear coordinates and an electronic part that depends on the electronic coordinates but only parametrically on these nuclear coordinates:

$$\Psi(r, R) = \chi(R)\psi(r; R), \tag{1.5}$$

where r and R now denote the combination of all of the electronic and nuclear coordinates, respectively[2]. This assumption, often called the Born-Oppenheimer approximation, relies on and is justified by the adiabaticity of the electronic part of the problem with respect to changes in the nuclear geometry. Since the electrons are several orders of magnitude lighter than the nuclei but feel similar forces, they should be able to quickly rearrange themselves in order to remain in their instantaneous eigenstate ψ given any small change in the positions of the nuclei. After making this approximation, the electronic eigenfunctions and the associated electronic spectrum may be found for a given frozen nuclear geometry R by solving the electronic part of the Schrödinger equation:

$$\hat{\mathrm{H}}_e\psi_i(r; R) = (\hat{\mathrm{T}}_e + \hat{\mathrm{V}}_e + \hat{\mathrm{V}}_{eN})\psi_i(r; R) = E_i(R)\psi_i(r; R). \tag{1.6}$$

Again, solving this equation for systems with even just a few electrons is out of reach due in part to the need for an antisymmetrized wavefunction and the exponential scaling that it implies. However, a variety of approaches have been and are actively being developed to find approximate solutions [11, 12, 13, 14, 15, 16]. The field of quantum chemistry, which encompasses these methods, is mature enough that many implementations are readily available [17].

Armed with the electronic spectrum $E_i(R)$ at each nuclear geometry, we can now approach the nuclear part of the problem. The total potential energy of the system as a function of nuclear geometry can be calculated by adding to this electronic energy the nuclear

[2]Note that the electronic wavefunction $\psi(r; R)$ must also include information about electronic spin.

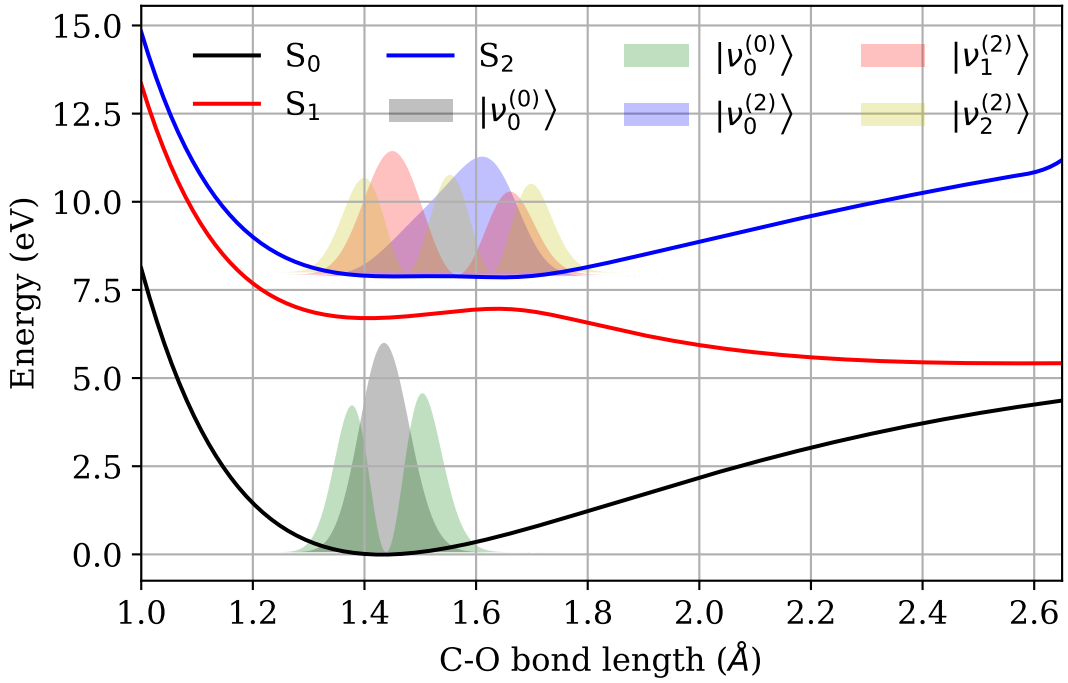

Figure 1.1: **One-dimensional PES cut.** A cut along the C–O bond coordinate of the high dimensional PES for the ground state (S_0, black) and first two excited states (S_1, red, and S_2, blue) of methanol. The ground state has a minimum in energy which corresponds to the equilibrium geometry of the molecule. S_1 is a dissociative state, since the lowest energy configuration is at diverging bond distances. On the bound states S_0 and S_2, several vibrational eigenstates have been calculated in the one dimensional approximation. This approximation will need only slight corrections on the ground state since this C–O bond stretch mode is roughly normal, while the excited state nuclear wavefunctions will need more corrections. The excited state energies were calculated using an equation-of-motion coupled cluster (EOM-CCSD) calculation using GAMESS [17], while the vibrational eigenstates were found by solving eq. (1.8) on a grid.

repulsion term dropped from eq. (1.4c):

$$V_i(R) = E_i(R) + V_N(R). \tag{1.7}$$

This term $V_i(R)$ visualized in the high dimensional space of all possible nuclear geometries is referred to as the potential energy surface (PES) for electronic state i. A one-dimensional example of the PES for several electronic states of methanol (CH_3OH) is shown in fig. 1.1. There are 3N-6=12 total internal coordinates in this molecule, making it necessary to take projections to visualize these PES on which we will solve our the nuclear part of the molecular

Schrödinger equation:

$$H_{iN}\chi(R) = \left[\hat{T}_N + V_i(R)\right]\chi(R) = E_{ij}\chi(R). \tag{1.8}$$

We can solve this equation and find either quantized states $|\nu_j^{(i)}(R)\rangle$ for a bound potential $V_i(R)$ or a continuum of states $|k_j^{(i)}(R)\rangle$ for an unbound potential. The former represents the vibrational states of the system, while the latter corresponds to dissociative states. Near the minimum of the PES of a given electronic state, this potential can be approximated by a multi-dimensional harmonic oscillator and the basis set of normal modes of vibration, which are uncoupled, can be extracted. Far away from this equilibrium geometry (or at this geometry but on the PES of a different electronic state), however, this basis set loses its significance as the various modes start to couple. There, instead, we can turn to the time-dependent version of eq. (1.8) to solve for nuclear wavepacket dynamics. Note that, although more feasible than the electronic problem, the nuclear Hamiltonian is also very highly dimensional making it difficult to approach head on.

These solutions $\Psi_i^k(r;R)$, with i representing the electronic state and k the vibrational state, to the molecular Hamiltonian in the Born-Oppenheimer approximation are also useful to understand the interaction of molecules with light. We can look at photo-absorption between two vibronic states $\Psi_i^k(r;R)$ and $\Psi_j^l(r;R)$[3] in the dipole approximation and get a transition probability amplitude P:

$$\begin{aligned}
P &\propto |\langle\Psi_i^k|\mu|\Psi_j^l\rangle|^2 && \text{(1.9a)}\\
&= |\langle\psi_i\chi_k^{(i)}|\mu|\psi_j\chi_l^{(j)}\rangle|^2 && \text{(1.9b)}\\
&= |\int \psi_i^*\chi_k^{(i)*}\mu\psi_j\chi_l^{(j)}drdR|^2 && \text{(1.9c)}\\
&\approx |\int \psi_i^*\mu_e\psi_j dr\int \chi_k^{(i)*}\chi_l^{(j)}dR + \int\psi_i^*\psi_j dr\int\chi_k^{(i)*}\mu_N\chi_l^{(j)}dR|^2, && \text{(1.9d)}
\end{aligned}$$

where the dependence of $\langle\psi_i|\mu|\psi_j\rangle$ on the nuclear geometry has been ignored[4] We recognize the first term as the electronic dipole matrix element, which will lead to the usual symmetry selection rules, and notice that the term $\int\psi_i^*\psi_j dr$ is null by orthogonality, leaving us with:

$$\begin{aligned}
P &\propto |\langle\psi_i|\mu_e|\psi_j\rangle\langle\chi_k^{(i)}|\chi_l^{(j)}\rangle|^2 && \text{(1.10a)}\\
&= |\langle\mu_e^{(ij)}\rangle S_{(ik),(jl)}|^2, && \text{(1.10b)}
\end{aligned}$$

where $S_{(ik),(jl)}$ is referred to as the Franck-Condon (FC) factor between the vibronic states $\Psi_i^k(r;R)$ and $\Psi_j^l(r;R)$. A non-negligible FC factor is needed for photo-absorption between

[3]For simplicity, we leave out spin and rotational information. Spin must be conserved, while rotational features are generally too low in energy to resolve.

[4]This is known as the Condon approximation and is valid to some order since this dependence is usually rather small and smooth.

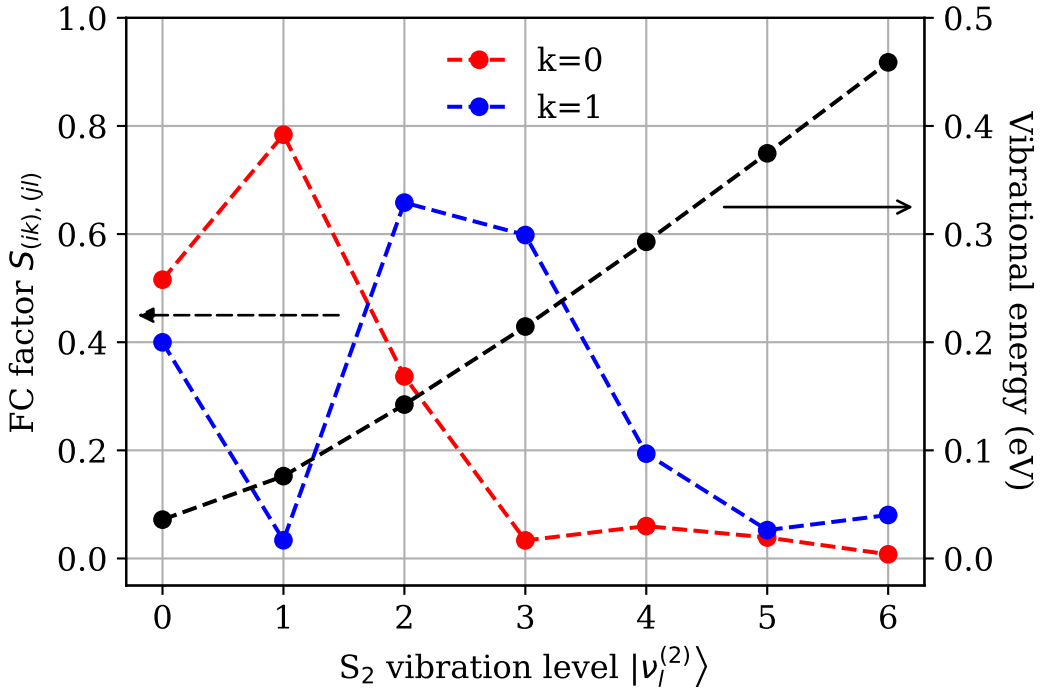

Figure 1.2: **FC factors for a vibronic excitation to S_2 in methanol.** The FC factors from initial vibrational states $k = 0$ (red) and $k = 1$ (blue) on S_0 of methanol to final vibrational states on S_2, plotted alongside the vibrational energies of these final vibrational states (black). Almost all of the FC overlap from $k = 0$ goes to the first three final vibrational states, which are only ∼100 meV apart. An excitation pulse would only require that much bandwidth to create a wavepacket almost completely localized to the FC region.

two vibronic states. Photo-ionization can also be treated in this same manner with a continuum electron wavefunction instead of a bound eigenstate. The FC factors between the first two vibrational states of the ground electronic state and first seven vibrational states of the second excited state of methanol (with only the C–O bond coordinate active) are shown in fig. 1.2. The sum of FC factors for a given initial state sum to 1 due to the vibrational states on the final state forming a complete orthonormal basis. We see that just the first three vibrational states of S_2 contain most of the FC overlap with the ground vibronic state of methanol. These FC factors are also used to understand photo-excitation with an ultrafast laser pulse: this pulse must have a large spectral bandwidth and may thus be resonant with multiple vibrational states, exciting them coherently and creating a vibrational wavepacket. Since each state is associated with its eigenenergy E_{ij}, the full time evolution of this excited

wavepacket can be predicted through the proper phase accumulation:

$$|\Psi(r,R;t)\rangle = \sum_{ik} c_{ik}|\psi_i(r;R)\chi_k^{(i)}(R)\rangle e^{iE_{ik}t/\hbar}, \tag{1.11}$$

where the coefficients c_{ik} can be found through appropriate first-order perturbation theory and eq. (1.10b) [18]. Again due to the vibrational states forming a complete orthonormal set, a pulse of negligible temporal width (i.e. a delta function in time), which must have spectral power at every energy, will form a copy of the initial vibrational state on the final electronic state PES. In practice this pulse is not feasible, but a short enough pulse will interact with the molecular system similarly. The space of nuclear geometries where the density of initial vibrational states is referred to as the FC region. Such a short pulse will initiate a wavepacket localized in this FC region. For short but not instantaneous pulses, eq. (1.11) is slightly complicated due to the additional time-dependence of the coefficients c_{ik} [18].

1.3 Beyond the Born-Oppenheimer Approximation

The Born-Oppenheimer approximation allows for the separation of the nuclear and electronic degrees of freedom and vastly simplifies the calculation of our molecular eigenstates. At the base, it relies on adiabaticity in the molecule: as the nuclei move slowly due to their large masses, the electrons can adjust instantaneously and remain in the same eigenstate. In quantum mechanical terms, these "motions" can be quantified with by characteristic frequencies $\omega \sim \sqrt{k/m}$, where k corresponds to some force constant in the harmonic approximation, or, alternatively, $\omega \sim \Delta E/\hbar$, where ΔE corresponds to the difference in energy between two beating eigenstates. In the first case, we find a frequency ratio between electrons and nuclei of $\omega_e/\omega_N \sim \sqrt{M_N/m_e}$, which will be on the order of 100 or larger. Looking at figs. 1.1 and 1.2, we find that the ground and first excited electronic states are split by several eV, while a typical vibrational spectrum will have a progression on the 100 meV scale, leading to a frequency ratio $\omega_e/\omega_N \sim \Delta E_e/\Delta E_N$ also on the order of 100. However, it may be possible to find geometries in the high dimensional space of nuclear configurations where the splitting of electronic levels becomes comparable or smaller than that of vibrational states. There, the electronic motion slows and the adiabatic approximation breaks down.

Going back to eq. (1.8), we see that another adiabatic approximation was made, notably that the nuclear kinetic energy operator did not operate on the electronic wavefunction:

$$\hat{T}_N\psi(r;R)\chi(R) \approx \psi(r;R)\hat{T}_N\chi(R). \tag{1.12}$$

The dropped terms will include derivatives of the electronic wavefunction with respect to the nuclear coordinates, which we can reinsert into the molecular Hamiltonian as perturbations, coupling together different molecular eigenstates and allowing for radiationless transitions between electronic states.

In most cases, only two electronic states (if any) will be close enough in energy to couple to each other efficiently, so we can rewrite our wavefunction as:

$$\Psi(r,R) = \chi_1(R)\psi_1(r;R) + \chi_2(R)\psi_2(r;R). \tag{1.13}$$

We require:

$$\left[\hat{\mathrm{H}}(r,R) - E\right]\Psi(r,R) = 0, \tag{1.14}$$

and find after switching to a matrix formulations and closing on the left side with $\langle\psi_i|$:

$$\begin{pmatrix} E_1(R) + \hat{\mathrm{T}}_N^{(11)}(R) & \hat{\mathrm{T}}_N^{(12)}(R) \\ \hat{\mathrm{T}}_N^{(21)}(R) & E_2(R) + \hat{\mathrm{T}}_N^{(22)}(R) \end{pmatrix} = E \begin{pmatrix} \chi_1(R) \\ \chi_2(R) \end{pmatrix}, \tag{1.15a}$$

$$\hat{\mathrm{T}}_N^{(ij)}(R) = \langle\psi_i(r;R)|\hat{\mathrm{T}}_N(R)|\psi_j(r;R)\rangle, \tag{1.15b}$$

where the integration is over the electronic degrees of freedom only. We can also find a new basis in which these terms disappear, notably:

$$\langle\psi_i(r;R)|\frac{\partial}{\partial R}|\psi_j(r;R)\rangle = \langle\psi_i(r;R)|\frac{\partial^2}{\partial R^2}|\psi_j(r;R)\rangle = 0. \tag{1.16}$$

This basis is found through a rotation of the original adiabatic electronic states $|\psi_i\rangle$ onto diabatic states $|\phi_i\rangle$:

$$\begin{pmatrix} \phi_1 \\ \phi_2 \end{pmatrix} = \begin{pmatrix} \cos\gamma(R) & \sin\gamma(R) \\ -\sin\gamma(R) & \cos\gamma(R) \end{pmatrix} \begin{pmatrix} \psi_1 \\ \psi_2 \end{pmatrix}. \tag{1.17}$$

After this transformation, we find that the coupling now arises due to terms of the form $\langle\phi_1|\hat{\mathrm{H}}_e|\phi_2\rangle$. For the one-dimensional case (i.e. for a diatomic molecule), we find that the diabatic state PES can cross, while that of the adiabatic states will show avoided crossings. Looking at the electronic state wavefunctions, we find that the character of the diabatic states will remain constant while that of the adiabatic states will rapidly change across the region where the diabatic states cross. The probability for a non-adiabatic transition between two states as this region is crossed was explored analytically by Landau and Zener [19, 20] by making use of both these adiabatic and diabatic representations and found to be:

$$P = e^{-2\pi\Gamma}, \tag{1.18a}$$

$$\Gamma = \frac{|a|^2}{\hbar|\alpha|}, \tag{1.18b}$$

where a is the off-diagonal coupling matrix element in the diabatic representation and $\alpha = \frac{\partial}{\partial t}(E_2 - E_1) = v\frac{\partial}{\partial R}(E_2 - E_1)$, where $v = \frac{\partial R}{\partial t}$ is the classical velocity of the molecule (i.e. the rate of change of the internuclear distance). At slow velocities, adiabaticity is achieved and there will be a low probability for transition. Transformation between these two representations is also useful as it gives two different options for computation of the coupling terms [21].

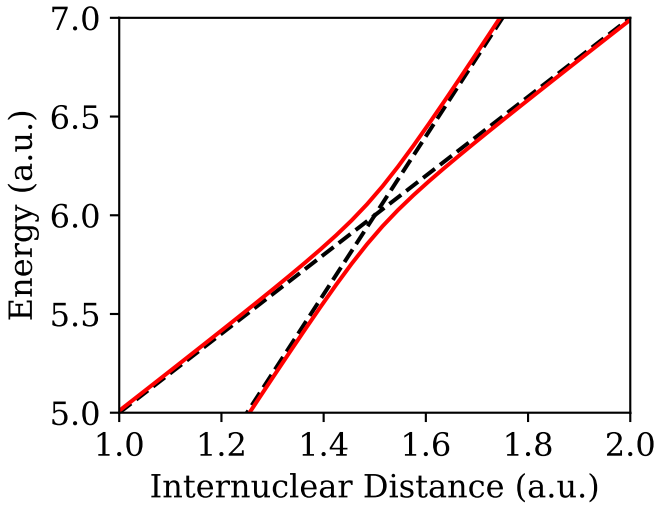

Figure 1.3: **Diabats and Adiabats of a Diatomic.** Example diabatic (black, dashed) and adiabatic (red, solid) electronic state energies for a diatomic molecule. Locally, the diabatic states, which will cross, can be approximated as linear. The size of the crossing depends on the strength of the coupling. Away from a crossing, the two representations will be identical, and the BO approximation is valid.

Going beyond the one-dimensional case, the adiabatic PESs can also cross. Although the next lowest dimensional molecule will be a triatomic with three internal degrees of freedom, it is simpler to visualize the PESs in two dimensions. fig. 1.4 shows the adiabatic energy states associated with a model molecule displaying a Jahn-Teller distortion [22], where a degeneracy of the two lowest electronic states due to a high symmetry is lifted as this symmetry is lifted, with one state reaching a more stable (that is, less energetic) configuration after rearrangement away from the symmetry. These points of degeneracy, called conical intersections, have been predicted since the early days of quantum mechanics [23], but it has not been until the last few decades that their widespread role in photochemistry has been appreciated [21, 24, 25].

At and around these conical intersections, the character of an adiabatic electronic state can change drastically, and the aforementioned couplings involving the derivatives of the electronic part of the wavefunction with respect to the nuclear coordinates can become large or even diverge, suggesting a complete breakdown of the Born-Oppenheimer approach. While such intersections are not generally found on the ground electronic state near the equilibrium geometry, they have been found to play a dominant role in the electronic relaxation of single molecules following photoexcitation [24], often out-competing fluorescence by several orders of magnitude. As such, they have been referred to as the excited state analogue of the transition state discussed in section 1.1. Electronic relaxation through conical intersections

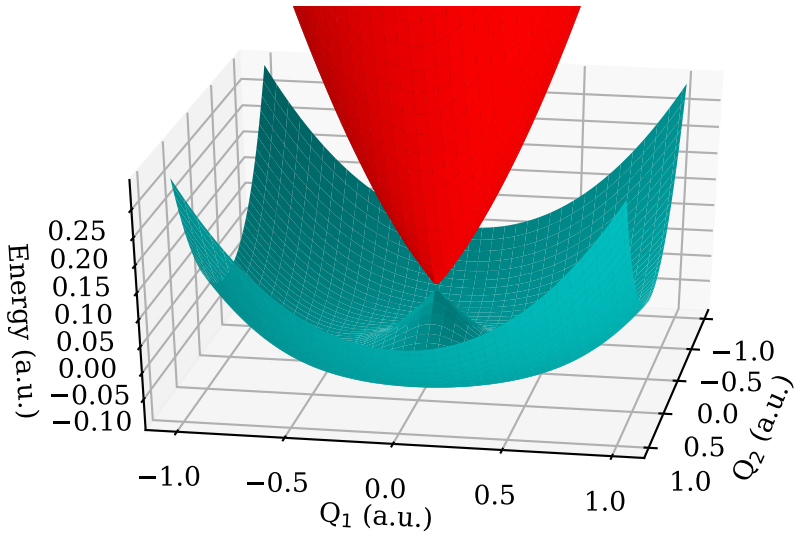

Figure 1.4: **Jahn-Teller distorted adiabatic states.** A conical intersection appears in the two-dimensional cut of low-lying excited states for molecules exhibiting Jahn-Teller distortions, where the coupling between two states leads to a new adiabatic ground state with a minimum away from the most symmetric geometry (Q_i=0).

has been identified as a crucial step in many biologically relevant photoreactions. DNA bases such as adenine are strong absorbers in the ultraviolet region of the spectrum, and electronic excitation leaves the molecules in a highly reactive state that can lead to damage should non-adiabatic relaxation not be possible [26]. Nature has also found these conical intersections useful to drive isomerization or dissociation reactions. As a famous example in the field of ultrafast science, the first step in vision involves isomerization of rhodopsin enabled by a conical intersection reached on the femtosecond time scale [6].

Like transition states, these conical intersections appear at geometries where the molecule is energetically unstable and are thus visited just briefly by an excited wavepacket. As a result, direct experimental study of concerted nuclear and electronic motion near these regions is difficult. As mentioned in section 1.1, final states and their branching ratios can be studied and their dependence on the nature of conical intersections assumed to be involved can be inferred. Still, breaking down a photochemical reaction into its fundamental steps should reveal much more information. The direct observation of radiationless transfer between adiabatic electronic states is a key step to build appropriate kinetic models for the reaction and further understand the role and mechanisms of non-adiabatic dynamics. Going one step further, resolving nuclear motion at and near conical intersections is also of importance, as it is the coupling of this motion with that of the electrons which enables the non-adiabatic relaxation that is key to many photochemical reactions.

1.4 Time Domain Approach: Pump-Probe Experiments and Electron Spectroscopy

In the previous section, we found that the characteristic frequencies for vibrational motion (which was orders of magnitude slower than electronic motion) went as $\omega \sim \Delta E/\hbar$. With a representative ΔE=100 meV, this leads to periods of motion on the order of $t \sim 10^{-14}$ s, or 10 femtoseconds (fs). This is many orders of magnitude faster than what can be perceived by both humans ($t_{\text{min}} \sim 0.1$ s) and computerized systems such as typical cameras, photodiodes, or other gated electronics ($t_{\text{min}} \sim 1$ ns).

Instead, time-resolved spectroscopy has been developed for several decades, using two (or more) ultrafast light pulses to directly measure molecular dynamics in the time-domain [27]. A pump pulse first excites the system and initiates the photochemical reaction. The pump pulse should have a temporal duration shorter than (or on the same order as) the dynamics to be studied, and must also have spectral content at energies corresponding to the excitation in question. The probe pulse, which will arrive with a specific and controllable time delay Δt with respect to the pump pulse, should also be short in duration, although there is a less rigorous constraint on its spectrum. The probe pulse should interrogate the instantaneous state of the excited system, such that by scanning the time delay will result in a time-domain picture of the evolving wavefunction $\Psi(r, R; t)$. In practice, full measurement of this wavefunction is not feasible: instead, some observable with some ideally strong dependence on this wavefunction is measured with the probe.

While other probe schemes, such as transient absorption [28] and Raman spectroscopy [29], have been demonstrated and are widely used, each with its own set of advantages and disadvantages, photoionization of the excited state followed by the detection of the resulting ions and/or electrons can lead to a large amount of information. In fact, taking a step back from the time-resolved study of excited state dynamics, molecular physics has historically been driven in large part by photoionization experiments. For example, measurement of a static photoelectron spectra reveals information about both the electronic and vibrational structure described in section 1.2 [30].

Ionization of a localized vibrational wavepacket will lead to photoelectrons with a kinetic energy (KE_{e^-}) distribution that will depend on both the electronic state occupied and the nuclear geometry. Time-resolved photoelectron spectroscopy (TRPES) [31] has been widely employed over the last two to three decades, making use of this dependence to track the state of the excited system as it evolves in time [32, 33, 34, 35, 36, 37]. Typically, the experimentally measured time-resolved photoelectron spectra $I(\text{KE}_{e^-}, \Delta t)$ will be parsed into various contributions that are assigned to N individual electronic states:

$$I(\text{KE}_{e^-}, \Delta t) = \sum_{i}^{N} I_i(\text{KE}_{e^-}, \Delta t). \tag{1.19}$$

In doing so, the time-dependent population $P_i(\Delta t)$ of each electronic state can be found

with:

$$P_i(\Delta t) = \int I_i(\mathrm{KE}_{e^-}, \Delta t) d\mathrm{KE}_{e^-}. \tag{1.20}$$

In some cases, this separation is straightforward, as the underlying spectra associated with individual electronic states will each lie in non-overlapping regions of photoelectron kinetic energy. This can be expected for a subset of experiments by extending Koopman's theorem [38] to excited state photoionization [39]: ignoring electronic correlation dynamics, valence photoionization can be treated using the molecular orbital picture. In cases where the individual spectra overlap, a global lifetime analysis has often been preferred, separating the spectra into underlying components with differing temporal evolutions [40, 35, 41]. Again, since underlying molecular dynamics can often lead to an accurate kinetic representation, decaying or rising exponential temporal evolutions are typically sought after.

However, these individual spectra are also sensitive to the vibrational wavepacket since the measured photoelectron kinetic energy will depend on the nuclear geometry [42, 43, 44], making photoelectron spectroscopy a possible direct probe of the nuclear motion involved in non-adiabatic dynamics. We can return to the Franck-Condon analysis and, at least within the Born-Oppenheimer approximation, describe ionization by considering the continuum of final states. These final states can be described by an ionic molecular state $|\psi_j \chi_l^{(j)}\rangle$ and a free electron with a given wavevector $|\vec{k}_{e^-}\rangle$, giving probabilities for the population of an electron with wavevector $\vec{k}_{e^-}$:

$$P(\vec{k}_{e^-}, t) \propto |\sum_{ijkl} c_{ik} e^{iE_{ik}t/\hbar} \langle \psi_i | \vec{\mu}_e | \psi_j \otimes \vec{k}_{e^-} \rangle S_{(ik),(jl)} \cdot \vec{E}_\omega(\frac{E_{jl} + \mathrm{KE}_{e^-} - E_{ik}}{\hbar})|^2, \tag{1.21}$$

where KE_{e^-} represents the energy of the outgoing photoelectron and the term $\vec{E}_\omega(\Delta E/\hbar)$ represents the spectral component of the ionizing field resonant with the transition. If the photon energy is known, the latter leads to a delta function that enforces energy conservation. The use of ultrafast pulses with relatively broad spectra will broaden the measured photoelectron spectra. Here, we have assumed that the ionization occurs much faster than any system dynamics. Using pulses with finite duration will lead mainly to time-average smearing, although interferences due to the evolution of both the initial and final states involved in this ionization can play a subtle role [18].

From the viewpoint of a localized excited vibrational wavepacket, we can make the approximation that ionization with broadband ultrafast pulses is impulsive and purely vertical (i.e. there is little or no vibrational redistribution during the ionization process) [45], and find that the measured photoelectron kinetic energy KE_{e^-} will depend on it's nuclear geometry $\vec{\mathbf{R}}$ and electronic state i dependent binding energy $\tilde{\mathcal{E}}_i(\vec{\mathbf{R}})$:

$$\mathrm{KE}_{e^-} = \hbar\omega_p - \tilde{\mathcal{E}}_i(\vec{\mathbf{R}}), \tag{1.22a}$$

$$\tilde{\mathcal{E}}_i(\vec{\mathbf{R}}) = \mathrm{E}_c(\vec{\mathbf{R}}) - \mathrm{E}_i(\vec{\mathbf{R}}), \tag{1.22b}$$

where $\mathrm{E}_c(\vec{\mathbf{R}})$ and $\mathrm{E}_i(\vec{\mathbf{R}})$ represent the geometry dependent energies of the cationic and excited electronic state, respectively, and $\hbar\omega_p$ is the energy of the probe photon, as seen in fig. 1.5. For

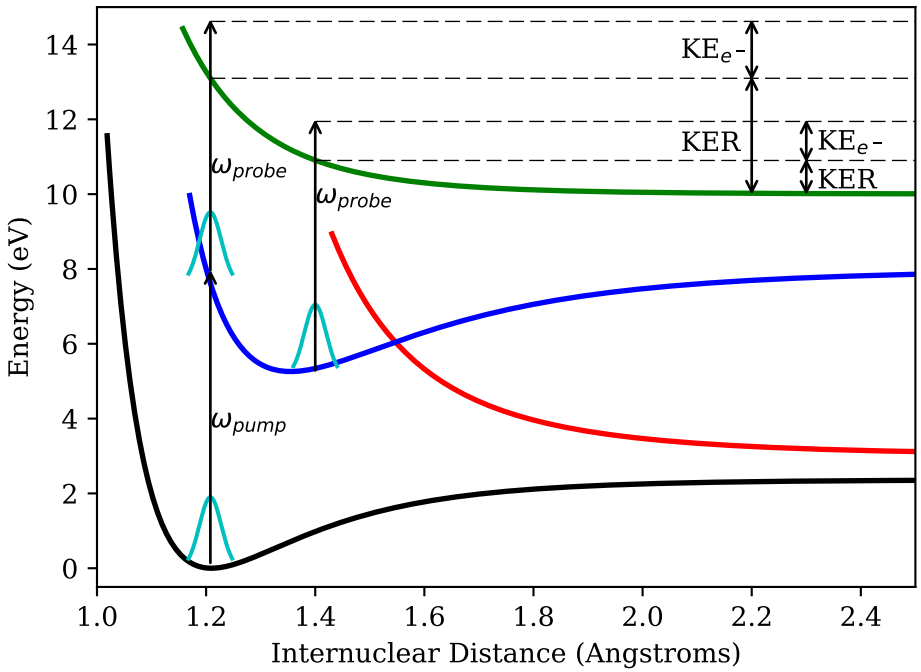

Figure 1.5: **Photoion and Photoelectron Spectroscopy.** Ionization of an excited wavepacket evolving on the neutral excited state adiabatic energy curves (blue, red) to the cation (green) will result in a photoelectron with a kinetic energy that depends on both the occupied electronic state and the nuclear geometry. If the ionization is also dissociative, the kinetic energy release of any measured ionic fragment will also depend on the state of the excited system at the time of ionization.

possible comparisons with static binding energies measured using, for example, synchrotron radiation, we will redefine the binding energy by shifting from the above definition by the excitation energy E_0. We find experimentally measurable binding energies $\mathcal{E}(\vec{\mathbf{R}})$, which we can compare to calculated binding energies for each excited electronic state $\mathcal{E}_i(\vec{\mathbf{R}})$:

$$\mathcal{E}_i(\vec{\mathbf{R}}) = \tilde{\mathcal{E}}_i(\vec{\mathbf{R}}) + E_0 = \mathrm{E}_c(\vec{\mathbf{R}}) - \mathrm{E}_i(\vec{\mathbf{R}}) + \mathrm{E}_0, \tag{1.23a}$$

$$\mathcal{E} = \sum \hbar\omega - \mathrm{KE}_{e^-}. \tag{1.23b}$$

In chapters 4 and 5, I will present the use of these relationships to extract information on the time-evolving nuclear geometry $\vec{\mathbf{R}}(t)$ of an excited system from its TRPES. As a molecular target begins to rearrange itself following photoexcitation, its effective binding energy will also evolve with time. Signatures of such excited state vibrational wavepacket dynamics can then be observed in the TRPES, for example, as oscillating [46, 47, 48] or shifting [42, 49, 43, 50, 51, 44] features. Since electronic excitation will, in general, initiate a vibrational

wavepacket away from equilibrium, a dynamical shift of the photoelectron spectrum may be expected from most systems at early time delays. Since it is the coupled evolution of the nuclear and electronic degrees of freedom that enables them, measuring such vibrational wavepackets is an important step to characterizing non-adiabatic excited state dynamics, alongside the time-resolved excited state populations $P_i(t)$ from which kinetic models are built.

Chapter 2

High Flux, High Repetition Rate Vacuum and Extreme Ultraviolet Beamline Implementation and Characterization

The first necessary task for the following experiments is the generation of a suitable light source. Pump and probe pulses must be provided with (1) spectral content that can be tailored depending on the system and dynamics to be studied and (2) time durations on the order of or shorter than the characteristic dynamic time scales. An additional requirement is that the probability for both the pump and probe to interact with a given molecule be non-negligible. Due to unfavorable scaling laws for short wavelength lasing [52], the VUV and XUV light needed for the experiments described in the previous chapter must be obtained in a different way. Here, we turn to frequency upconversion using established ultrafast laser technology in the near infrared as a driver.

In this chapter, I will briefly review the non-linear optics that allow for upconversion in the perturbative regime [53]. In the strong-field regime, high harmonic generation (HHG) has emerged since its discovery a few decades ago as the de facto method for generating coherent light beyond the ultraviolet in a tabletop setup [54, 55]. The spectral and temporal characteristics of an HHG based light source are considered. Next, I describe our implementation of a VUV/XUV light source, focusing on aspects unique to this high pulse energy, high repetition rate setup. The state-of-the-art laser system driving the HHG process, the long-focusing geometry for generation, and spectral filtering are discussed. Finally, we present two further applications of this bright HHG source, external free-electron laser (FEL) seeding and non-linear XUV optics.

2.1 Nonlinear Optics and High Harmonic Generation

Nonlinear Optics

When light passes through matter, its electric field can cause displacements of the electrons in the medium. The amount of displacement, dependent on the strength of the field E, can be quantified by the polarization density of the medium P:

$$P = \epsilon_0 \chi E, \tag{2.1}$$

where χ is the susceptibility of the material describing its response to an electric field. For the low intensities of light which we encounter in the vast majority of our world, electric fields are on the order of V/cm or below and are not strong enough to alter the optical properties of the medium. As such, the effect of two applied fields can be well approximated as the sum of the effects of each field:

$$P(E_1 + E_2) = P(E_1) + P(E_2). \tag{2.2}$$

This comprises the domain of linear optics, from which a wide array of optical properties, including reflection, refraction, scattering, and absorption, can be derived.

At higher intensities, where the material begins to be modified by an electric field so much that it will interact differently with a second field, non-linear effects appear. For moderate intensities, a perturbative approach is adequate and the polarization is expanded as a Taylor series:

$$P = \epsilon_0(\chi^{(1)}E + \chi^{(2)}E^2 + \chi^{(3)}E^3 + ...), \tag{2.3}$$

where each term $\chi^{(i)}$ describes higher order responses to the field. Since light will have electric fields which oscillate as $E = E_0\cos(\omega t)$, the second order term in eq. (2.3) will have components that oscillate at $\cos^2(\omega t) = \frac{1}{2}[1 + \cos(2\omega t)]$. The polarization can thus contain components oscillating at 2ω (and higher orders of ω from the higher order terms). The invention of the laser in 1960 gave access to electric fields many orders of magnitude higher than had been achieved before, and such frequency upconversion was observed shortly thereafter by 1961 [56]. Other nonlinear phenomena include sum and difference frequency generation, optical rectification, and saturable absorption [53], as well as multiphoton absorption leading either to excitation or ionization.

It can be argued that the nonlinear terms in eq. (2.3) will be on the same order as the linear term when the applied electric field is on the same order as the electric field E_a holding atoms together:

$$E_a = \frac{e}{4\pi\epsilon_0 a_0^2} \approx 5 \times 10^9 \text{V/cm}, \tag{2.4}$$

where e is the atomic charge and a_0 the Bohr radius. As a rough approximation, we find that higher order components of the polarization will diminish as $(E/E_a)^{n-1}$. This limits upconversion in this perturbative approximation to low harmonic orders.

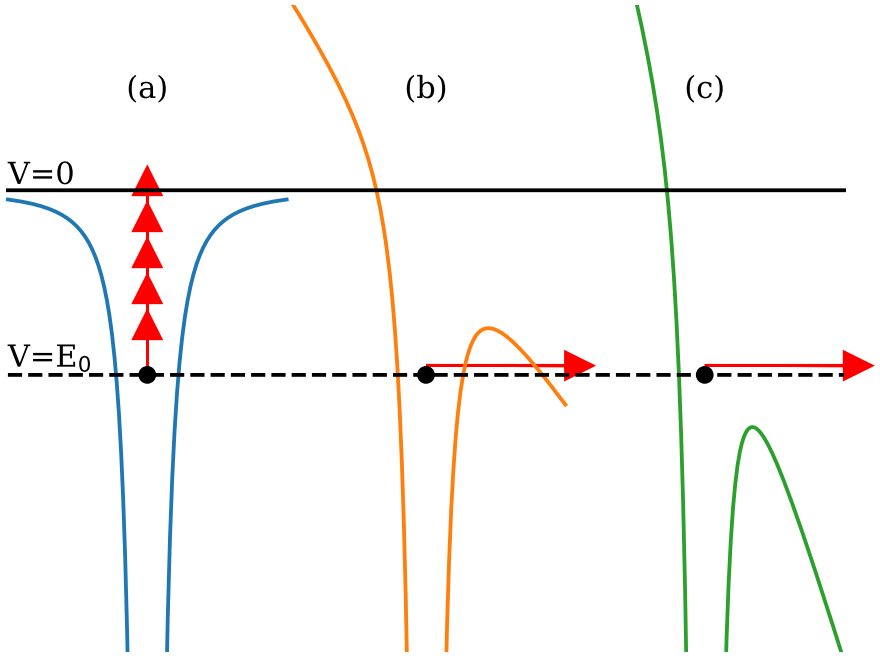

Figure 2.1: **Regimes of Low-Frequency Photoionization.** (a) For weak fields (in the perturbative limit), the absorption of several photons can help overcome the ionization potential of an atom. (b) At stronger field strengths, the potential due to the light can be on the same order as the Coulomb potential, and the perturbative approximation breaks down. A barrier for ionization appears, and tunneling through this barrier leads to ionization. (c) At even higher fields, the barrier is lowered such that the electron is completely unbound.

Strong Field Physics

With the advent of ultrafast optical and infrared sources several decades ago, electric fields comparable or exceeding the atomic electric field E_a became available, breaking down the perturbative approximation made above. Instead, new solutions to the Schrödinger for the atom (or more complicated media) must be found in which the light is directly included as potential energy term:

$$V_{\text{atomic}} \Rightarrow V_{\text{atomic}} + V_{\text{laser}}. \tag{2.5}$$

In this strong field limit, the multiphoton ionization picture mentioned above is no longer adequate and must be replaced by either a tunneling ionization or barrier suppression ionization picture, as seen in fig. 2.1. Strong-field ionization is described in the atomic case by the analytical theory of Ammosov, Delone, and Krainov [57]. As a simple parameter to distinguish between the perturbative and strong-field regimes, the Keldysh parameter γ [58] can be introduced, describing the ratio of multi-photon to tunneling ionization in terms of

the ionization potential I_p and the ponderomotive energy U_p of the field:

$$\gamma = \sqrt{\frac{I_p}{2U_p}}, \tag{2.6a}$$

$$U_p = \frac{e^2E^2}{4m_e\omega^2} = 9.33 \text{ eV} \times (\lambda \text{ [}\mu\text{m]})^2 \times I \text{ [}10^{14} \text{ W/cm}^2\text{]}. \tag{2.6b}$$

The ponderomotive energy describes the cycle averaged energy of a free electron in an electric field, and appears in several other aspects of light-matter interaction in the strong-field limit. For example, the continuum levels of an atom are shifted by this energy U_p in the presence of a strong field, effectively increasing the ionization potential [59].

The Three Step Model

High harmonic generation was first observed in 1987, when odd harmonics of the fundamental radiation from a KrF laser were observed up to the 17^{th} order [60]. As opposed to frequency upconversion in the perturbative regime, the strength of neighboring harmonics plateaued until the limit was reached, signifying a different mechanism. At the single atom level, the three step model was introduced as a semi-classical model providing an intuitive description of the observed high order upconversion process [61, 62]:

1. The laser field distorts the Coulomb potential, as in fig. 2.1(b), leading to tunneling ionization. A free electron is born with low (or zero) velocity at the time of ionization due to the tunneling process.

2. Disregarding the ionic potential, the electron undergoes classical acceleration away from the core due to the electric field. As the electrical field oscillates and changes sign, the electron slows down and can eventually be turned around, accelerating back towards the ionic core.

3. For some trajectories, the electron can find itself back in the vicinity of the ionic core. With some (small) probability, the electron can recombine with the the ion, releasing all of its excess kinetic energy as a single, high energy photon.

As seen in fig. 2.2, depending on the phase of ionization, the electron will undergo different trajectories. The electron can have a kinetic energy up to $\sim 3.17U_p$ at the moment of recombination, again depending on the phase of the field at the moment of ionization. For each recombination energy, both a short and a long trajectory exist, which may interfere. The energy of the emitted photon will be equal to this kinetic energy added to the ionization potential, such that the maximal photon energy reached goes as:

$$E_{\max} = I_p + 3.17U_p. \tag{2.7}$$

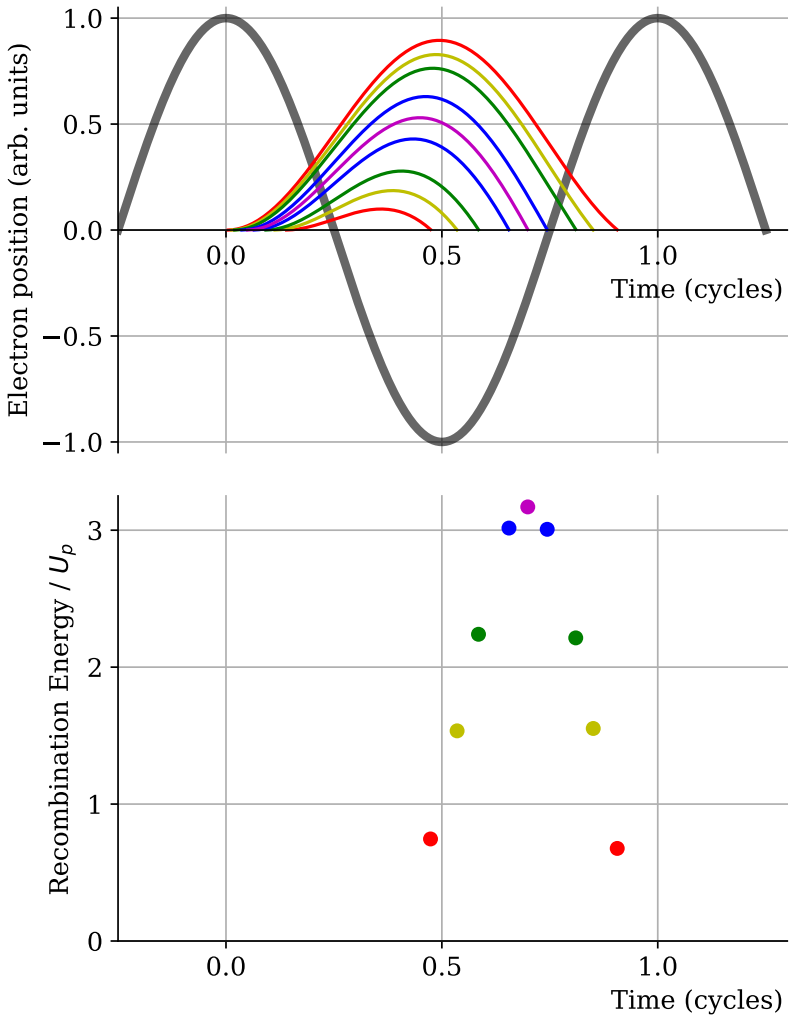

Figure 2.2: **Classical Trajectories in the Continuum.** Depending on the phase of the electric field (shown in gray), the electron will undergo different trajectories in the continuum. Certain trajectories will return to the ionic core and can recombine. The recombination energy scales with the ponderomotive potential U_p, giving a linear scaling with higher intensity and quadratic scaling with driving wavelength.

This cutoff energy can thus be shifted by choosing a medium with a higher ionization potential or by increasing the ponderomotive energy by increasing either the intensity or the wavelength of the light. All energies between I_p and $E_{\max}$ are allowed, and, since we can expect the ionization and recombination rates to not have too large of dependences on the ionization times and recombination energy, respectively, a continuum of frequencies is emitted in this single atom, single cycle picture. The recombination events all occur in a relatively short window of the laser cycle, leading to an attosecond burst of light. This process repeats itself for every half cycle of the driving laser. In the time domain, this leads to a train of attosecond bursts emitted at twice the frequency of the laser light. In the frequency domain, due to the symmetry of the medium, emission events from neighboring half cycles will interfere destructively for even harmonics of the fundamental light and constructively for odd harmonics. For shorter driving pulses with less half-cycles, this interference may not be complete, and a quasi-continuum can reemerge. By limiting the emission to just one half-cycle, isolated attosecond pulses with a continuous spectrum are emitted [63, 64].

While this semi-classical model qualitatively predicts much of the physics of the HHG process for a single atom, a fully quantum mechanical treatment is also possible, with the time-dependent dipole moment expressed as a product of an ionization transition probability, wavepacket propagation in the field-dressed continuum, and a recombination transition probability closely related to that of ionization [65]. The Fourier transform of this dipole moment yields the frequency output of the HHG process. While also serving as a starting point for meaningful quantitative predictions, the quantum mechanical picture brings out one additional quantitative feature of HHG over the classical model: since the electron trajectories scale in time with λ and that a localized continuum electron wavepacket will naturally spread in time, the recombination rate quickly decreases with larger λ since the overlap of the returning electron wavepacket with the ionic core will be smaller.

Phase Matching and Absorption

Beyond the single atom picture, phase matching plays a crucial role in HHG. One of the main advantages of a HHG source is coherence: while high harmonic photons can be created at macroscopic distances away from each other in a gas cell, their phases are not random, unlike for synchrotron radiation, instead determined by the phase of the driving laser field. We can expect this field to be fully coherent, such that the phase of the field evolves in time and space as:

$$\partial\phi_0(x,t;\partial x,\partial t) = k(w_0,x,t)\partial x + \omega_0\partial t. \tag{2.8}$$

The phase of light at a given harmonic order q generated at a given position and time will be related to the phase of the driving field:

$$\phi_q(x,t) = q\phi_0(x,t) + \Delta\phi_{0,q}, \tag{2.9}$$

where the phase offset $\Delta\phi_{0,q}$ comes from various contributions in the three-step model. This phase will evolve following:

$$\partial\phi_q(x,t;\partial x,\partial t) = k(\omega_q,x,t)\partial x + q\omega_0\partial t. \tag{2.10}$$

Phase mismatch between the harmonic light emitted downstream and that emitted upstream and propagated downstream can occur:

$$\begin{aligned}
\Delta\phi_q &= \phi_q(x+\partial x,t+\partial t) - [\phi_q(x,t) + \partial\phi_q(x,t;\partial x,\partial t)] && \text{(2.11a)}\\
&= q\phi_0(x+\partial x,t+\partial t) + \Delta\phi_{0,q} - [q\phi_0(x,t) + \Delta\phi_{0,q} + k(\omega_q,x,t)\partial x + q\omega_0\partial t] && \text{(2.11b)}\\
&= qk(\omega_0,x,t)\partial x - k(\omega_q,x,t)\partial x, && \text{(2.11c)}\\
\Delta k_q &= qk(\omega_0,x,t) - k(\omega_q,x,t). && \text{(2.11d)}
\end{aligned}$$

In order to avoid destructive interference, this phase mismatch must be minimized.

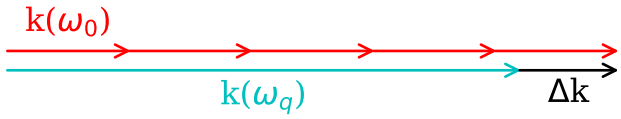

In vacuum, this phase mismatch will be zero. However, for the HHG process, a variety of phenomena will contribute. First, we consider the dispersion due to the generation medium. Using the relationship $k(\omega) = \frac{n(\omega)\omega}{c}$, we find:

$$\begin{aligned}
\Delta k_{q,\text{medium}} &= q\frac{n(\omega_0)\omega_0}{c} - \frac{n(\omega_q)\omega_q}{c} && \text{(2.12a)}\\
&= \frac{q\omega_0}{c}\left[n(\omega_0) - n(\omega_q)\right]. && \text{(2.12b)}
\end{aligned}$$

Since the medium will be partially ionized (with fraction η), there will be contributions from both neutral gas and plasma:

$$\Delta k_{q,\text{medium}} = (1-\eta)\rho\left[\tilde{n}(\omega_0) - \tilde{n}(\omega_q)\right]_{\text{neutral}} + \eta\rho\left[\tilde{n}(\omega_0) - \tilde{n}(\omega_q)\right]_{\text{plasma}}, \tag{2.13}$$

where ρ is the medium density and $\tilde{n}(\omega) = n(\omega)/\rho$ is the index of refraction per unit density. The contribution to the index of refraction from the plasma will depend on the plasma frequency ω_p:

$$\begin{aligned}
\eta\rho\tilde{n}(\omega)_{\text{plasma}} &= \sqrt{1-(\frac{\omega_p}{\omega})^2} && \text{(2.14a)}\\
&\approx 1 - \frac{1}{2}(\frac{\omega_p}{\omega})^2 && \text{(2.14b)}\\
&= 1 - \frac{e^2\eta\rho}{2\epsilon_0 m_e\omega^2}, && \text{(2.14c)}
\end{aligned}$$

from which we find:

$$\Delta k_{q,\text{atomic}} = (1-\eta)\rho\left[\tilde{n}(\omega_0) - \tilde{n}(\omega_q)\right], \tag{2.15}$$

$$\Delta k_{q,\text{plasma}} = -\frac{qe^2\eta\rho}{2\epsilon_0 m_e \omega_0 c}(1-\frac{1}{q^2}). \tag{2.16}$$

Next we consider two sources of additional phase due to the focusing of the laser beam. For a focused Gaussian beam, solutions to Maxwell's equations under the paraxial approximation [53] take the form:

$$E(r,z,t) = E_0\frac{w_0}{w(z)}e^{-r^2/w^2(z)}e^{i(k_0 z + k_0 r^2/2R(z) + \Phi_G(z) - \omega_0 t)}, \tag{2.17a}$$

$$w(z) = w_0\sqrt{1+(\frac{z}{z_R})^2}, \tag{2.17b}$$

$$\Phi_G(z) = -\tan^{-1}(z/z_R), \tag{2.17c}$$

$$z_R = \frac{\pi w_0^2}{\lambda}, \tag{2.17d}$$

$$R(z) = \frac{z w^2(z)}{w_0}, \tag{2.17e}$$

$$\tag{2.17f}$$

where $w(z)$ is the beam waist of the focusing beam along the propagation direction, w_0 is the beam waist at focus, $\Phi_G(z)$ is the Gouy phase shift, and $R(z)$ is the radius of curvature of the phase fronts, all of which depend on the focusing geometry. Using $k(\omega) = \partial\phi(w)/\partial z$, we will find additional terms for the focused beam compared to a plane wave electric field where $k(\omega) = k_0$.

After the first ionization step of HHG, the propagating electron wavepacket and thus the harmonic light accumulates a phase due to the presence of the driving electric field which can be roughly approximated as $\phi_{prop} = U_p\tau/\hbar$, with U_p as defined in eq. (2.6b) proportional to the intensity $I(z,t)$ and τ is the amount of time the electron spends in the continuum. Defining an intensity dependent phase coefficient α_q^j [65], we find:

$$\phi_{prop} = \alpha_q^j I(z,t). \tag{2.18}$$

As the beam propagates along the focus, the intensity will also change:

$$I(z,t) = I_{peak}(t)(\frac{w_0}{w(z)})^2 = \frac{I_{peak}(t)}{1+(z/z_R)^2}. \tag{2.19}$$

Again using $k(\omega) = \partial\phi(w)/\partial z$, we find that the varying intensity along the focusing axis adds another wavevector mismatch called the dipole phase mismatch:

$$\Delta k_{\text{dipole}} = \frac{dI(z,t)}{dz} \tag{2.20a}$$

$$= -\frac{2I_{peak}(t)}{z_R}\frac{z/z_R}{\left[1+(z/z_R)^2\right]^2}. \tag{2.20b}$$

For our applications (as discussed below), a long focusing geometry with the gas cell placed away from the focus will be used and the Gouy phase shift will be minimal over the length of the generation medium, such that it can safely be ignored. In most cases, the atomic term Δk_{atomic} will be positive since the index of refraction at high frequencies converges to 1, the plasma term Δk_{plasma} will be negative, and the sign of Δk_{dipole} can be chosen by using positive or negative z, allowing for the sum of these terms to go to zero by tuning, for example, the gas pressure, focusing geometry, laser power, and gas cell position relative to the focus. However, several complications arise. For example, both the intensity $I(z, r, t)$ and the fraction of ionized gas $\eta(t)$ are time-dependent, making phase matching a dynamical problem. Next, the phase matching condition depends on q, such that some harmonic orders will have better phase matching than others. On- and off-axis phase matching should be considered, where the wavevectors $\vec{k}(\omega_0)$ and $\vec{k}(\omega_q)$ are correctly treated as vectors rather than scalars [66].

Perhaps most important is consideration of reabsorption, since any target used as a non-linear medium for HHG will have absorption throughout the spectral range of interest (¿10 eV). From the target pressure ρ and its (energy dependent) absorption cross-section σ, we can find a characteristic absorption length:

$$L_a = \rho\sigma, \tag{2.21}$$

where $\frac{e-1}{e} \approx .632$ of the current flux will be absorbed. As described with the framework of the three-step model, harmonic gain will be linear with propagation at best (assuming perfect phase-matching conditions): unlike laser amplification, the presence of harmonic light does not stimulate further generation. This will lead to saturation of the harmonic flux, where any generation is counteracted by absorption. In practice, imperfect phase-matching will impose further restrictions. As a simple model of a 1-D generation medium of length L_m with constant atomic dipole response and phase-matching conditions, we find that the harmonic field $E_q(z)$ will grow as [67]:

$$\frac{dE_q}{dz} \propto \exp\left(-\frac{L_m - z}{2L_a}\right) e^{i\Delta k z}. \tag{2.22}$$

Integration over the medium and defining the coherence length $L_c = \frac{\pi}{\Delta k}$, we find a final harmonic output of [67]:

$$I_q \propto \frac{L_a^2}{1 + 4\pi^2(L_a/L_c)^2}\left[1 + e^{-L_m/L_a} - 2\cos(\pi L_m/L_c)e^{-L_m/2L_a}\right]. \tag{2.23}$$

The harmonic flux as a function of propagation length is shown for several values of the coherence and absorption lengths in fig. 2.3. For small coherence lengths, strong oscillations in the harmonic intensity are observed due to interference. For long coherence lengths, saturation is achieved after several absorption lengths.

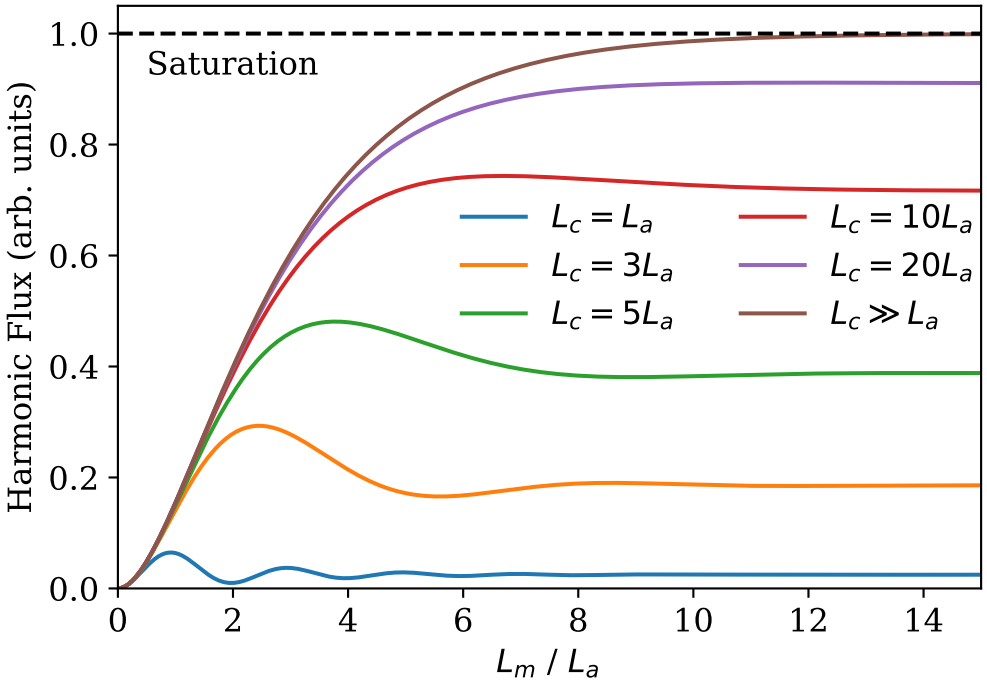

Figure 2.3: **Harmonic Gain with Reabsorption and Phase Mismatch.** Considering only the single atom response, harmonic gain will be linear with propagation. However, interference of harmonic light generated at two different positions due to phase mismatch and reabsorption in the gas will limit the attainable harmonic flux. The conditions $L_m > 3L_a$ and $L_c > 5L_a$ assure that half of the saturation flux will be reached [67].

Low Order Harmonics

As presented, the three-step model predicts a plateau of harmonics between $I_p \leq \hbar\omega_q < 3.17U_p$. However, efficient harmonic generation below the ionization potential is observed even when going beyond the perturbative regime [68]. Instead, their appearance has instead been explained at first by field-driven transient resonance effects [69, 70] but more recently by the inclusion of the ionic core in the three-step model, allowing for more complex electron trajectories and recombination dynamics [71]. Apart from rare and narrow atomic excitation resonances, the generation of these harmonics will not suffer from reabsorption as above. As such, their flux can be much higher than that of high order harmonics, limited mainly by phase-matching and geometrical considerations. While low order harmonics can also be generated in the perturbative regime using crystals with large non-linearities, pushing this generation to the VUV is difficult due to both reabsorption (limiting flux) and dispersion (limiting pulse durations) in the medium, making the gas-based HHG approach preferential for generating short VUV pulses.

2.2 Terawatt, Kilohertz Laser System

Since its characterization three decades ago [72], Titanium-doped Sapphire (Ti:Sapph) crystals have enabled large leaps in various areas of optical science due to their many advantages as a lasing medium [73]. Among other attributes, their remarkably broad gain bandwidth in the near-infrared, high thermal conductivity, and efficient pumping with flash-lamp or diode based green lasers have made Ti:Sapph lasers a staple of most ultrafast science labs. While driving HHG using these lasers has become a relatively standard undertaking, scaling to high enough VUV/XUV pulse energies and repetition rates to make pump-probe experiments feasible requires a similarly scaled driving laser. For this work, I have made use of the commercial laser (KMLabs) installed at Lawrence Berkeley National Laboratory in summer of 2012. This laser combines a mode-locked Ti:Sapph oscillator with a three stage amplifier, outputting $\sim$30 mJ, $<$ 30 fs pulses at a central frequency of 780 nm and at a repetition rate of 1 kHz, making it the world's first terawatt, kilohertz, tabletop laser. The laser system has gone through several changes since its installation: I will briefly discuss its current state, which is mostly unchanged from its condition when the experiments presented in chapters 4 and 5 were conducted.

A Kerr-lens mode-locked oscillator (Griffin, KMLabs) pumped by 5.5 W of 532 nm light from a frequency doubled diode-pumped laser (Laser Quantum Opus) emits $<$ 30 fs pulses centered at 780 nm with $>$ 50 nm of bandwidth at a repetition rate of 88 MHz. These pulses are sent through a pulse shaper (MIIPS, Biophotonic Solutions Inc.), which uses gratings to spectrally disperse the beam and applies an arbitrary phase mask in this Fourier domain. This shaper was used to precompensate for third and higher order dispersive phases accumulated during the subsequent amplification and beam-transport, shortening the compressed pulses from a typical 35-45 fs to as low as 25 fs, as measured using a home-built frequency-resolved optical gating (FROG) spectrometer [74]. These pulses were then sent through a grating-based stretcher, increasing the pulse duration to $>$ 200 ps to reduce the peak intensities of the light traveling through the chirped pulsed amplification amplifiers.

The first amplification stage consists of a cavity-based, cryo-cooled regenerative amplifier. The 88 MHz pulse train is down-selected to 1 KHz using a Pockels cell, trapping pulses in the amplifier cavity pumped by 10 W of green light (Coherent Evo-30) until gain saturation is reached. An intracavity gain-flattening filter, which partially reflects the central portion of the broad spectrum, helps maintain the $>$50 nm bandwidth from the oscillator. This amplifier typically outputs 1.5 W.

The next two stages of amplification consist of two cryo-cooled multipass amplifiers, each pumped by two $>$ 40 W diode-pumped green lasers (Coherent Evo-HE). The large amount of average power in these two stages can easily lead to detrimental thermal lensing, which can result in unfavorable beam mode, loss of power, and damage to optics. Several changes to the original design helped mitigate much of the thermal lensing. First, a weakly divergent mirror was added in between the two stages of amplification to counteract some of the lensing in the first stage. Next, a camera imaging the green fluorescence from each surface of the crystal in the third amplification stage was added. This crystal allows to visualize

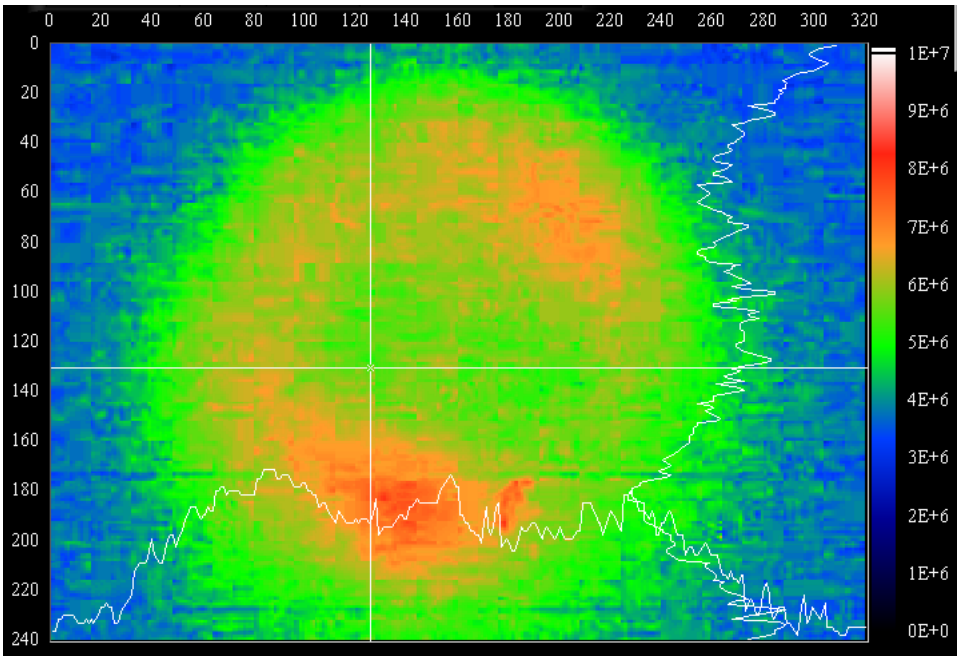

Figure 2.4: **Pump depletion in the last amplification stage.** The pump mode can be imaged by measuring its fluorescence. When one pass of the seed overlaps this mode, depletion of fluorescence is observed. This can be used to optimize seed spatial overlap, but can also be used to adjust the relative sizes of the two beams and to monitor thermal lensing as the beam propagates to later passes.

the overlap of the green pump and infrared seed as the overlapped region displays decreased fluorescence. The focusing of the green pump lasers was adjusted such that the seed beam mode closely matched the modes of the pump lasers, avoiding large thermal gradients. Finally, the amount of gain in each stage was adjusted. By increasing the pump power in the first multipass stage, we could reach levels close to saturation in the last amplifier using at first three and finally only two passes rather than the original five. Pass by pass alignment of the amplifier revealed that much of the mode issues came from the later passes and could be avoided by having less total passes. A typical gain progression through the multipass amplifiers is shown in fig. 2.5. Powers beyond 40 W can be achieved for the stretched amplifier output after full realignment, although this typically deteriorates to a more stable ∼35 W over several weeks due to drifts of the seed as well as damage of the pump laser routing and focusing optics.

Beam routing, compression, and focusing follow the amplification. A schematic of the laser, beamline, and experimental layout is shown in fig. 2.6. At the laser output, a small portion of the pulse energy can be routed towards a secondary beamline using a thin beam splitter. This beamline has its own compressor and can be recombined with the VUV/XUV beam in the end station. While the temporal resolution is limited, this beamline adds several

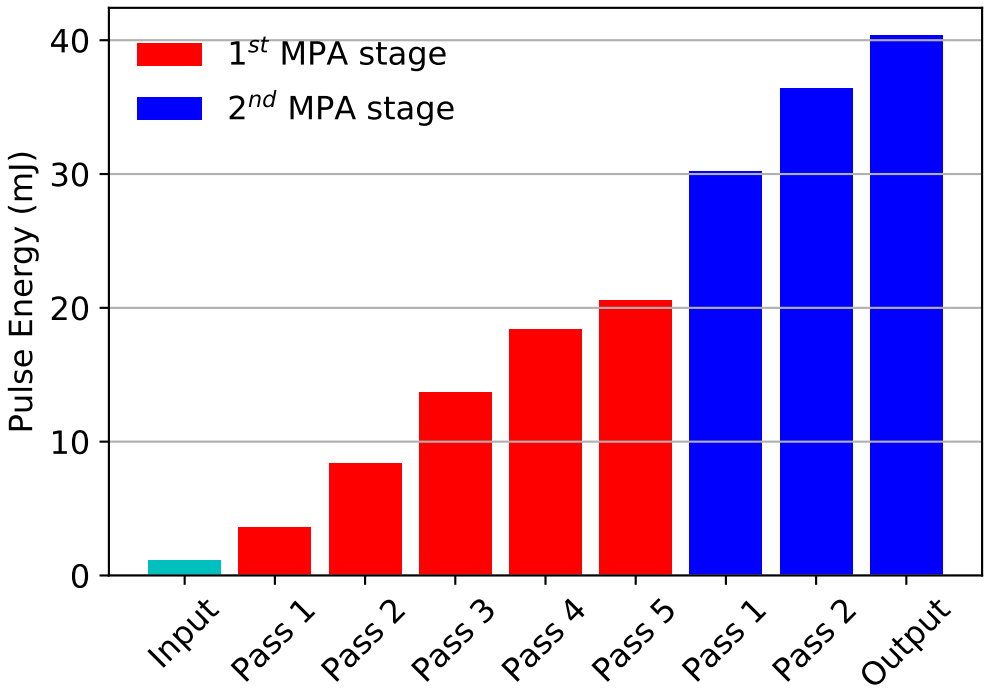

Figure 2.5: **Pass by pass gain in the multipass amplifiers.** The two MPA stages are each pumped by up ∼80 W of 532 nm light. Roughly 20 W of gain is extracted for each stage, corresponding to 25% efficiency. The last pass of the 2^{nd} MPA stage is usually bypassed to avoid strong thermal lensing.

experimental capabilities, including impulsive alignment of molecular samples [75].

The pulse compressor and all following optics were placed inside vacuum chambers. This was necessary due to the high $\sim 10^{12}\,\mathrm{W/cm^2}$ intensity of the unfocused beam following compression. At such intensities, the third-order non-linearity of eq. (2.3) can change the effective index of refraction:

$$n = n_0 + n_2 I, \tag{2.24}$$

where n_0 is the standard index of refraction, n_2 is the non-linear index of refraction, and I the intensity [53]. In the spatial domain, due to the Gaussian shape of the beam mode, this non-linear term can create an effective lens, which will lead to self-focusing of the laser. In the temporal domain, the intensity gradients of the rising and falling edges of the pulse can lead to unwanted phase shifts and also to the creation of new frequencies, a process known as self-phase modulation. We can estimate when such non-linear effects become important by calculating the phase shift ϕ_{NL} that will result from them:

$$\phi_{NL} = \frac{2\pi}{\lambda_0} n_2 I L, \tag{2.25}$$

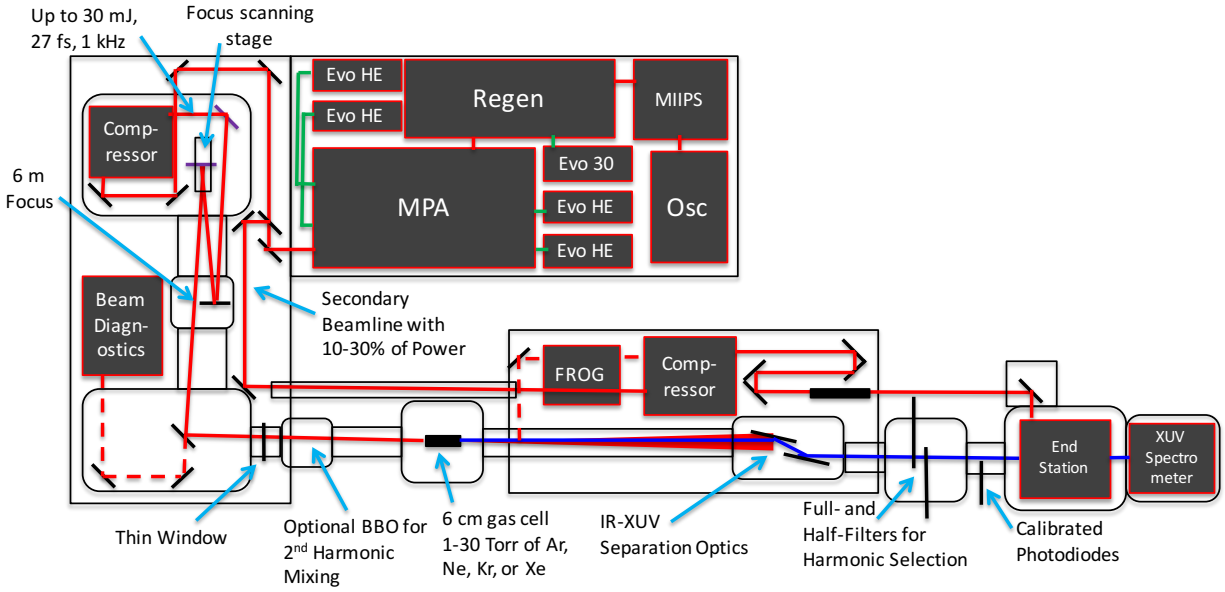

Figure 2.6: **Schematic of the laboratory layout.** After amplification in the regenerative amplifier (Regen) and two multipass stages (MPA), the beam is routed into vacuum chambers where it is compressed and focused towards the gas cell.

where L is the propagation distance. For air, the non-linear index of refraction is equal to $6\times10^{-19}\,\mathrm{cm}^2/\mathrm{W}$ [76], and we find that a π phase shift will develop after a propagation of only 0.7 m. As such, the compressor and beam focusing chambers were initially evacuated to avoid these effects.

In vacuum, all of the optics involved with the compressed beam, including 45° mirrors, the focusing mirror, a waveplate, and one of the gratings in the compressor, were found to develop a thin dark film as a result of laser ablation of hydrocarbons present even at 10^{-6} Torr pressures. While we have found removal of these films to be possible using a UV Ozone cleaner, they are reduced to carbon over time (about one week of laser exposure), at which point cleaning is no longer possible. These films cause several issues. The reflection of coated mirrors or diffraction efficiency of a coated grating are reduced. Additionally, the damage threshold of coated optics decreases, as these films lead to increased absorption. Due to the high average power of the system, we observe an additional problem: the thin films are found to heat considerably, especially in vacuum where cooling capacity is reduced as compared to an atmospheric environment. Due to the non-uniform structure of both the beam power and optics damage, we find that effective divergent lenses are created from the thermal expansion of these films, causing serious issues to the propagating beam as it focuses (as seen in fig. 2.7).

In order to overcome this, the compressor and folding chambers were separated from the main beamline by a thin UVFS window with an anti-reflection coating for the infrared, and these chambers were filled with 100 Torr of Helium gas, rather than being operated in

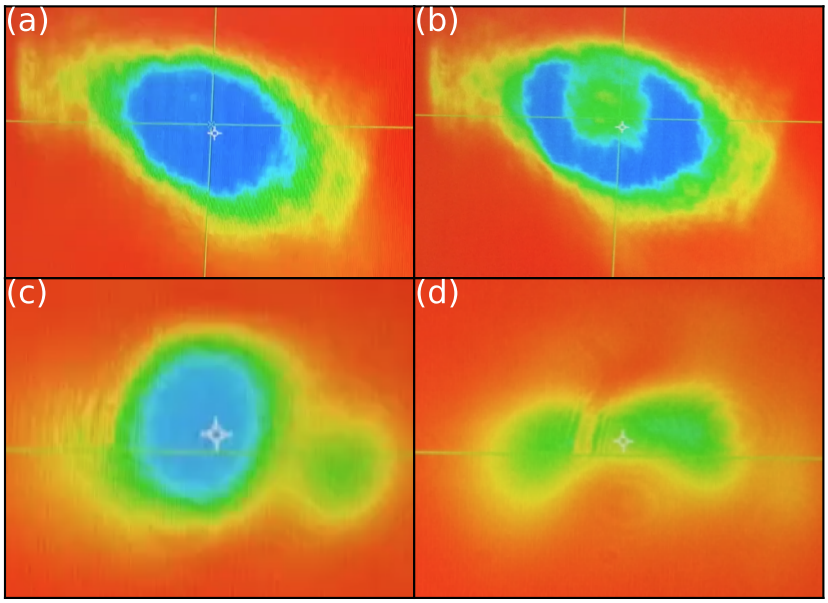

Figure 2.7: **Hydrocarbon film heating effects on the mode.** A leak-through of a mirror allows the beam mode to be imaged 3 m after the focusing optic (top) and at the focus (bottom). Immediately after unblocking the beam (left), the beam modes are smooth and mostly Gaussian. After 10 s of laser exposure (right), thermal issues lead to large deterioration of the beam mode.

vacuum. The non-linear index of refraction of Helium (per unit pressure) is two orders of magnitude smaller than that of air, while its thermal conductivity is four times larger [77], helping cool the optics irradiated by the compressed beam. Empirically, beyond cooling, we found that this Helium backfill prevented (or severely slowed down) the hydrocarbon film deposition [78], making it crucial for long-term operation.

2.3 VUV/XUV Beamline

To reach the peak intensities of $10^{14}\,\mathrm{W/cm^2}$ needed for efficient HHG with a 1 TW laser, a loose focusing geometry can be used. A 6 m focus gives both a large beam waist (120 μm) and a large Rayleigh range (60 mm). These combine to form a rather large focal volume in which harmonics can be generated. A gas cell is used as an interaction region. To reach higher pressures without compromising the nearby vacuum needed to avoid reabsorption, this gas cell is comprised of a central region in which gas is fed surrounded by two regions directly connected to high-throughput scroll pumps. Each of these regions is separated from the vacuum and from each other through small pinholes. These pinholes are drilled from thin aluminum shims by the laser in place. This reduces their size to the minimum

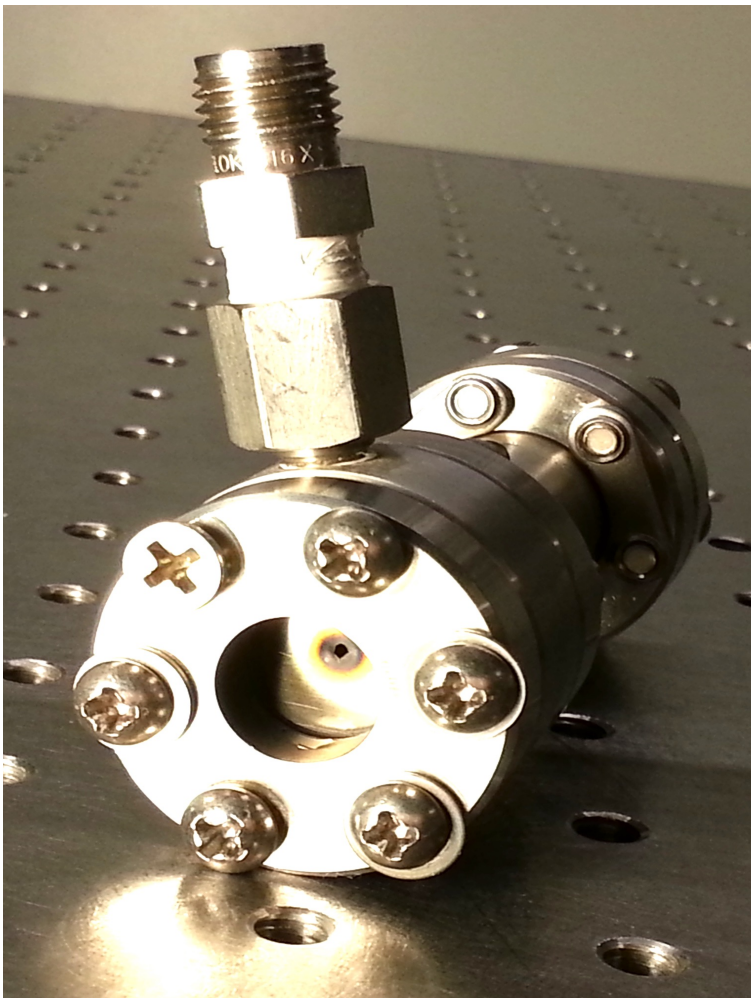

Figure 2.8: **Laser drilled pinholes on the gas cell.** The laser near focus is able to drill through Aluminum shims in seconds, giving precisely aligned and sized (300-500 μm) pinholes. The additional compartments for differential pumping with a scroll pump are not shown here.

needed to accommodate the laser and removes the need for precise alignment. With this differential pumping, pressures as high as 30 Torr can be set inside the gas cell while keeping the surrounding vacuum pressure below 10^{-2} Torr. Movable 5 mm pinholes downstream with differential pumping help maintain pressures below 10^{-6} Torr within several centimeters behind the gas cell. The length of the gas cell was empirically optimized to 6 cm.

Following generation of harmonics, the residual driving infrared light must be removed before the experimental interaction region. Typically, this is achieved using metal filters. However, the average power used here is much higher than the power that can be dissipated by thin ($\sim$ 100 nm) filters. Our first rejection attempt involved using Silicon mirrors set at Brewster's angle for 780 nm light (75° angle of incidence). At this angle, harmonics are efficiently ($> 60\%$ per reflection) reflected up to a cutoff energy near 50 eV. However, even the bulk Silicon material could not withstand absorbing the high average powers of the system. In-vacuum water cooling of such a Silicon mirror (using a copper intermediate) prevented the melting of the surface, but caused pointing instabilities due to flow. Instead, anti-reflection coated glass plates used at 80° incidence angle (Optique Fichou) were used. Using two of these mirrors, $> 10^6$ rejection of the infrared light was observed while harmonics up to 80 eV could be efficiently reflected ($> 30\%$ after two reflections). The infrared light was transmitted rather than absorbed by the mirror substrates. This light was absorbed by a beam dump thermally coupled to the vacuum chamber walls.

A typical spectrum optimized for high orders is shown in fig. 2.9. This spectrum was measured using 20 mJ of driving energy, with a 27 fs pulse centered at 780 nm, as measured with the FROG spectrometer. A 6 m focusing geometry was used, giving estimated spot sizes on the order of $\sim 300\,\mu$m at the 6 cm gas cell. This gas cell was filled with 2.1 Torr of Argon gas, which was optimized to maximize the signal of the 29^{th} harmonic (see section 2.5). The photon flux and harmonic pulse energy quoted reference the levels after two shallow angle bounces off of the coated Silicon mirrors introduced above and after propagation through a 200 nm thick Aluminum metal filter to further reject the driving infrared light. The spectra was measured using a home-built XUV spectrometer based off of a previous design [79]. Light is transmitted through a $d = 100$ nm nano-grating built using free-standing SiN membranes, giving $\sim 20\%$ XUV transmission in the energy range of interest [80]. The dispersed light is sent to an MCP coupled to a phosphor screen. The phosphorescence from this assembly is imaged out of vacuum to a digital camera. Since the photon energy-dependent grating transmission and MCP detection efficiencies are known, the measured spectrum can be corrected to yield the *in-situ* spectrum.

The spectrum is calibrated using the position of the observed peaks and by considering the geometry shown in fig. 2.10. A given harmonic order with wavelength $\lambda_q = q\lambda_0$ will have a first order diffraction at an angle θ_q with $d\,\sin\theta_q = \lambda_0/q$. This diffracted beam will

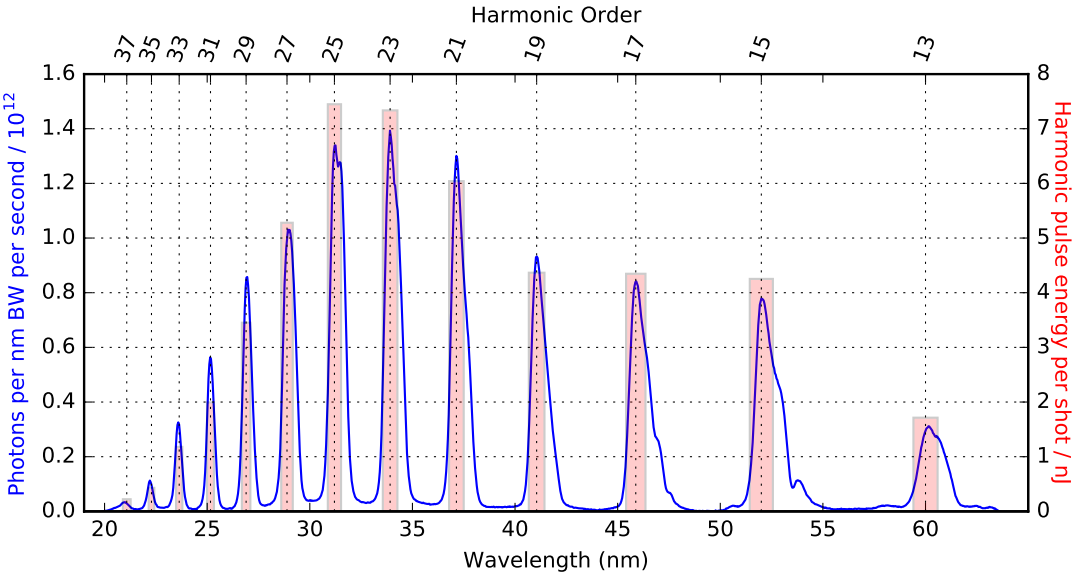

Figure 2.9: **Spectrum optimized for the 29^{th} harmonic.** A typical spectrum found when optimizing for high order harmonics. Here, the 37^{th} harmonic is reached, giving photons with 59 eV of energy. The harmonic peaks are clearly isolated, indicating the generation of an attosecond pulse train. For several harmonics, a double peak structure is observed, which is attributed to the separate contributions of long and short trajectories.

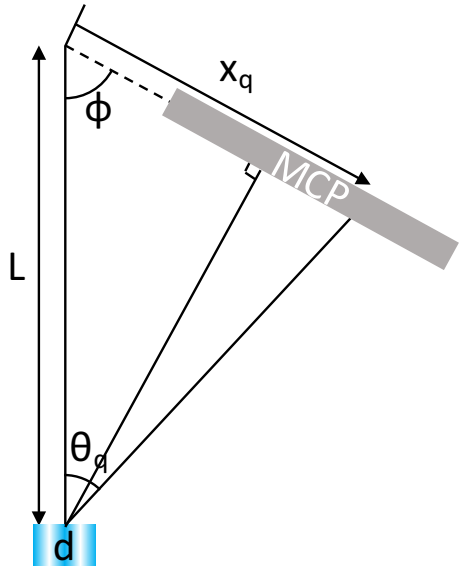

Figure 2.10: **Diagram of the XUV Spectrometer.** The relative position on the MCP depends on the wavelength of the incident light and on the period of the grating, as well as parametrically on the geometry of the spectrometer.

intersect the MCP at a relative position:

$$x_q = \frac{L\sin\theta_q}{\sin(180^\circ - \phi - \theta_q)} \tag{2.26a}$$

$$= \frac{L\sin\theta_q}{\sin\phi\cos\theta_q + \cos\phi\sin\theta_q} \tag{2.26b}$$

$$= \frac{L}{\sin\phi\sqrt{\left(\frac{dq}{\lambda_0}\right)^2 - 1} + \cos\phi}. \tag{2.26c}$$

From a raw spectrum, we find n peaks at positions $x_i + x_0$ ($i \in [0, n-1]$), which we attribute to diffraction of harmonics of order $q_i = q_0 + 2i$. A nonlinear least-squares fit is used to find the parameters L, ϕ, x_0, and q_0 needed for calibration (d and λ_0 can be set to the known values or also extracted). We find that the first imaged harmonic order is 13. This is verified by adding a second Al filter in series, as its cutoff for transmission lies just above the 13^{th} harmonic [80].

The photon flux is calibrated by measuring the integrated yield of the harmonic beam after the first Al filter with a calibrated XUV photodiode (Opto Diode AXUV100Al). The measured spectrum is not measured below the 13^{th} harmonic, but we do not expect any contribution from this missing information as the Al-coated photodiode should not be sensitive to it.

We find that we are able to generate beyond 10^{12} photons per nanometer bandwidth per second, giving nJ level pulse energies per harmonic per shot, after full filtration of the driving infrared light using two rejection mirrors and an Aluminum filter. Focusing this energy to a spot size of 1-10 μm should help reach XUV intensities in the range of $10^{11-13}\,\mathrm{W/cm^2}$, corresponding to >1% absorption probabilities for a $\sigma = 1\,\mathrm{MB}$ transition. These orders of transitions probabilities are necessary to look at nonlinear processes, including those measured in any time-resolved pump-probe experiment.

Focusing on low order harmonics that can be used to resonantly pump neutral excited states in small molecules, we can also measure the flux of the 5^{th} harmonic and of the 9^{th} harmonic. Using two bandpass filters centered at 157 nm (Acton Optics and Coatings) and a calibrated bare XUV photodiode (Opto Diode AXUV100), the 5^{th} harmonic flux can be directly measured. Pulse energies greater than 200 nJ were measured after two infrared separation mirrors and one bandpass filter (with modest transmission, as discussed in the following section) using 25-30 Torr of Argon gas in a 6 cm gas cell with a 6 m focus and driving with 20 mJ of infrared light. To find this optimum, the focus was moved downstream such that the spot size in the gas cell was larger. As discussed in section 2.1 and as seen in fig. 2.11, at these high pressures of 25-30 Torr, the 5^{th} harmonic flux saturates while the high orders are mostly reabsorbed. A similar saturating pressure-dependence was found for the 9^{th} harmonic generated in Argon, as measured by monitoring the ionization rate of Xenon gas using an Indium metal filter (as described below).

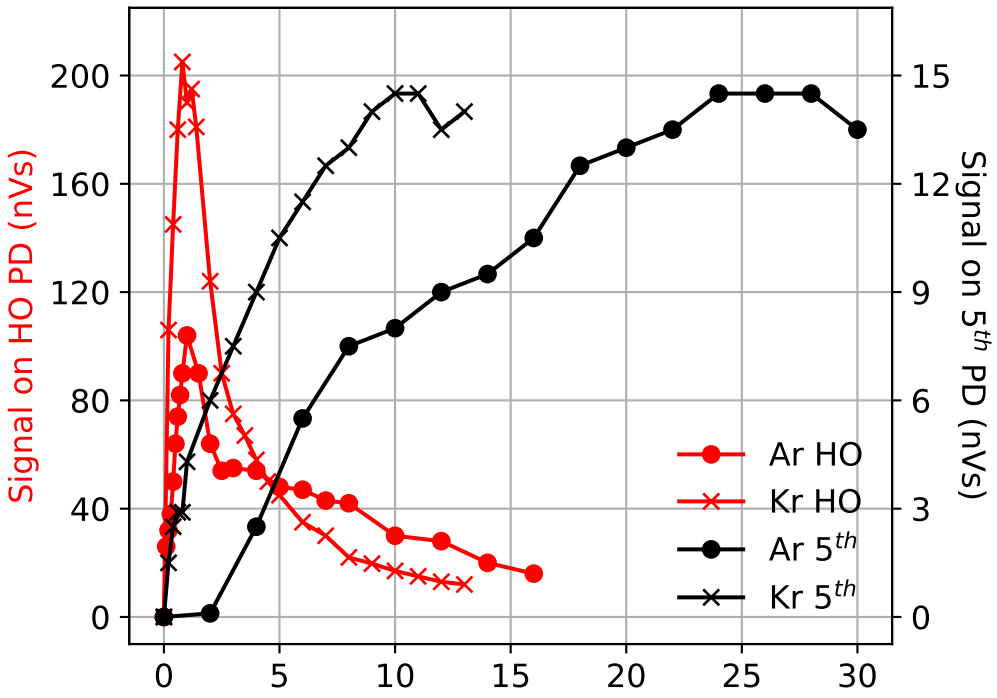

Figure 2.11: **Pressure Scan of Low and High Order Harmonics.** The high order harmonics ($q > 13$), as measured by an Aluminum coated photodiode, have an optimum pressure of several Torr, as higher pressures lead to increased reabsorption. The 5^{th} harmonic, which lies energetically much below the ionization potential of the generating Ar or Kr gas, saturates at higher pressures. These data were taken with 20 mJ, 27 fs driving pulses, a 6 cm gas cell, a 6 m focus, and a focus position optimized for high order harmonics.

Besides studying ultrafast dynamics, a bright VUV/XUV laser based source also has applications in the growing field of free electron lasers (FEL). One of the original goals for the design and implementation of this beamline was to study the feasibility of using an HHG source as a seed for a next-generation FEL [81, 82]. While these FELs are expected to operate in the 100 kHz to 1 MHz range, beyond the 1 kHz repetition rate used here, the work here shows that it is possible to reach the high XUV pulse energies needed for seeding even at 1 kHz. However, pushing for two or three more orders of magnitude may bring about new challenges analogous to the average power issues faced here.

2.4 Spectral Filtering and Time Delay

Depending on the experiment, spectral filtering of the frequency comb output by HHG is needed. For example, in photoelectron spectroscopy as described in section 1.4, knowledge of

the energy of the probe photon is crucial as it is directly related to the kinetic energy of the measured photoelectron. Since all materials will be absorbing in the VUV and XUV regions, much less spectral control is available than, for example, in the infrared and optical regions. Still, several options are available. Going to the Fourier plane using a diffraction grating can help select just one harmonic. However, the resulting beam will suffer from smearing in both the time and spatial dimensions when focused, unless a complicated and inefficient time-compensating design is constructed [83].

Filtering optics

Metal foils are available as bandpass filters in the XUV region [80]. Some absorption is still present, so these foils must be kept thin (100-200 nm). Three filters available in the energy range of the harmonics generated above are aluminum, indium, and tin. For the energies considered here, Aluminum filters act as high-pass filters, ideally transmitting harmonics of order 13 and above at the 70% level for a 150 nm thickness. Indium filters have a small transmission window which isolates the 9^{th} harmonic only, although the peak transmission is still below 40% at best. A tin filter can also be used, transmitting the 13^{th} and 15^{th} harmonic at a $\sim 30\%$ level. These filters also have strong rejection of any residual infrared light. In practice, the transmission levels for all of these filters becomes quickly reduced. Upon installation, these metal filters can quickly become oxidized, and oxidation layers just several atoms thick can reduce the measured transmission half or more.

For lower order harmonics, fluoride windows can be used as transmission optics. MgF_2 and LiF_2 for example, efficiently transmit the driving infrared light as well as the low order harmonics up to $q = 7$. These optics can also be coated for the selection of a single harmonic: an MgF_2 crystal window can be coated to be highly reflective at 780 and 260 nm, leading to isolation of the 5^{th} harmonic with 10-20% transmission. In addition, these windows provide dispersion which can be used by to temporally isolate harmonics. The delay Δt between a pulse traveling through a dispersive medium and a reference pulse depends on the index of refraction n and the chromatic dispersion $\frac{\partial n}{\partial \lambda}$:

$$\Delta t = L\left(\frac{1}{v_g} - \frac{1}{c}\right), \tag{2.27a}$$

$$v_g = \frac{c}{n - \lambda\frac{\partial n}{\partial \lambda}}, \tag{2.27b}$$

where v_g is the group delay velocity. For fluoride windows, the group delay velocity will decrease as the photon energy increases towards the VUV. As such, an infrared pulse will exit the medium first, followed by the 3^{rd} harmonic, and finally by the 5^{th} and 7^{th} harmonics [84]. If the infrared and UV light are not resonant with a target in its molecular ground state, their contribution to a measured experimental signal can be ignored.

Since we require both a pump and a probe arm, each with its own spectral content which may vary experiment to experiment, a filter chamber was constructed and placed after the

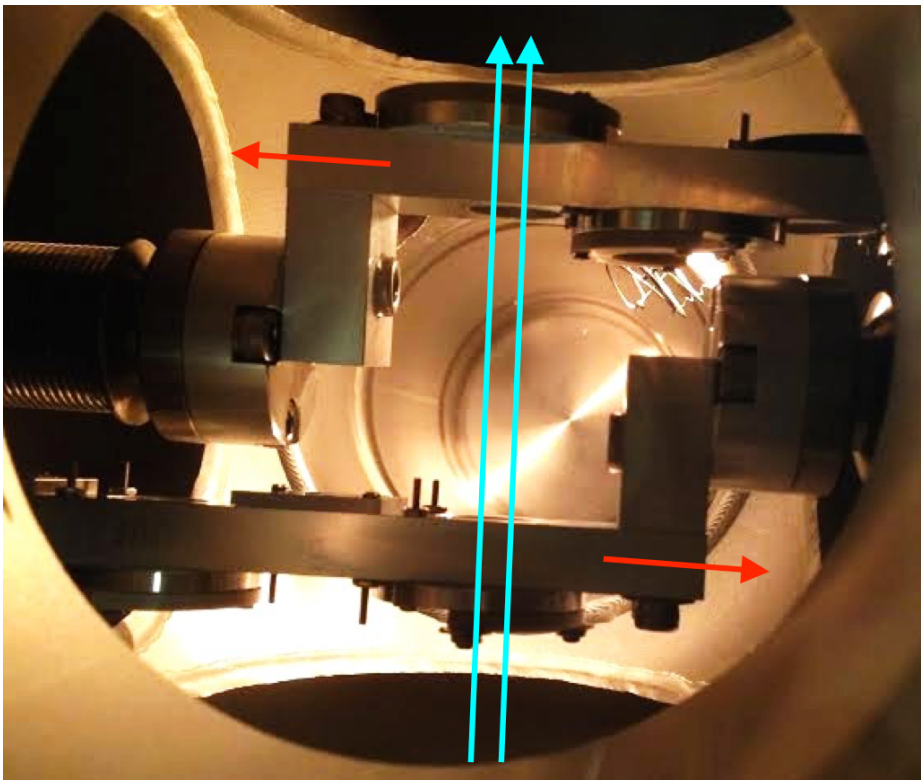

Figure 2.12: **D-shaped filter holders.** Two arms holding D-shaped filters can be scanned along the red arrows parallel to the beam direction to select various filter combinations. The incoming HHG beam will be split into two arms spatially (teal arrows), each with different spectral content depending on the filters used.

infrared rejection optics. Two arms hold up to 4 filters each. These arms can be coarsely adjusted to select the appropriate filter and finely adjusted using a piezo-electric motor for proper alignment (see section 3.1). Using two D-shaped filters, both halves of the harmonic beam mode can separately be spectrally filtered.

Coated mirrors

After the metal and window filters, mirrors can also be used for spectral filtering [85]. Although losses will occur for any reflection in the VUV and XUV, a minimum of one mirror reflection is needed to focus the beam in order to achieve high intensities on target. At higher energies, multilayer mirror technology provides the ability to select a given harmonic with good contrast and full control on the reflected wavelength [86]. At lower energies, less options are available. While a rich database exists for transmission and reflectivities above 30 eV, the VUV and XUV region below this energy has not been explored, due to the difficulties in accurate calculation (excited state resonances) and measurement (lack of sources and,

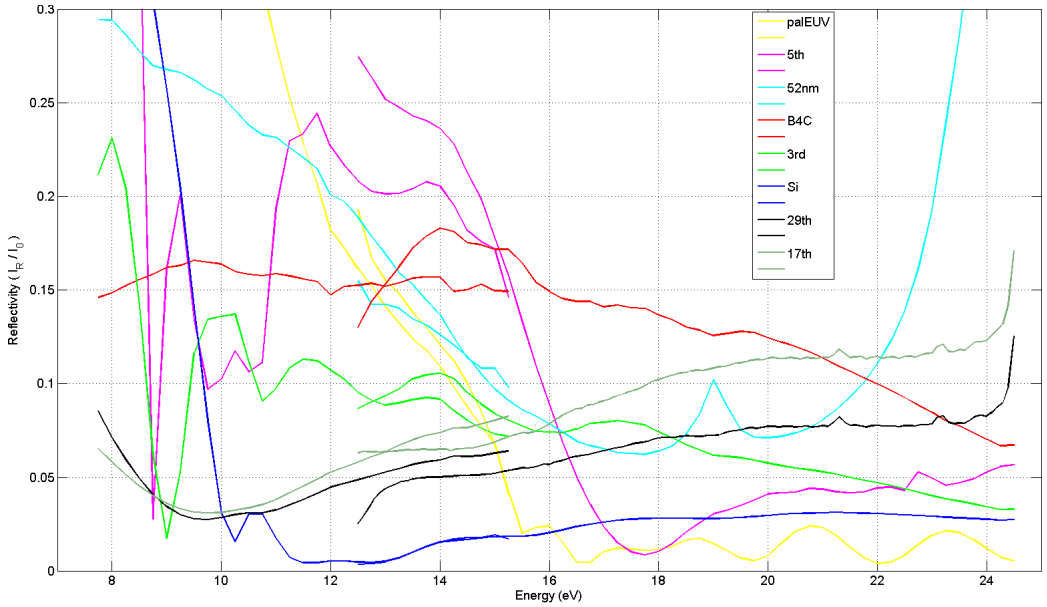

Figure 2.13: **Mirror reflectivities.** The near normal incidence reflectivities of various substrates and coated mirrors are reported: (yellow, palEUV), EUV protected Aluminum, Lattice Electro Optics; (pink, 5th) 160 nm dielectric mirror, Layertec; (teal, 52nm) SiC/Mg multilayer mirror for 52 nm, Center for X-ray Optics; (red, B_4C) single layer B_4C/Cr stack, Center for X-ray Optics; (green, 3rd) 270 nm dielectric coated mirror, Lattice Electro Optics; (blue, Si) bare Silicon substrate; (black, 29th) SiC/Mg multilayer mirror for 27 nm, Center for X-ray Optics; and (gray, 17th) SiC/Mg multilayer mirror for 47 nm, Center for X-ray Optics. The beamline flux at each energy is measured using the same photodiode (Opto Diode AXUV100G) before and after reflection. Two overlapping energy ranges are measured for each mirror, each using different mechanisms for beamline second harmonic rejection. The first between 7.5 and 15.25 eV uses 115 mm propagation through a gas cell filled with 30 Torr of Argon gas, while the second between 12.5 and 24.5 eV uses 20 Torr of Helium.

as currently discussed, optics). Using the Advanced Light Source synchrotron at Lawrence Berkeley National Laboratory, we have measured the reflectivities of various substrates and coated mirrors at normal incidence in the energy range of 7.5 to 24.5 eV and report them in fig. 2.13 [85]. At the 5^{th} harmonic, a commercial mirror (Layertec) provides >90% reflectivity over a small window while rejecting photons below and above this energy. The multilayer mirrors have >30% reflection at the energy they are designed for, but still provide some reflection within the range of energies measured here. The single layer B_4C mirrors, designed for broad reflection, do show >15% reflection over a large energy range. However, the reflectivity of this particular mirror, which spent 6 months in a desiccator, was half of that reported for a freshly coated substrate [87], indicating degradation of the nanometer scale coating. Although small (∼10%) a dielectric mirror with a coating for 270 nm also showed a broad reflection spectrum.

Split-Mirror Interferometer

Similarly to the D-shaped filters, two D-shaped mirrors can be set side by side for separate spectral shaping of the pump and probe arms. In addition, the relative position of these mirrors along the beam propagation direction allows for temporal separation of the pump and probe arms. The experiments described here make use of such a split-mirror interferometer (SMI) [88]. To minimize mirror reflections and losses, the mirrors of the SMI are curved, providing focusing and time delay with a single reflection. An $f = 10\,\mathrm{cm}$ focusing geometry is chosen, giving enough room for the experimental spectrometer described in the next chapter while also providing a tight focus. Adding time delay to one arm will move its focus relative to the other. However, the estimated Rayleigh range for the focused harmonic light is on the order of 1 mm, much larger than the 50 μm needed for a time delay scan of 300 fs. Having the focusing on the SMI provides great interferometric stability, since the only source of phase noise is the split-mirror itself.

2.5 Non-linear XUV optics in Neon

The high intensities that can be reached with this HHG source also enable studies in non-linear XUV optics. As a test case, we looked at non-linear effects in Neon using split mirrors coated for the 17^{th} and 29^{th} harmonics at 27.0 and 46.1 eV, respectively. Absorption of a photon at either of these energies can lead to the ionization continuum of Ne^+, as seen in fig. 2.14. Subsequent absorption of a 29^{th} harmonic photon is enough to reach the double ionization continuum. Such sequential two-photon double ionization is a second order non-linear process. A distinct process, non-sequential two-photon ionization, is also open with two photons of the 17^{th} harmonic only, although its cross-section should be much smaller than the sequential pathway [89, 90].

Additionally, the 29^{th} harmonic is close to resonance with the $1s^2 2s^1 2p^6 3p^1$ core-excited state. This state lies in the ionic continuum and should thus auto-ionize on the femtosecond time scale [91]. However, stimulated emission at 27.0 eV, corresponding to the 17^{th} harmonic, can cause a $2p \rightarrow 2s$ transition to the $1s^2 2s^2 2p^5 3p^1$ excited state, which should eventually fluoresce back to the ground state through the $1s^2 2s^2 2p^5 3s^1$ state. The population of the $1s^2 2s^2 2p^5 3p^1$ excited state with the absorption of one photon and the emission of another constitutes a Raman process. While these processes have been extensively studied in the microwave, infrared, and optical regions, with final excitations along spin, rotational, or vibrational degrees of freedom, they have thus far not been observed in the XUV or X-ray region, where the final excitation can now be electronic. Using broadband XUV or X-ray pulses, these electronic Raman transitions could populate neutral electronic wavepackets localized in a molecule if the intermediate state corresponds to excitation of a core electron. Such excitations would be useful to study coherent electron dynamics in molecular systems.

The population of the $1s^2 2s^2 2p^5 3p^1$ excited state through electronic Raman redistribution was investigated by looking for the characteristic fluorescence of the $3p \rightarrow 3s$ transition. A

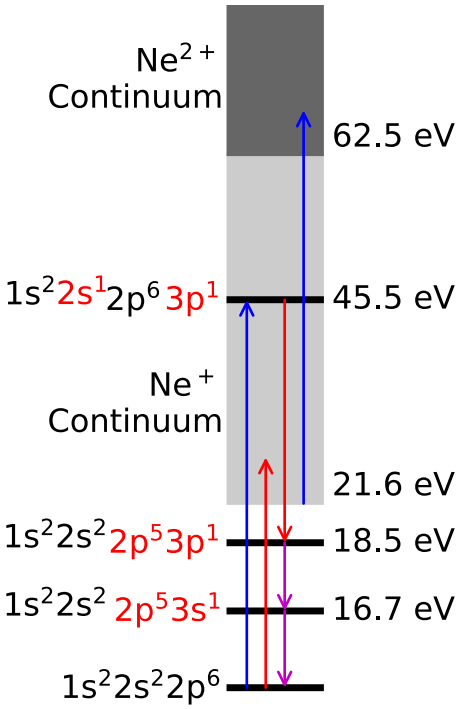

Figure 2.14: **Non-linear XUV optics in Neon.** With the 17^{th} and 29^{th} harmonics, two-photon sequential absorption is possible. Electronic Raman excitation of the dark $1s^2 2s^2 2p^5 3p^1$ state, another second order non-linear process, should also be energetically allowed, although such processes have not yet been observed.

curved silver mirror was placed near the harmonic focus to collect and image fluorescence onto an avalanche photodiode behind a vacuum window and a narrow band filter transmitting 689 nm. However, no signal was observed above noise levels. This could result from a variety of issues, including insufficient XUV intensities and missed resonances between the used harmonics and the electronic states.

A time-of-flight mass spectrometer was used to investigate ionization and double ionization of Neon. Briefly (more details on the experimental end stations are available in the next chapter), after ionization of Neon from a gas jet, the resulting ions are accelerated with DC electric fields towards a microchannel plate (MCP) detectors, leading to measurable electrical pulses. The time-of-flight of a charged particle will be proportional to the square root of its mass to charge ratio, such that Ne^+ and Ne^{2+} can be distinguished. The beam impingent on the split mirror was scanned, giving data sets for ion yields with the beam fully on the 17^{th} harmonic mirror, fully on the 29^{th} harmonic mirror, or split evenly between the mirrors. The ion yields are reported in table 2.1. The flux of the 17^{th} and 29^{th} harmonics were relatively equal, as measured with the XUV spectrometer, which does not account for the reflection from the focusing mirror. We find only small variations in the

Table 2.1: **Ionization and double ionization rates of Neon using the high order harmonics.** Using an $f = 10\,\text{cm}$ mirror with two halves coated for the 17^{th} and 29^{th} harmonics, the signal rates of Ne^+ and Ne^{2+} are measured for various positions of the beam on the mirror. The high signal rate of Ne^+ were measured by integrating the pulses coming from the MCP with a boxcar integrator, although this does not yield absolute rates. For Ne^{2+}, the rate was low enough that individual events could be measured using a time-to-digital converter. Contributions from both ^{20}Ne and ^{22}Ne were observed and combined.

Harmonics	17^{th}	29^{th}	17^{th}+29^{th}
Ne^+ (arb. units)	128.7	114.9	126.4
Ne^{2+} (counts/sec)	0.08	2.35	1.04

rate of single ionization by changing the ratio of the beam on each mirror surface, indicating that the probabilities for ionization with either harmonic are similar. For double ionization channel, we measure negligible amounts of Ne^{2+} (within the noise) with the 17^{th} harmonic only, while the amount of counts with the beam fully on the 29^{th} harmonic mirror is roughly double that with the beam split between the half-mirrors. This factor of 2 is reasonable, as we can expect both harmonics to contribute similarly to the first step of the sequential process, namely the single ionization, while only the 29^{th} harmonic contributes to the second step. The non-sequential double ionization pathway was not measured. The absence of this pathway might indicate that the intensities, while high enough to lead to sequential double ionization, may not be enough for the Raman process.

Chapter 3

Experimental End Station: Time-Resolved Photoelectron Spectroscopy

Armed with spectrally and temporally tunable pump and probe pulses, the next step is to implement an instrument capable of measuring an observable. As discussed in section 1.4, many schemes have been developed, all with their own strengths and weaknesses. The high photon energies (as compared to visible or infrared light) achieved with the HHG beamline are well suited for molecular ionization and thus for charged particle detection using, for example, micro-channel plates [92].

At the lowest level of detail, the pump-probe time delay dependent ionization yield can be measured. The ionization rate of the reactants and products for a constant ionizing light source should, in general, defer from one another, such that this measurement should yield a timescale related to the reaction rate. Still, measured changes may be due to one or several of the intermediate steps in the reaction rather than to its completion, and thus this simple measurement may not reveal much information. Going one step further, an ion time-of-flight (ToF) spectrometer, which resolves ion species by their mass-to-charge ratio, is more differential, allowing for the measurement of the time-dependent ionization yield to each final ion channel [93]. Although this one-to-one mapping does fail just as the one above, many experiments make use of this technique and find characteristic timescales for either the disappearance of the parent ion or the appearance of a fragment ion, both of which can be linked to, for example, either fragmentation or electronic relaxation as a result of excited state dynamics [88].

The next increase in measurement differentiability comes about from measuring the momentum (or energy) distributions of the resulting ions and/or photoelectrons. For photoionization to a dissociating cationic state, the resultant kinetic energy release (KER) will depend on both the electronic state and nuclear geometry, as seen in fig. 1.5. However, while predicting the measured KER given these PESs and a localized excited wavepacket on a given electronic state, the inverse is more difficult. First, the measured KER also depends

on wavepacket dynamics on the cation surfaces. Second, this mapping may not necessarily be one-to-one, especially when dealing with PESs of dimension greater than one. The measurement of photoelectron kinetic energies can yield similar information while not requiring simulation of cation dynamics. Time-resolved photoelectron spectroscopy (TRPES) has thus been a popular experimental approach to study ultrafast molecular dynamics [31].

The measurement of an ion or electron momentum distribution can be achieved in several ways. Direct measurement of the full three dimensional distribution is difficult, mainly since the available detectors are two dimensional. Still, it has been achieved by again making use of the time-of-flight, either using a slicing approach [94, 95], acquiring portions of the distribution one at a time with detector pulsing, or delay-line anode detectors, which are able to detect individual particles with position and time sensitivity [96]. Due to its detection of individual particles, the latter has been used in so called Reaction Microscope spectrometers, measuring the momenta of all of the photoions and photoelectrons resulting from a single molecule in coincidence and again giving a much deeper set of information [97]. This technique, however, is limited in the amount of events that can occur for each laser shot in order to avoid false coincidences. The slicing technique has its own limitations, in that acquisition time is greatly lengthened due to having to take individual measurements at each time slice.

Velocity Map Imaging (VMI) has been successfully used to indirectly measure these full momentum distributions [98]. Similarly to the slicing approach, appropriate physical design and voltages of the spectrometer, as discussed in section 3.1, allows for the creation of a Newton's sphere accelerated to high enough energies to efficiently trigger a micro-channel plate (MCP) detector [92]. In VMI, however, the entirety of this Newton's sphere is measured at the detector plane, giving a measurement of the projection of the full three dimensional momentum distribution, as shown in fig. 3.1. Assuming certain symmetry constraints are upheld, the full distribution can be recuperated from its projected measurement [100]. While some limitations exist, the VMI approach suits itself well with the light source presented in chapter 2 and was used for the experiments presented in the following chapters.

3.1 Velocity Map Imaging Spectrometer

Expanding on the Wiley-McLaren time-of-flight spectrometer [93], the design of a spectrometer based on electrostatic lenses was shown to allow for velocity map imaging [98], where all charged particles born within some interaction volume with the same initial momentum vector are imaged to the same point on a detector, as shown in fig. 3.2. The electrostatic lenses lead to stronger deflection of particle trajectories for particles near their edge, and are thus able to focus particles born at different positions to a single position. By careful tuning of the distances between the three electrostatic plates, the size of the lenses, and the ratio of the applied voltages, a condition can be found where the lenses work at every initial particle energy, and where there is a clear mapping, to a high degree of accuracy, between the initial projected momentum $v_\perp$ and the final position on the detector, measured as the radius from

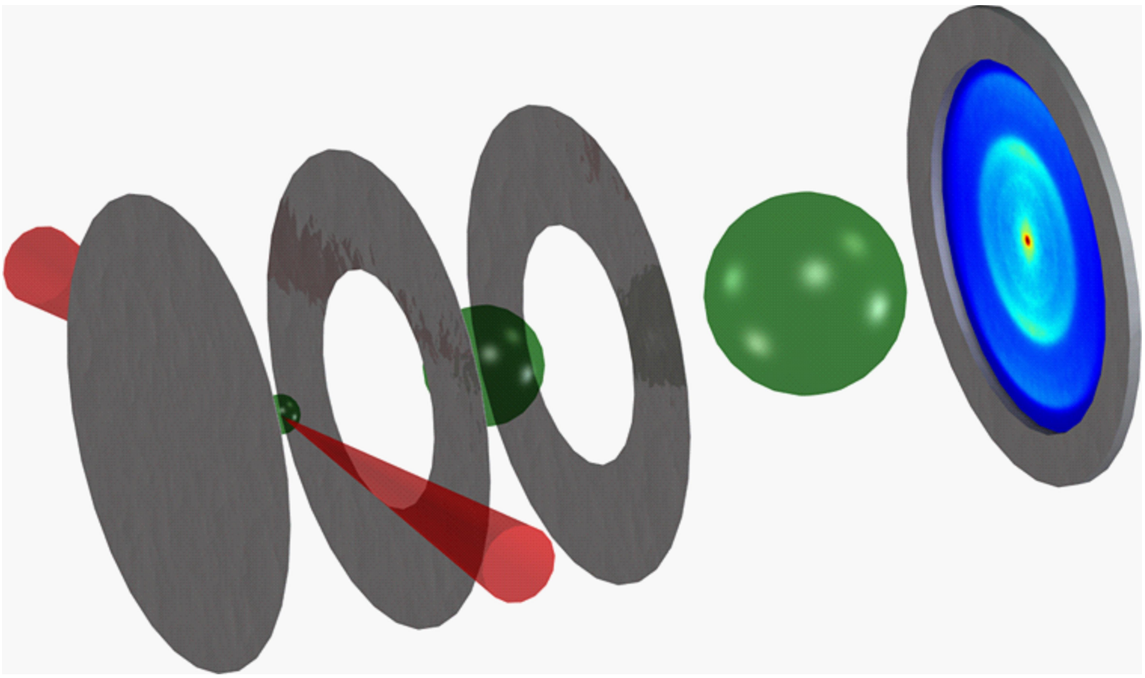

Figure 3.1: **Schematic of Velocity Map Imaging.** Light (pictured in red) is focused into the interaction region where it ionizes gas molecules, which are left to expand, imprinting their momentum distribution into their spatial distribution, while being accelerated towards the particle detector. A projection of the three dimensional spatial distribution will be measured on the two dimensional detector. Figure adapted from [99].

center R_d:

$$R_d \propto v_\perp, \tag{3.1a}$$
$$E_\perp = \alpha R_d^2. \tag{3.1b}$$

Angle information is also preserved due to the cylindrical symmetry. Beyond the simple energetic distribution, the angular information can also be useful. The ionization rate of a molecular state, in general, will depend on relative orientation of the molecule with respect to the polarization of the light due to the appearance of $\vec{r}$ in the dipole matrix element. Ionized molecules may have an anisotropic distribution due either to selection rules of the excitation step in a pump-probe experiment or due to systematic alignment in the laboratory frame through, for example, non-adiabatic alignment [75], and thus the angular asymmetry in the ionization rate, which will depend on the instantaneous state of the system, can be measured. Photoelectron angular distributions also hold rich information, as they will depend on the symmetry of the molecular orbital of the ionized electron [102]. While two electronic states may be degenerate and thus result in similar photoelectron kinetic energies, their angular distributions can vary greatly, allowing for the observation of population transfer from one

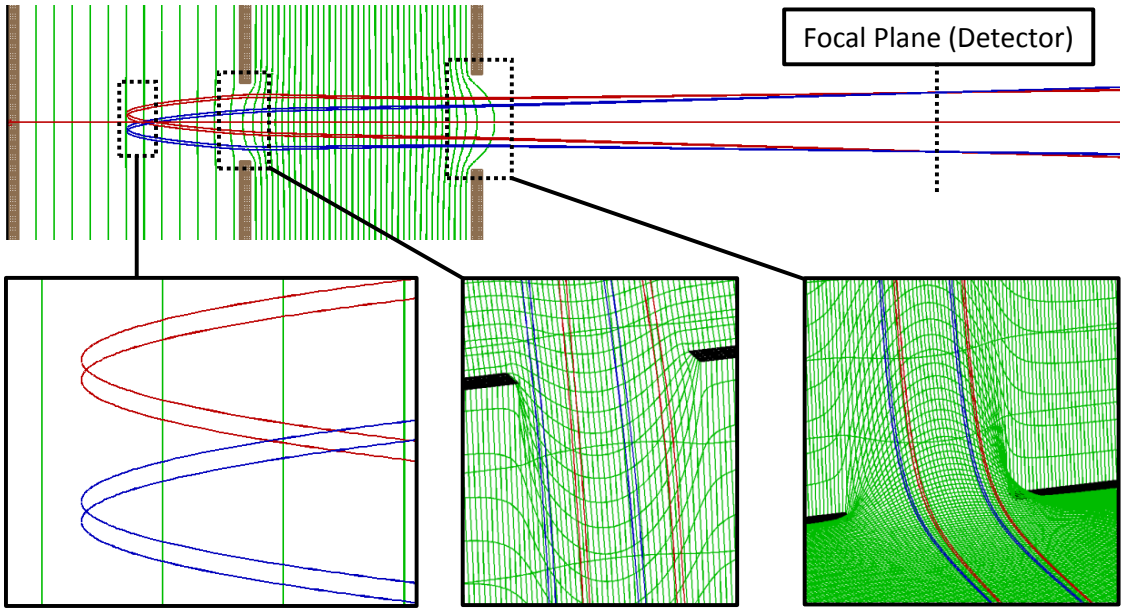

Figure 3.2: **Velocity Map Imaging with Three Electrostatic Plates.** The eight trajectories resulting from two different initial velocity vectors at four different initial positions are shown in a cut of the VMI spectrometer, which has cylindrical symmetry. Due to two electrostatic lenses, these eight trajectories are imaged onto only two positions at the detector plane, one for each initial velocity vector. Electrostatic potentials and charged particle trajectories were found using SIMION 8.1 [101]. Figure adapted from [99].

state to the other in the time domain through the measurement of angular distributions [31, 103].

Physical Implementation

Several considerations were taken when designing our VMI spectrometer. Using VUV and XUV light, we can expect both photoion and photoelectrons with energies up to the 10s of eV, so the detector should be optimized for the best energy resolution at this range of energies. These photons are energetic enough to be above the work function of any metals in the spectrometer, the chamber, and even the detector, and thus any stray photons can create electrons. The spectrometer should then be ideally light tight and also reject electrons created outside of the interaction volume. Additionally, some of these photons are energetic enough (>10 eV) to ionize typical molecules with a single photon. In contrast to many past TRPES experiments, this leads to the possibility to create signal away from the focus. In a perfectly back-focusing geometry, the incoming beam will cross the interaction volume and generate unwanted signal. To avoid this, the incoming beam was positioned between the ground and extractor plates and the back-focusing mirror was tilted such that the reflected

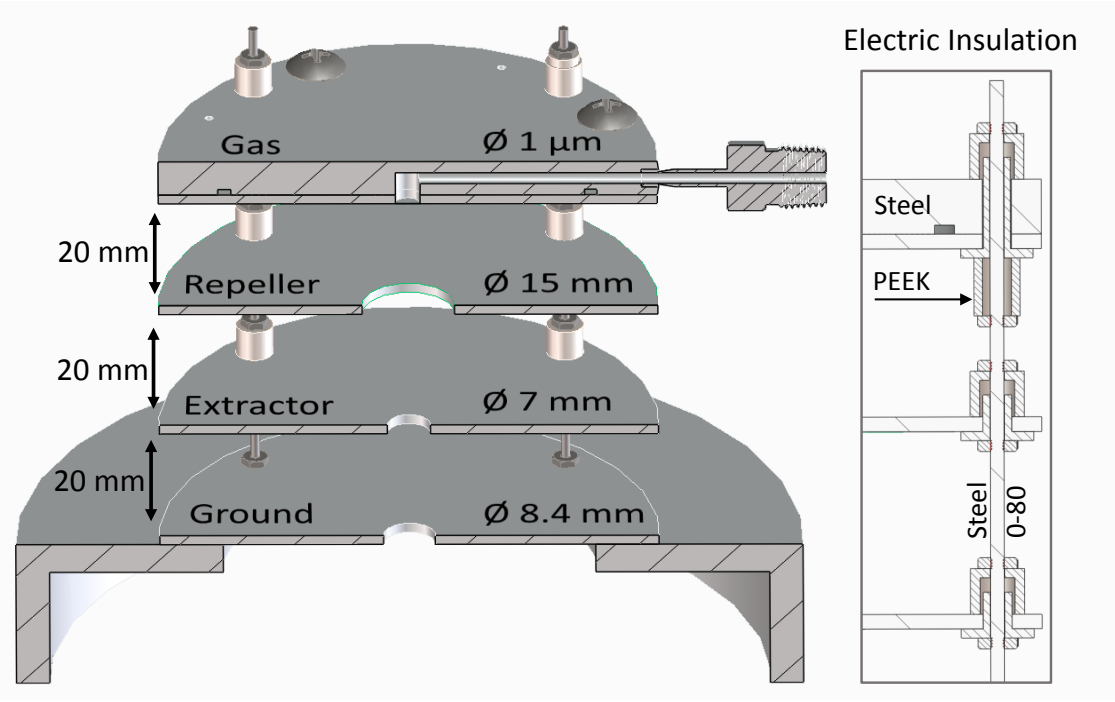

Figure 3.3: **Spectrometer Electrostatic Plate Assembly.** The four plate design allows for the trapping of stray ions, while also having a built-in gas delivery. Voltages of -4700 V, -5000 V, -3315 V, and 0V on the gas, repeller, extractor, and ground plates, respectively, allowed for efficient velocity map imaging with a ∼1 m focus for energies up to ∼10 eV. Figure adapted from [99].

beam was positioned between the repeller and extractor plates. Charged particles ionized by the incoming beam were then born at a lower potential than those born at the focus, such that this energy was not enough to trigger the MCP efficiently. This resulted in a slight tilt of the focused beam direction with respect to the spectrometer. Several effects and uses of this tilt are discussed later in this section.

Our initial design used the standard three plate scheme (repeller, extractor, and ground) [98]. However, we noticed that, while imaging electrons, ions would be accelerated upwards towards the repeller and create electrons that would then be detected. Instead, we switched to a four plate design, as shown in fig. 3.3. In electron operation, ions will go through the repeller plate and will then be slowed down as the potential increases towards the gas plate. Target gas is let into the interaction volume through a feed-through built into the gas plate, and let into the chamber through a 1 μm nozzle. The distances between the plates and the size of the plate holes were tuned along with the applied voltages to maximize energy resolution below 10 eV.

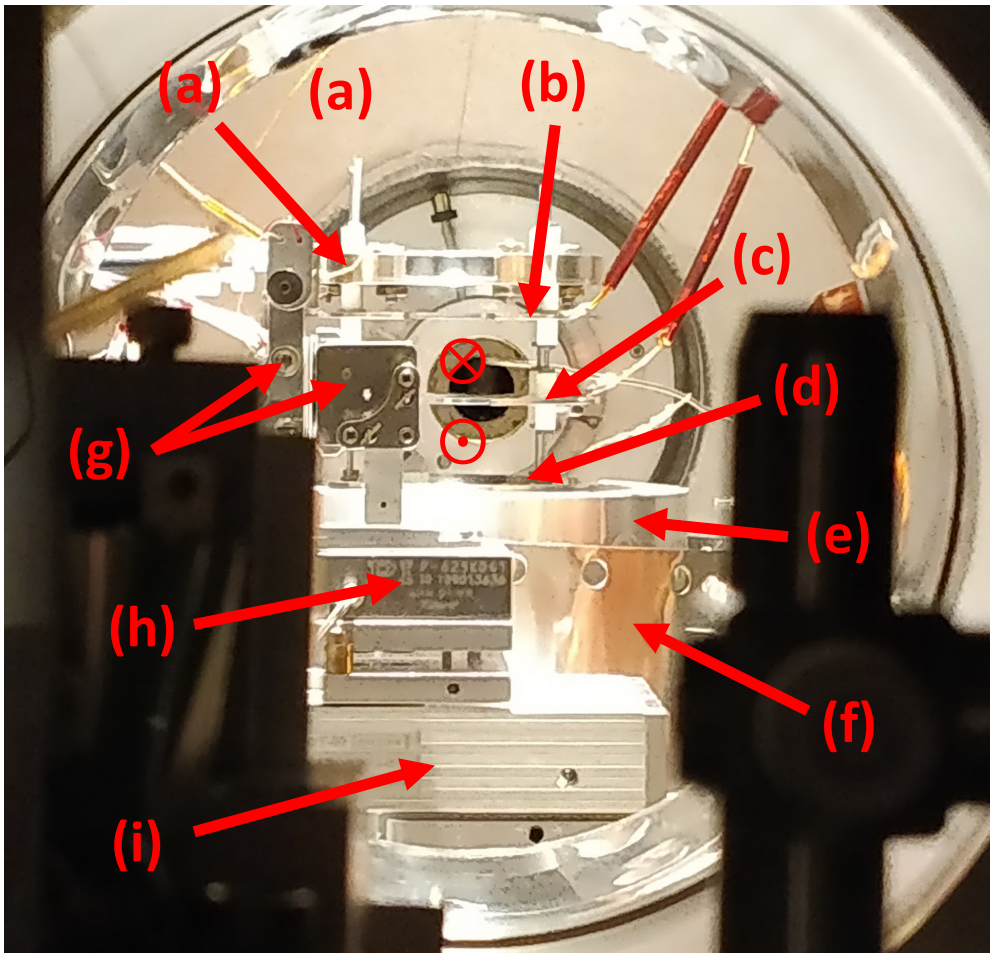

Figure 3.4: **VMI Spectrometer in Magnus Chamber.** The spectrometer sits in the center of the Magnus chamber, as seen from the downstream exit port. The $\odot$ and $\otimes$ symbols indicate the beam incoming to the SMI and outgoing towards the interaction region, respectively. (a) Gas plate with built in gas nozzle, (b) Repeller plate, (c) Extractor plate, (d) Ground plate, with an enclosed 1 m drift tube below it, (e) Isolated drift tube, (f) Mu-metal shield isolating the drift tube from magnetic fields that would affect electron trajectories, (g) Mirror holders for the SMI, (h) "PI" stage for SMI delay, and (i) "Micos" stage for SMI translation.

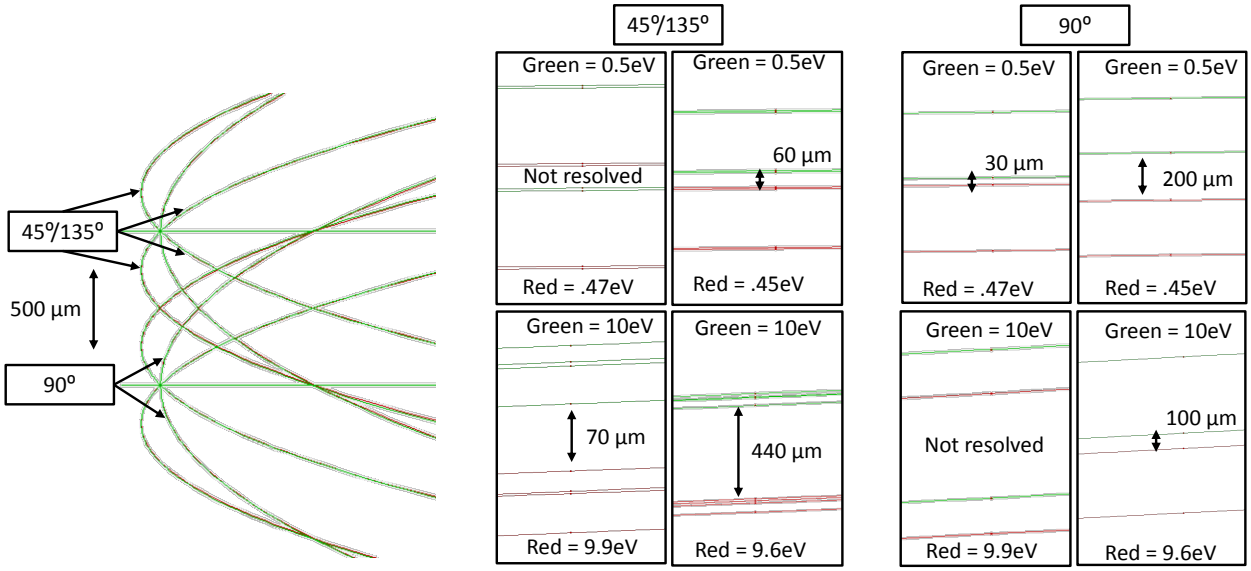

Figure 3.5: **VMI Energy Resolution.** SIMION trajectories of particles of varying kinetic energy, initial momentum direction, and initial position at the detector plane. The 500 μm source distance limits the energy resolution of the spectrometer, with particles emitted at one end of the source and one energy being imaged to the same position as those emitted at the other end of the source and with a slightly different energy. The resolution at 0.5 eV is greater than 0.05 eV, while that at 10 eV is greater than 0.4 eV. Figure adapted from [99].

Resolution

Theoretical calculations of our Rayleigh range using $z_R = \frac{4\lambda}{\pi}(\frac{F}{D})^2$ at various harmonic wavelengths and estimation using the spatial imaging mode of our spectrometer discussed below in section 3.1 yielded values on the order of 500 μm. Spatial resolution at the detector is limited by the channel size of the MCP, which is on the order of 10 μm, and by the phosphor screen, which causes additional blurring of an individual particle hit. Numerical estimation of the spectrometer's energy resolution was carried out in SIMION [101] by creating two charged particle sources separated by this Rayleigh range of 500 μm. At each source, particles of various neighboring energies and directed in 45° angular increments were spawned, and their trajectories were simulated. The spatial separation of the two sources leads to some range of positions that a particle with a given energy will cross the detector plane. Resolution for a given energy separation ΔE is determined to be achieved if these ranges of positions for two particle energies E and $E + \Delta E$ do not overlap and, ideally, are separated by an amount larger than the spatial resolution of the imaging system. The results of this simulation are shown in fig. 3.5, and reveal an energy resolution $\Delta E/E$ of roughly 5-10% at both 0.5 and 10 eV.

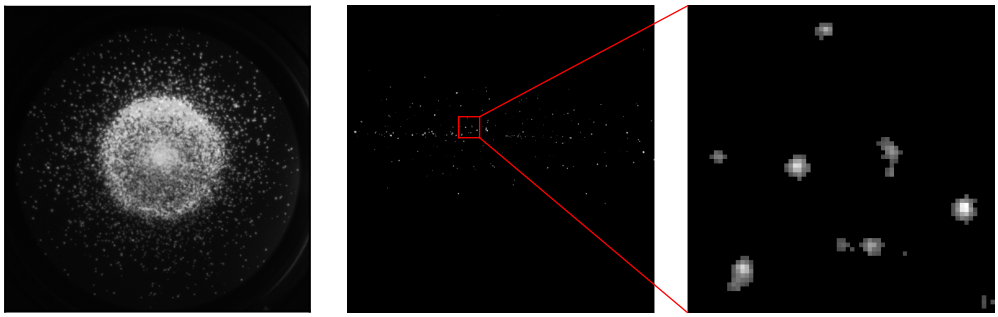

Figure 3.6: **Particle Hit Finding.** (a) A VMI image of O^+ ions from dissociated O_2 molecules following sequential absorption of two 5^{th} harmonic photons, acquired with a long exposure time. (b-c) A short exposure image shows that individual O^+ events can be observed.

Particle Hit Finding

Using the camera, the simple addition of many images (of either short or long individual exposures) can be used to record the spatial distribution of charged particles at the detector plane. However, this integration has several drawbacks which will result in errors in the measurement. Dark current at each pixel will result in an additional source of background. Using short exposures and putting a lower threshold limit can reduce the effect of dark current, but some hot pixels may still appear. The gain across the detector, in general, will not be constant, especially as the MCPs of the spectrometer age. Increasing the overall gain towards saturation by increasing the voltages supplied to the MCPs and to the phosphor screen alleviates this problem, but does not solve it completely. A solution to both of these issues is to use exposure times short enough that individual particle hits can be resolved for a single image, and to implement a particle hit finding algorithm. Hot pixels due to dark current that have survived the thresholding step can be identified as such, while each particle hit that has enough gain to be detected by such an algorithm will be contribute to the measured distribution equally. Furthermore, an increased resolution is possible: each particle hit will light up an $\sim N \times N$ area of camera pixels, but a hit finding algorithm can reduce this to the single pixel (or even sub-pixel) level through centroiding.

Such an algorithm requires that the exposure time for single images can be set low enough such that the probability of two particles on a single image being too close to distinguish is small. For a given exposure time T and assuming a uniform signal rate γ (with units of hits per unit time per unit area), the uniform hit density for one image will be $\rho = \gamma T$. We can approximate that the particle hits in our spectrometer are imaged as Gaussians, and find their mean width σ to be 1.58 pixels with a standard deviation of 0.37 pixels (see fig. 3.7). Using the Rayleigh criterion [104] of a local minimum of 81.1% of the peak heights and a Gaussian approximation to the Airy pattern, two peaks are said to be resolved if they are

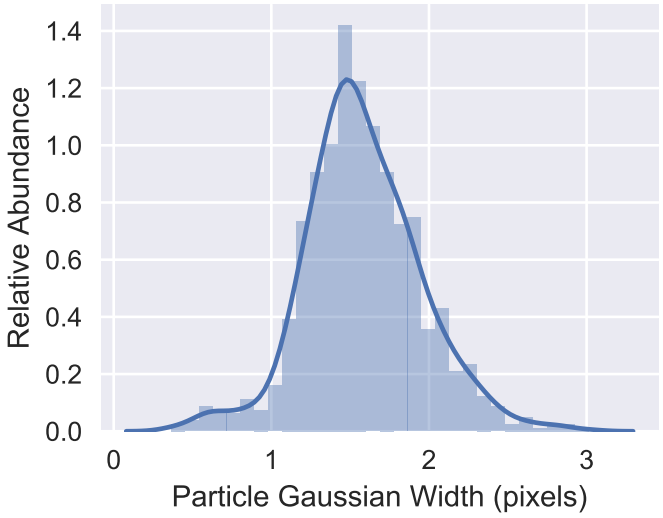

Figure 3.7: **Particle Hit Size Distribution.** The particle hits form small blobs on the detector which can be approximated as Gaussian peaks. The width of these peaks are normally distributed, with a width of 1.58±0.37 pixels.

separated by at least $2\sqrt{2\ln\frac{2}{0.811}}$ times their width, requiring a separation of at least 4 pixels between two hits for them to both be resolved. A given pixel will have 48 neighboring pixels which are less than 4 pixels away. The probabilities $P_i(n_i)$ and $P_o(n_o)$ of having n_i and n_o events at the center pixel and its 68 neighboring pixels, respectively, can be found using Poisson statistics:

$$P_i(n_i) = \frac{\rho^{n_i} e^{-\rho}}{n_i!} \tag{3.2a}$$

$$P_o(n_o) = \frac{(48\rho)^{n_o} e^{-48\rho}}{n_o!}. \tag{3.2b}$$

If a hit was found at a given pixel, there is a chance that it was the only event that occurred at that pixel and at its neighboring pixels for that image frame. However, there is also a chance that other events did occur and were not recorded by the hit finding algorithm. The probability that there were N events in the area surrounding the pixel where the hit was found (with $N \geq 1$) can be found to be:

$$P(N) = \sum_{k=1}^{N} P_i(k) P_o(N-k). \tag{3.3}$$

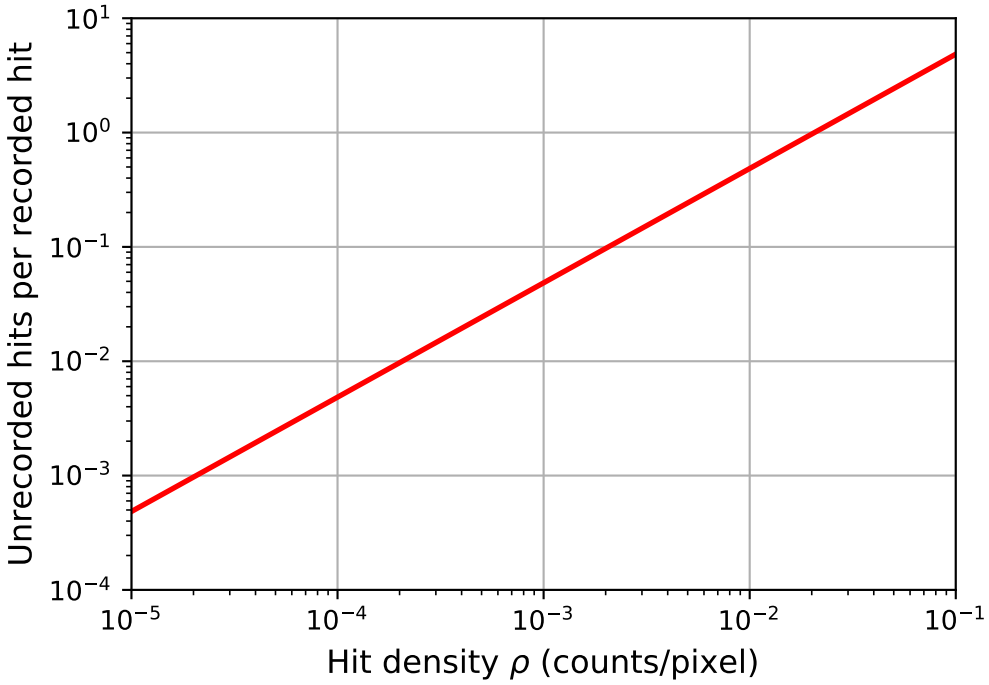

Figure 3.8: **Unrecorded hits for varying measured hit densities.** As the hit density increases, there is a growing probability that two or more hits will overlap spatially, such that the hit finding algorithm leads to an underestimation of the actual hit density. Below hit densities of 0.001 counts/pixel, corresponding to ∼1000 detected events per frame assuming a uniform hit density, the error will be on the few percent level or below.

We can then find the expected number of hits not recorded as a function of the hit density:

$$\langle N \rangle - 1 = \frac{\sum_{N=1}^{\infty} NP(N)}{\sum_{N=1}^{\infty} P(N)} \tag{3.4a}$$

$$= \frac{\sum_{N=1}^{\infty} NP(N)}{1 - P_i(0)}. \tag{3.4b}$$

The results of this calculation of the expected amount of unrecorded hits per recorded hit for varying measured hit densities ρ are shown in fig. 3.8, showing that a per-image hit density of 10^{-4} counts/pixel (giving ∼100 hits per image for a standard 1024×1024 image) will result in errors at the few tenths of a percent level. For a given experiment, reaching this per-image signal rate may require using low integration times.

We implemented a robust hit finding algorithm which was also optimized for computational complexity in order to work at low integration times that result in high frame rates. We require the hits to be infrequent, and the dark current is low enough that only a few

pixels without hits are as bright as those with a hit. This allows efficient computation using a sparse representation of the image. As a first step, lists of the horizontal and vertical positions as well as the value of each pixel with values above a certain threshold are found. These lists are typically only hundreds or thousands of elements long, greatly reducing the $\sim 10^6$ elements of a full image. Next, a median filter is applied, where the value at each pixel in the list above is set to the fifth largest of the nine values of that pixel and its direct neighbors. This filter removes the few isolated hot pixels remaining after the thresholding step. Next, a Gaussian convolution is performed, again on the sparse data only. Finally, all local maxima remaining in the image are found, and their positions are saved as a list of hits.

This algorithm was implemented in both C and Python (using the Cython library [105]). In either case, analyzing one image, including loading the image from a saved file, took on average 4 ms on a single core of a 2013 Macbook Pro with a 2.6 GHz Intel Core i5 processor. Direct analysis of an in-memory image without saving it and parallelization through the use of multiple cores for multiple subsequent images should allow for real-time analysis at frame rates greater than 1 kHz.

In practice, our camera had a maximum frame rate of ∼27 Hz, which was used for the subsequent experiments. The distribution of hit densities for each pixel of a representative data set taken at this frame rate is shown in fig. 3.9. A small amount of pixels have hit densities above 10^-3 counts/pixel, which will result in an underestimation of the signal at the few percent level according to fig. 3.8. For most of the pixels, this error will be at the tenth of a percent level or below. These percent errors are smaller than those expected from shot noise and other noise sources, and can thus safely be ignored.

Spatial Imaging with the Spectrometer

The spectrometer can also be used in a separate spatial imaging mode. Hard extraction through a similar high voltage on the repeller and grounding the extractor leads to a direct imaging of the projection of the initial ion source distribution, assuming that the kinetic energies of these ions is relatively low. A +5000 V potential on the repeller leads to a magnification on the order of ∼20, as predicted by SIMION simulations (see fig. 3.10) and as measured by scanning of the focal spot along its propagation direction with the back-focusing mirror.

This mode of operation has several uses. First, it allows for precise position of the focus at the center of the spectrometer, away from the spectrometer lens edges which may cause imaging aberrations. Next, the beam can be aligned to the split-mirror interferometer (SMI) such that the energy splitting of the two beams can be chosen. By tilting one of these half mirrors and using the spectrometer's spatial imaging mode, both beams can be observed spatially separated from each other, as observed in fig. 3.11. Proper alignment can be found by scanning the calibrated linear stage on which the second IR rejection mirror is installed and examining the changing ionization yield from each beam, as shown in fig. 3.12. Similarly,

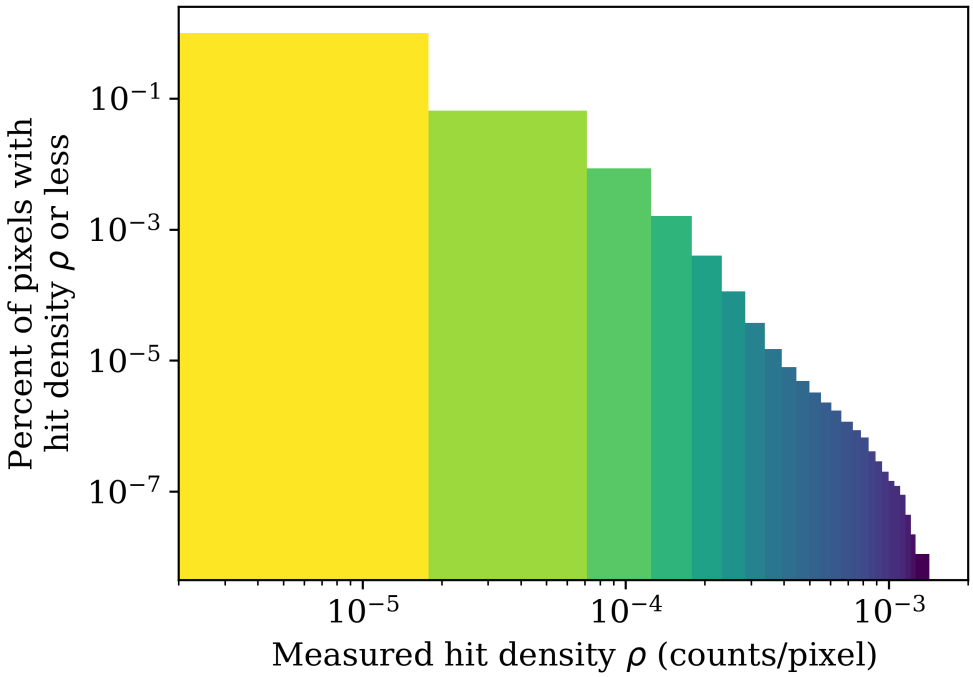

Figure 3.9: **Pixel hit density distribution.** The cumulative distribution of measured hit densities for a representative data set. A small amount of pixels have hit densities above 10^{-3} counts/pixel, where the error is on the few percent level. These pixels are localized to the center of the image, where low-energy electrons pile up.

accurate positioning of upstream D-shaped filter, such that they split the beam in the same way as the SMI, is also possible.

Spatial overlap of the pump and probe arms is also greatly aided by the spatial imaging mode. By physically overlaying the images of the foci from each beam, as seen in fig. 3.13 (a), overlap is achieved in the two dimensions of the detector.

Time Gating

By applying a pulsed voltage to the MCPs with variable onset time (with respect to the laser pulse) and width, particle detection can be limited to certain times of flight. This has been used in several ways. Dark counts from random electrical discharge or stray particles, though not a dominant source of noise, are greatly reduced by time gating the detection. Ions or electrons generated from the beam incoming to the SMI, which is positioned in between the ground and repeller plates, will have a much lower potential than those generated at the focus, and can also be fully rejected with a pulsed detection scheme.

Combined with the slight tilt of the beam from the SMI to the interaction region, the time gating allows for accurate spatial overlap in the last spatial dimension not found using

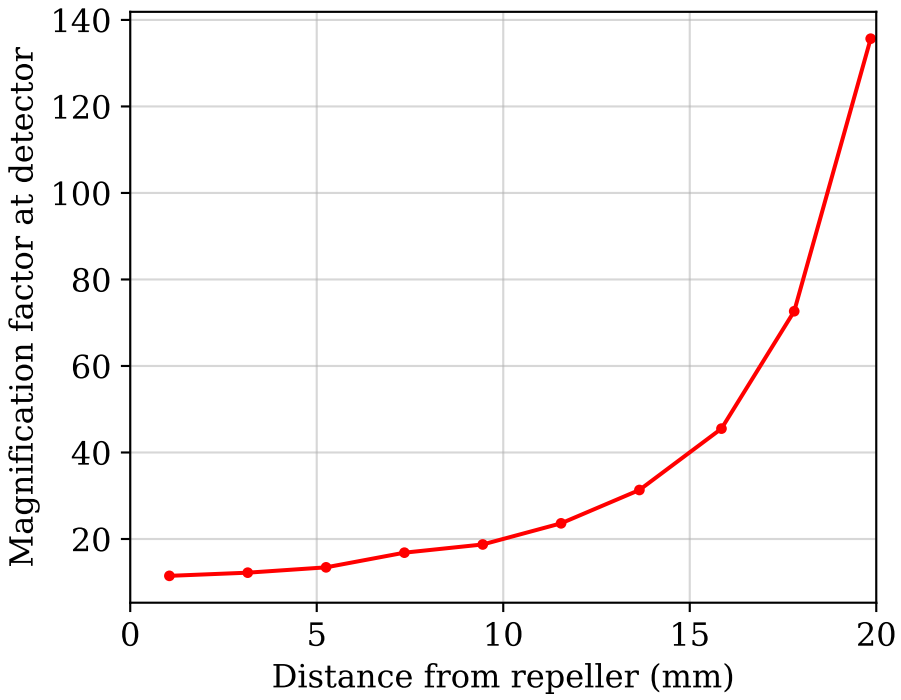

Figure 3.10: **Spatial imaging magnification factor.** The dependence on the magnification on the position of the ion source along the spectrometer axis, as calculated by SIMION simulation. Due to the upwards tilt of the beam in the spectrometer, a 500 μm long focus will lead to a 121 μm range of distances sampled and only small imaging aberrations. The focus is imaged and magnified onto the detector plane to a size of $\sim$10 mm.

the spatial imaging mode. Due to the changing height in the spectrometer along the beam propagation, particles born at different positions along this direction will have different initial potentials. This will result in a streaking of time-of-flights. By applying a short gate, a short region along the focus can be selected, as seen in fig. 3.13. Using ethylene as a target, no filters, and an SMI composed of an Aluminum coated mirror and a 157 nm coated mirror (low and high orders present from the first, 5^{th} harmonic dominating with some high orders present from the second), two foci are seen in fig. 3.13 (a) when detecting $C_2H_4^+$ and no gate is used. By applying a 50 ns gate, the signal coming from the overlap region can be selected, with all other signal being rejected, as seen in fig. 3.13 (d). To overlap the two beams along the projected spatial dimension, one beam is blocked, and the onset of this short time gate is scanned to maximize either the total signal (i.e. find the focus) or the signal integrated in a region where the two beams cross (i.e. find the overlap). Next, this first beam is blocked, with the other beam being let back in. The half-mirror of the SMI corresponding to this second beam is then scanned in the up-down direction to maximize the signal in the region

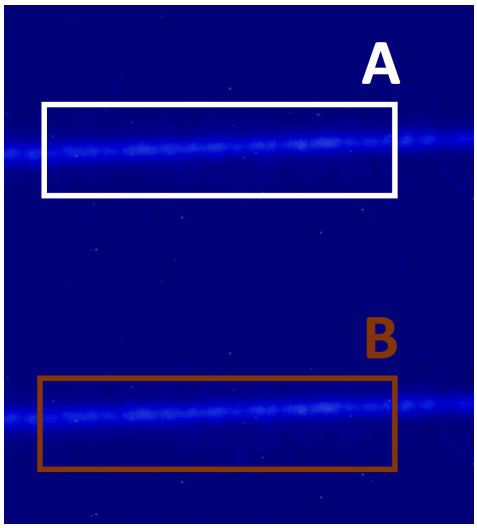

Figure 3.11: **Separation of SMI arms.** Tilting of one mirror of the SMI separates the beam such that both are visible using the spatial imaging mode. Here, lines are seen rather than foci since the ionization is due to the high order harmonics, which are able to ionize the target gas (C_2H_4) away from the focus.

where the previous signal was maximized. The two beams now cross at the same height along the spectrometer axis, and full spatial overlap is achieved.

This time gating approach can also be used to increase signal to noise ratios in these experiments [106]. Performing a pump-probe time delay scan of the two beams as before and integrating the signal measured everywhere yields the time-dependent ion yield shown in fig. 3.13 (c). The signal is normalized to the level where the pump (beam from the 157 nm half-mirror) is preceded by the probe (beam from the Aluminum coated half-mirror). Two main features are observed: (1) a short lived signal increase near the pump-probe time overlap and (2) a long term reduction in signal when the probe appears much later (Δt >100 fs) than the pump. These features and the physics of ethylene will be discussed in detail in chapter 4.

Figure 3.13(b) shows the distribution of the time-dependent hits: the average distribution of the ion signal for all pump-probe delays less than $\Delta T <$ -60 fs has been subtracted from the average distribution for delays in the range -25 fs $< \Delta T <$ 25 fs. We see that the spatial distribution of these $C_2H_4^+$ ions is localized in the overlap region. By repeating this time-delay scan using the 50 ns gate, we again observe this localized signal in fig. 3.13 (e), and also see the two time-dependent features as earlier in fig. 3.13 (f).

However, the contrast, defined as the percent increase (or decrease) of the signal relative to the background (which was defined as the signal when the probe preceded the pump), is much larger. This is due to the rejection of the signal away from the overlap which contributes a constant signal at all pump-probe time delays. While this rejection could have been simply achieved by selective integration of the spatial distribution without the short

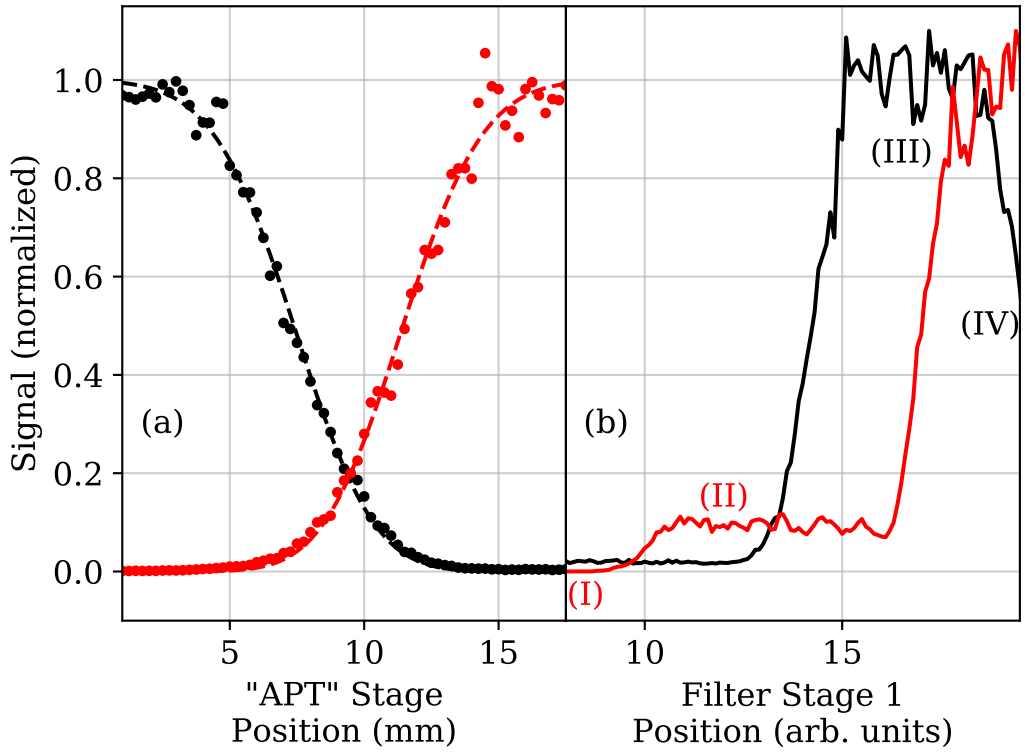

Figure 3.12: **Alignment with Spatial Imaging Mode.** Monitoring ionization yield with a harmonic source optimized for low orders allows for alignment of the beam on the SMI and of the various filters to the beam. (a) As the beam is scanned across the split-mirror interferometer, the signal coming from the Aluminum coated mirror (red) begins to dominate over that from the 157 nm coated mirror (black). At a position of ∼9.4 mm, the beam is equally split. The signals at this position in each arm are less than half of the respective maximal signals mostly due to the nonlinear dependence of the multi-photon ionization process on beam energy. (b) Four zones are observed when scanning a D-shaped 5^{th} coated MgF_2 filter (see fig. 2.12) across the beam: the beam can be blocked by either side of the filter holding assembly (I and IV), the beam can go through the D-shaped filter (II), or the beam can go through the D-shaped hole (III). The filter should be set such that the arm with which the filter is associated (red) is in zone (II) while the other arm (black) is in zone (III), corresponding here to a position of ∼15.5 mm.

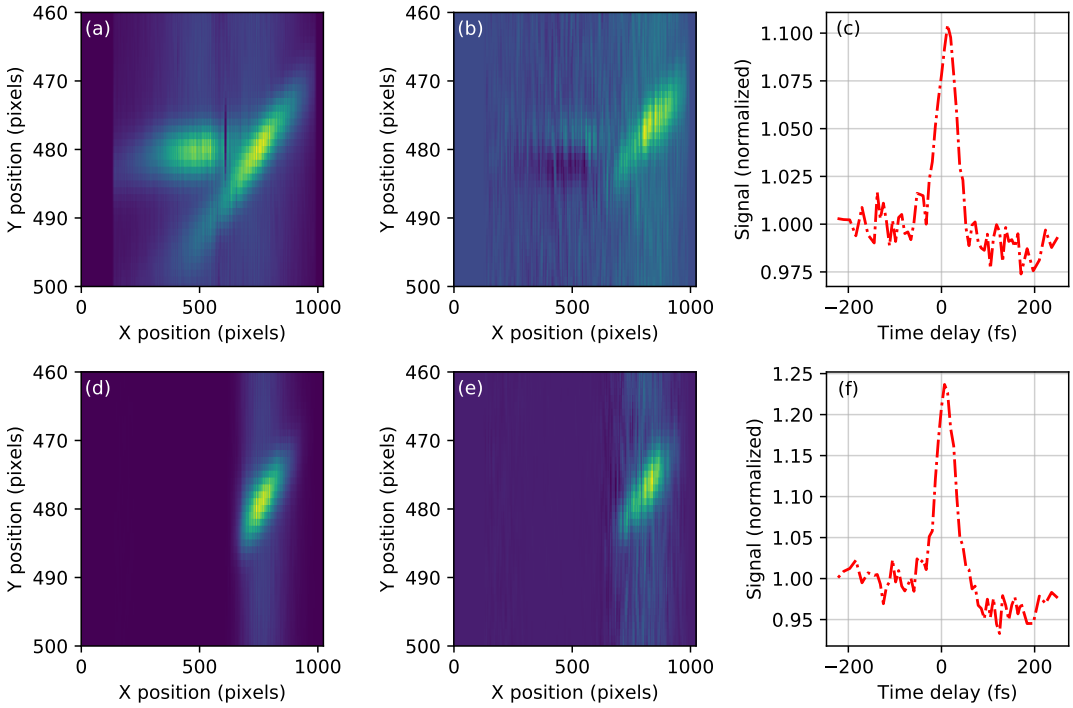

Figure 3.13: **Time gating in spatial imaging mode.** (a) Spatial distribution of $C_2H_4^+$, showing two foci from the two beams from the SMI. (b) The spatial distribution of the time-dependent signal, as defined in the text, is localized to the overlap region. (c) The time-dependent total integrated signal, showing a short-lived increase near the pump-probe overlap and a long term decrease, due to a bleach effect discussed in chapter 4. (d) Spatial distribution of $C_2H_4^+$ using a 50 ns gate, showing a localization along the beam propagation direction. (e) Time-dependent signal, as in (b), but with the 50 ns gate. (f) Time-dependent total integrated signal, as in (c), but with the 50 ns gate. Since the signal away from the overlap region is rejected, the contrast of the two time-dependent features is increased. For (a, b, d, e), we note that the aspect ratio is large, such that the beam waist size and the angle between the two beams appear larger than they are.

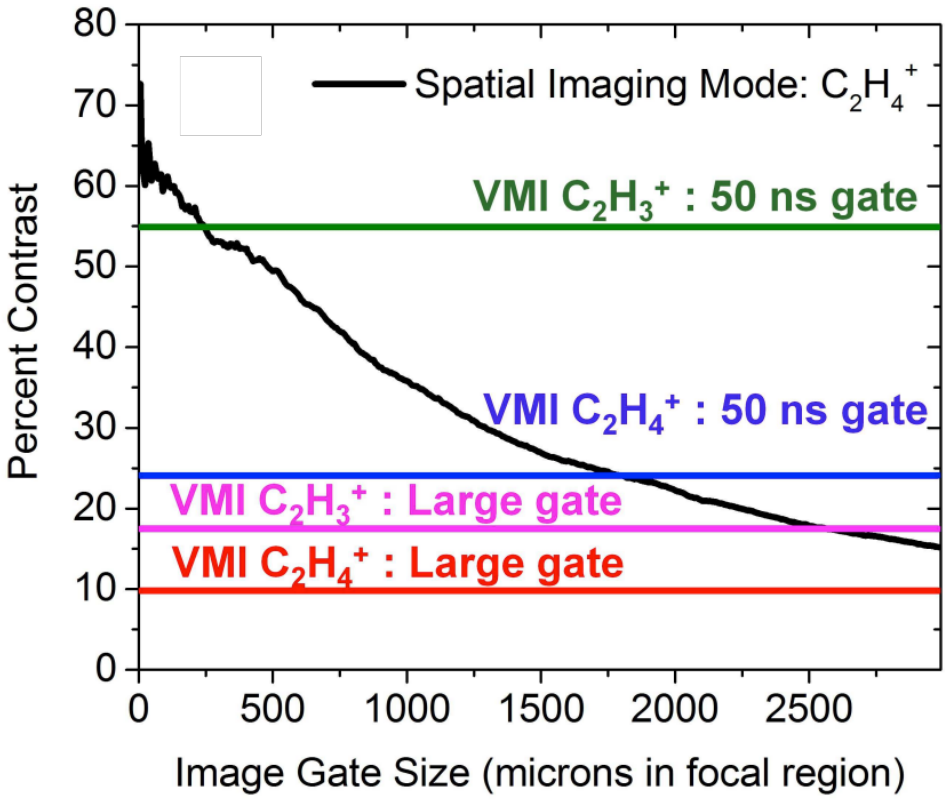

Figure 3.14: **Increased Signal-to-Noise Ratio with Time Gating.** Applying a spatial gate (selective integration) in spatial imaging mode for $C_2H_4^+$ increases the signal-to-noise ratio of a pump-probe experiment (quantified here by the percent contrast, see text). Reducing the size of this gate in spatial imaging mode leads to a monotonically increasing contrast (black), as signal generated from outside the pump-probe overlap volume is selectively decreased. The horizontal colored lines correspond to the contrast achieved using the time gating method in VMI mode. The contrasts with the 50 ns gates are larger than those using a large gate and full focal averaging. Figure adapted from [106].

time gate, this concept can be extended to VMI experiments, where the spatial separation is no longer possible [106]. Fig. 3.14 shows the dependence of the percent contrast for either $C_2H_4^+$ or $C_2H_3^+$ yield, defined as the integrated signal near the pump-probe overlap divided by the average integrated signal where the probe precedes the pump, on various experimental parameters. For the case explored above ($C_2H_4^+$ in spatial imaging mode), selective integration of the image gives contrasts that improve as the spatial gate size is reduced, as expected. A large gate size corresponding to full focal averaging gives a contrast at the ∼15% level, while a spatial gate of 250 um or below leads to contrast near 60%. From SIMION simulations, a 50 ns gate with the 14° beam tilt used here selects ions created within a 1.7 mm spatial gate. The 25% contrast observed using this gate agrees with the contrast

obtained using a spatial gate of this size.

For $C_2H_3^+$ using the VMI detection scheme, we see an even larger increase in contrast, from 17% without the time gating to 55% with it. This large increase, as compared to that for $C_2H_4^+$, is due to the larger production of the fragmented ion by the high order harmonics outside of the focal region. We note that this technique is thus far limited to ions, as the time-of-flights of the photoelectrons are much below the 50 ns gate used here.

3.2 pBASEX Abel Inversion

The Abel Transform

For a given physical process leading to the emission of charged particles, the probability distribution of these particles can be described as a function of particle kinetic energy (E) and direction, specified by the polar (θ) and azimuthal (ϕ) angles:

$$F(E,\theta,\phi), \text{ such that } \int_0^\infty \int_0^\pi \int_0^{2\pi} F(E,\theta,\phi) E^2 \sin\theta d\phi d\theta dE = N \tag{3.5}$$

Given some time of evolution t, this distribution in kinetic energy space becomes a Newton sphere which can be represented as a spatial distribution:

$$r = vt \tag{3.6a}$$
$$E = \frac{m}{2}v^2 = \alpha r^2 \tag{3.6b}$$
$$\alpha = \frac{m}{2t^2} \tag{3.6c}$$
$$\frac{dE}{dr} = 2\alpha r = 2\sqrt{\alpha E} \tag{3.6d}$$
$$f(r,\theta,\phi), \text{ such that } \int_0^\infty \int_0^\pi \int_0^{2\pi} f(r,\theta,\phi) r^2 \sin\theta d\phi d\theta dr = N \tag{3.6e}$$
$$F(E,\theta,\phi)E^2 dE = f(r,\theta,\phi) r^2 dr \tag{3.6f}$$
$$F(E,\theta,\phi) = \frac{f(r,\theta,\phi) r^2}{E^2} \left(\frac{dE}{dr}\right)^{-1} \tag{3.6g}$$
$$= \frac{f(r,\theta,\phi)}{2(\alpha E)^{3/2}} \tag{3.6h}$$

A Velocity Map Imaging (VMI) spectrometer measures the projection of this three-dimensional distribution onto a two-dimensional plane. Mathematically, this projection is known as an Abel transform.

$$\tilde{f}(y,z) = \int_{-\infty}^{+\infty} dx f(r,\theta,\phi) \tag{3.7}$$

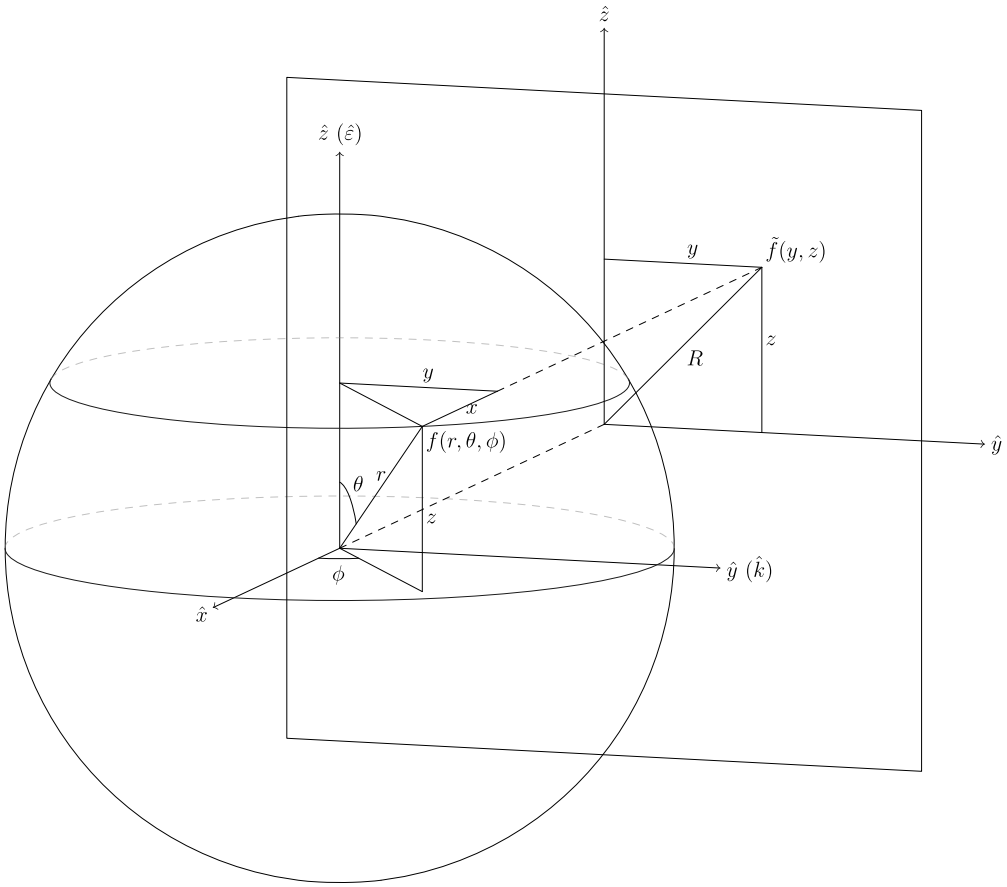

Figure 3.15: **Abel transformation: projection of the Newton sphere.** The probability density of the Newton sphere at the point $f(r, \theta, \phi)$ contributes to the measured detector signal $\tilde{f}(y, z)$.

It can be easier to picture this process in one less dimension, where a two-dimensional distribution $f(r, \theta)$ is projected onto a line where $\tilde{f}(y)$ is measured:

$$\tilde{f}(y) = \int_{-\infty}^{+\infty} f(r, \theta) dx, \tag{3.8}$$

or, given an isotropic distribution:

$$\tilde{f}(y) = 2 \int_{0}^{+\infty} f(r) dx, \tag{3.9}$$

Although I have found it advantageous to use this form of the Abel transform for the following implementation of Abel inversion, the more commonly seen form follows a radial rather than

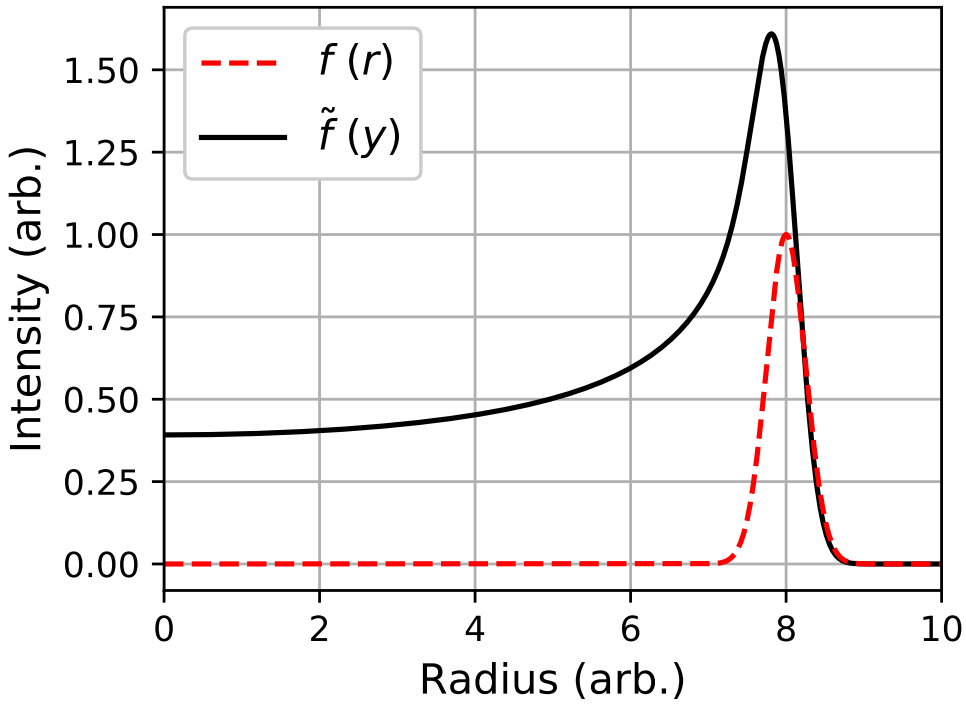

Figure 3.16: **One-dimensional Abel transform.** The Abel transform of a thin Gaussian radial, isotropic angular distribution. Due to the projected measurement, signal will appear at the center of the detector ($r = 0$).

Cartesian integration variable and a Jacobian is thus needed:

$$x = \sqrt{r^2 - y^2} \tag{3.10}$$

$$dx = \frac{rdr}{\sqrt{r^2 - y^2}} \tag{3.11}$$

$$\tilde{f}(y) = 2\int_y^{+\infty} \frac{f(r)rdr}{\sqrt{r^2 - y^2}}. \tag{3.12}$$

The Abel transform of an isotropic, thin-shelled distribution is shown in fig. 3.16. For this isotropic case, an analytic expression for the inverse transform can be found. In general, however, the reduced dimensionality of the measurement will make it impossible to recover the full three-dimensional distribution.

Axial Symmetry

For the case of photoionization of an isotropic target or an unaligned ensemble with linearly polarized light whose polarization vector lies parallel to the detection plane, axial symmetry

is achieved, and we can describe the original distribution with only two planar coordinates:

$$f(r,\theta,\phi) \Rightarrow f(r,\theta) \tag{3.13}$$

$$\tilde{f}(y,z) = 2\int_0^\infty dx f(r,\theta) \tag{3.14}$$

With this axial symmetry, no information is lost in the projection. The challenge is now to perform an inverse Abel transform and recover the original distribution from its detected projection.

Conservation of angular momentum during the light-matter interaction further simplifies the task at hand, as the original distribution can be described with a general radial part multiplied by an angular part described as a sum of the Legendre polynomials. The highest order Legendre polynomial to include will be twice the order of the light-matter interaction.

$$l_{max} = 2N_{photons} \tag{3.15}$$

$$f(r,\theta) = \frac{\sigma(r)}{4\pi}[1 + \sum_{\substack{l=2 \\ l\ even}}^{l_{max}} \beta_l(r) P_l(\cos\theta)] \tag{3.16}$$

When dealing with an anisotropic target or an aligned ensemble, this decomposition still works assuming axial symmetry still holds. However, it is no longer possible to truncate the sum of Legendre polynomials to get complete agreement. Still, partially due to the orthogonality of the Legendre polynomials, setting an arbitrary truncation can still be useful in approximating the angular distribution and extracting potentially relevant observables.

The pBASEX approach

Although it will no longer be possible to describe any arbitrary distribution, the use of radial basis functions to describe $\sigma(r)$ and $\beta_l(r)$ will allow for Abel inversion:

$$\sigma(r) \simeq \sum_k c_{k0} f_k(r) \tag{3.17}$$

$$f(r,\theta) = \frac{1}{4\pi} \sum_k c_{k0} f_k(r)[1 + \sum_{\substack{l=2 \\ l\ even}}^{l_{max}} \beta_l(r) P_l(\cos\theta)] \tag{3.18}$$

$$\beta_l(r) \simeq \frac{\sum_k c_{kl} f_k(r)}{\sum_k c_{k0} f_k(r)} \tag{3.19}$$

$$f(r,\theta) = \frac{1}{4\pi} \sum_k \sum_{\substack{l=0 \\ l\ even}}^{l_{max}} c_{kl} f_k(r) P_l(\cos\theta) \tag{3.20}$$

$$= \sum_k \sum_{\substack{l=0 \\ l\ even}}^{l_{max}} c_{kl} f_{kl}(r,\theta) \tag{3.21}$$

These basis functions can now be Abel transformed:

$$R = \sqrt{y^2 + z^2} \tag{3.22}$$

$$r = \sqrt{R^2 + x^2} \tag{3.23}$$

$$\cos\theta = \frac{z}{\sqrt{R^2 + x^2}} \tag{3.24}$$

$$\tilde{f}(y,z) = 2\int_0^\infty dx f(r,\theta) \tag{3.25}$$

$$= 2\sum_k \sum_{\substack{l=0 \\ l\ even}}^{l_{max}} c_{kl} \int_0^\infty dx f_{kl}(\sqrt{R^2 + x^2}, \cos^{-1}\frac{z}{\sqrt{R^2 + x^2}}) \tag{3.26}$$

$$= \frac{1}{2\pi} \sum_k \sum_{\substack{l=0 \\ l\ even}}^{l_{max}} c_{kl} \int_0^\infty dx f_k(\sqrt{R^2 + x^2}) P_l(\frac{z}{\sqrt{R^2 + x^2}}) \tag{3.27}$$

$$= \sum_k \sum_{\substack{l=0 \\ l\ even}}^{l_{max}} c_{kl} \tilde{f}_{kl}(y,z) \tag{3.28}$$

$$\tilde{f}_{kl}(y,z) = \frac{1}{2\pi} \int_0^\infty dx f_k(\sqrt{R^2 + x^2}) P_l(\frac{z}{\sqrt{R^2 + x^2}}) \tag{3.29}$$

In practice, the measured distribution must be represented as a discrete function, whether this discretization is explicit due to detector pixelization or achieved through binning. Due

to the finite measurement domain, the data can then be represented as a vector $\vec{b} \in \mathbb{R}^{n_p}$, where n_p is the number of pixels. In a similar way, the Abel transformed basis functions can be represented as a matrix $G \in \mathbb{R}^{n_p \times n_b}$, where n_b is the number of basis functions, and the coefficients of the basis functions as a vector $\vec{c} \in \mathbb{R}^{n_p}$. It is now possible to find the coefficients by fitting the data using:

$$G\vec{c} = \vec{b} \tag{3.30}$$

Assuming a square and euclidean pixel grid, there will be $\sqrt{n_p}$ points sampled in each axis. This number is an appropriate upper limit on the amount of radial basis functions to use to avoid overfitting on $\sigma(r)$. In most applications, the sum over Legendre polynomials will be truncated such that:

$$l_{max} \ll \sqrt{n_p} \tag{3.31a}$$

$$n_b \leq l_{max}\sqrt{n_p} \ll n_p. \tag{3.31b}$$

This leads to an underdetermined system when solving for the coefficients, which makes least squares linear regression an appropriate tool. We find the optimal coefficient vector $\vec{c}_*$ such that:

$$\vec{c}_* = \underset{\vec{c}}{\operatorname{argmin}} \|G\vec{c} - \vec{b}\|^2 \tag{3.32}$$

This problem has an analytical solution. Using the singular value decomposition of G, we can obtain the optimal coefficients and recover the original distribution:

$$G = U\Sigma V^T \tag{3.33}$$

$$\vec{c}_* = V\Sigma^{-1}U^T\vec{b} \tag{3.34}$$

$$\sigma(r) = \sum_k c_{k0} f_k(r) \tag{3.35}$$

$$\beta_l(r) = \frac{\sum_k c_{kl} f_k(r)}{\sum_k c_{k0} f_k(r)} \tag{3.36}$$

We also note that use of the singular value decomposition allows for both a regularized fit with regularization values λ_i as the diagonal elements of $\lambda \in \mathbb{R}^{n_b \times n_b}$:

$$\vec{c}_* = \underset{\vec{c}}{\operatorname{argmin}} \|G\vec{c} - \vec{b}\|^2 + \|\lambda^{1/2}\vec{c}\|^2 \tag{3.37}$$

$$= V\tilde{\Sigma}^{-1}U^T\vec{b} \tag{3.38}$$

$$\tilde{\Sigma}^{-1}_{ij} = \delta_{ij}\frac{\Sigma_{ii}}{\Sigma_{ii}^2 + \lambda_i} \tag{3.39}$$

or a weighted fit with pixel weights w_i as the diagonal elements of $W \in \mathbb{R}^{n_p \times n_p}$:

$$\vec{c}_* = \underset{\vec{c}}{\operatorname{argmin}} \|W^{1/2}(G\vec{c} - \vec{b})\|^2 \tag{3.40}$$

$$= V\Sigma^{-1}(U^TWU)^{-1}U^TW\vec{b}. \tag{3.41}$$

The particle kinetic energy spectrum and angular distribution are the two outputs. The angular distribution follows trivially from $\beta_l(r)$, while a bit more work is needed for the kinetic energy spectrum:

$$\beta_l(E) = \frac{\sum_k c_{kl} f_k(\sqrt{\frac{E}{\alpha}})}{\sum_k c_{k0} f_k(\sqrt{\frac{E}{\alpha}})} \tag{3.42}$$

$$F(E,\theta,\phi) = \frac{f(\sqrt{\frac{E}{\alpha}},\theta)}{2(\alpha E)^{3/2}} \tag{3.43}$$

$$= \frac{1}{8\pi(\alpha E)^{3/2}} \sum_k \sum_{\substack{l=0 \\ l\ even}}^{l_{max}} c_{kl} f_k(\sqrt{\frac{E}{\alpha}}) P_l(\cos\theta) \tag{3.44}$$

Working towards a more useful representation of the kinetic energy spectrum:

$$N = \int_0^\infty \int_0^\pi \int_0^{2\pi} F(E,\theta,\phi) E^2 \sin\theta d\phi d\theta dE \tag{3.45}$$

$$= \frac{1}{8\pi\alpha^{3/2}} \sum_k \sum_{\substack{l=0 \\ l\ even}}^{l_{max}} c_{kl} \int_0^\infty \int_0^\pi \int_0^{2\pi} f_k(\sqrt{\frac{E}{\alpha}}) P_l(\cos\theta) \sqrt{E} \sin\theta d\phi d\theta dE \tag{3.46}$$

$$= \frac{1}{2\alpha^{3/2}} \sum_k c_{k0} \int_0^\infty f_k(\sqrt{\frac{E}{\alpha}}) \sqrt{E} dE \tag{3.47}$$

$$= \int_0^\infty I(E) dE \tag{3.48}$$

$$I(E) = \frac{1}{2\alpha^{3/2}} \sum_k c_{k0} f_k(\sqrt{\frac{E}{\alpha}}) \sqrt{E} \tag{3.49}$$

Error propagation

For error analysis, we will propagate errors from the data $\vec{b}$ to the coefficients $\vec{c}$ and finally to the final functions $I(E)$ and $\beta_l(E)$. Making use of the error propagation formula in the linear case:

$$\vec{y} = A\vec{x} \tag{3.50}$$

$$\Sigma_y = A\Sigma_x A^T, \tag{3.51}$$

where Σ_z is the variance-covariance matrix of vector $\vec{z}$ (not to be mistaken with the Σ from the earlier single value decomposition), we find:

$$\Sigma_c = V\Sigma^{-1}U^T\Sigma_b U\Sigma^{-1}V^T. \tag{3.52}$$

We can reformulate eq. (3.49) in terms of matrix multiplications to again make use eq. (3.51):

$$I(E) = \frac{\sqrt{E}}{2\alpha^{3/2}} F\vec{c}_0 \tag{3.53}$$

$$= \frac{\sqrt{E}}{2\alpha^{3/2}} F J_0 \vec{c} \tag{3.54}$$

$$= \frac{\sqrt{E}}{2\alpha^{3/2}} \tilde{F}^0 \vec{c} \tag{3.55}$$

$$\Sigma_I = \frac{E}{4\alpha^3} \tilde{F}^0 \Sigma_c \tilde{F}^{0^T} \tag{3.56}$$

$$\tilde{F}^l = F J_l, \tag{3.57}$$

where $F \in \mathbb{R}^{n_r \times n_k}$, similarly to G, represents the sampled values of all of the radial basis functions $f_k(\sqrt{\frac{E}{\alpha}})$, and $\vec{c}_0 = J_0\vec{c}$ the coefficients of the basis functions of $l = 0$ only (which we can extend to $l \neq 0$).

For Σ_{β_l}, the situation is more difficult due to the nonlinearity. We can find the needed Jacobian $D^l = \vec{\nabla}_c \beta_l$ by again using a matrix formulation:

$$\beta_l(E) = \frac{F\vec{c}_l}{F\vec{c}_0} \tag{3.58}$$

$$= \frac{F J_l \vec{c}}{F J_0 \vec{c}} \tag{3.59}$$

$$D^l_{ik} = \frac{\partial \beta_l(E_i)}{\partial c_{kl}} \tag{3.60}$$

$$= \frac{\tilde{F}^l_{(ik)} - \tilde{F}^0_{(ik)} \beta_l(E_i)}{\sigma(\sqrt{\frac{E_i}{\alpha}})}, \tag{3.61}$$

and can find the uncertainties in $\beta_l(E)$:

$$\Sigma_{\beta_l} = D^l \Sigma_c D^{l^T}. \tag{3.62}$$

MATLAB and Python implementations of this inversion algorithm have been written and are available online [1].

Choice of basis functions

The standard choice for basis functions are Gaussian functions:

$$f_k(r) = \frac{1}{\sqrt{2\pi}\sigma_k} e^{-\frac{1}{2}(\frac{r-r_k}{\sigma_k})^2} \tag{3.63}$$

[1] https://github.com/e-champenois/CPBASEX/

Typically, these functions will be evenly spaced and have constant width:

$$r_k = r_0 + k\Delta r \tag{3.64}$$
$$\sigma_k = \sigma \tag{3.65}$$

A range of values for σ will work decently, but we can choose one that allows to generate a relatively flat function:

$$f(r) = \frac{1}{2}[f_k(r) + f_{k+1}(r)] \tag{3.66}$$
$$f(\frac{r_k + r_{k+1}}{2}) = f(r_k + \Delta r/2) = f(r_k) = f(r_{k+1}) \tag{3.67}$$
$$e^{-\frac{(\Delta r/2)^2}{2\sigma^2}} = \frac{1}{2}[1 - e^{-\frac{\Delta r^2}{2\sigma^2}}] \tag{3.68}$$
$$\sigma = (0.45291...)\Delta r \approx 0.5\Delta r \tag{3.69}$$

The integrals that need to be calculated are then of the form:

$$\tilde{f}_{kl}(x,y) = \frac{1}{(2\pi)^{3/2}\sigma}\int_0^\infty dz e^{-\frac{1}{2}(\frac{\sqrt{R^2+z^2}-r_k}{\sigma})^2} P_l(\frac{x}{\sqrt{R^2+z^2}}) \tag{3.70}$$

We can write the Legendre polynomials as a sum over monomials:

$$\tilde{f}_{kl}(x,y) = \frac{2^l}{(2\pi)^{3/2}\sigma}\sum_{n=0}^{l/2} x^{2n}\binom{l}{2n}\binom{\frac{l+2n-1}{2}}{l}\int_0^\infty dz \frac{e^{-\frac{1}{2}(\frac{\sqrt{R^2+z^2}-r_k}{\sigma})^2}}{(R^2+z^2)^n} \tag{3.71}$$
$$= \frac{2^l}{(2\pi)^{3/2}\sigma}\sum_{n=0}^{l/2} x^{2n}\binom{l}{2n}\binom{\frac{l+2n-1}{2}}{l} I_{kn}(x,y) \tag{3.72}$$

An analytic solution is possible by using a truncated Taylor expansion rather than the Gaussian radial basis function. The Taylor expansion must be truncated at an odd M for the function to have zeros. Numerical methods or lower bounds can be used to find the

domain of this new radial basis function, delimited by these zeros.

$$e^{-\frac{1}{2}(\frac{r-r_k}{\sigma})^2} \simeq \begin{cases} \sum_{m=0}^{M}(-\frac{1}{2\sigma^2})^m \frac{(r-r_k)^{2m}}{m!}, & r_k - r_M \leq r \leq r_k + r_M \\ 0, \text{ elsewhere} \end{cases} \tag{3.73}$$

$$\sum_{m=0}^{M} \frac{1}{m!}(-\frac{r_M^2}{2\sigma^2})^m = 0 \tag{3.74}$$

$$\sqrt{R^2 + z_\pm^2} = r_k \pm r_M \tag{3.75}$$

$$z_\pm = \sqrt{\max(0, (r_k \pm r_M)^2 - R^2)} \tag{3.76}$$

$$I_{kn}(x,y) = \sum_{m=0}^{M} \frac{1}{m!}(-\frac{1}{2\sigma^2})^m \int_{z_-}^{z_+} dz \frac{(\sqrt{R^2+z^2} - r_k)^{2m}}{(R^2+z^2)^n} \tag{3.77}$$

$$= \sum_{m=0}^{M}\sum_{j=0}^{2m} \frac{1}{m!}(-\frac{1}{2\sigma^2})^m \binom{2m}{j} (-r_k)^{2m-j} \int_{z_-}^{z_+} dz (R^2+z^2)^{\frac{j}{2}-n} \tag{3.78}$$

$$= \sum_{m=0}^{M} \frac{1}{m!}(-\frac{r_k}{2\sigma^2})^m \sum_{j=0}^{2m} \binom{2m}{j} (-\frac{R}{r_k})^j R^{-2n} [z_2F_1(\frac{1}{2}, n-\frac{j}{2}; \frac{3}{2}; -\frac{z^2}{R^2})]\Big|_{z_-}^{z_+} \tag{3.79}$$

There are no more numerical integrals, but samplings of the hypergeometric function are needed:

$$\tilde{f}_{kl}(x,y) = \frac{2^l}{(2\pi)^{3/2}\sigma} \sum_{n=0}^{l/2} (\frac{x}{R})^{2n} \binom{l}{2n} \binom{\frac{l+2n-1}{2}}{l} \times \tag{3.80}$$

$$\sum_{m=0}^{M} \frac{1}{m!}(-\frac{r_k}{2\sigma^2})^m \sum_{j=0}^{2m} \binom{2m}{j} (-\frac{R}{r_k})^j [{}_2F_1(\frac{1}{2}, n-\frac{j}{2}; \frac{3}{2}; -\frac{z^2}{R^2})z]\Big|_{z_-}^{z_+} \tag{3.81}$$

3.3 Calibration

Determination of the energy calibration of the spectrometer, notably of α from eq. (3.6b), can be done in several ways. Numerical simulation with SIMION and use of eq. (3.6c) is one option, but the uncertainty in the actual height of the interaction along the spectrometer axis will limit this estimate. Instead, experimental calibration using a system with a known photoelectron kinetic energy distribution given a known spectrum of ionizing radiation is preferred. For such a system, we can expect a peak in the spectrum at energy $\mathrm{KE}_{e^-} = \sum \hbar\omega$ - IP, where IP is the ionization potential of the system. If this peak is located at a pixel radius r_p, we can find the calibration using:

$$\alpha = \mathrm{KE}_{e^-}/r_p^2. \tag{3.82}$$

Ionization of a noble gas is generally preferred, as the ionization potentials are well known and the peaks will always be sharp due to the absence of vibronic states. In terms of light

source, several schemes are possible. Starting with infrared light, a strong field can cause above threshold ionization [107]. While this is a complicated mechanism, it will result in a photoelectron spectrum with many peaks, all separated by the photon energy which can be measured accurately with a simple spectrometer. The large number of peaks enables a more accurate fitting for the calibration parameter α. Due to the strong field mechanism, the ionization potential IP will be shifted by the ponderomotive energy U_p, resulting in peaks at kinetic energies $\mathrm{KE}_{e^-}^{(n)}$, which we will find at radii r_n:

$$\mathrm{KE}_{e^-}^{(n)} = (n_0 + n)\hbar\omega_0 - \mathrm{IP} - U_p \tag{3.83a}$$
$$= n\hbar\omega_0 + E_0 \tag{3.83b}$$
$$= \alpha r_n^2, \tag{3.83c}$$
$$E_0 = n_0\hbar\omega_0 - \mathrm{IP} - U_p, \tag{3.83d}$$
$$r_n = \sqrt{\frac{n\hbar\omega_0 + E_0}{\alpha}}, \tag{3.83e}$$

where n_0 is the minimum number of photons required to ionize the system and E_0 is the energy of the corresponding peak.

Using the second beamline and a 780 nm, $\sim$400 μJ, 55 fs beam, and using Krypton (IP=14 eV) as a target, we observe a typical ATI signal, shown in the left half of fig. 3.17 (a). The VMI spectrometer, mainly due to the finite radius of the MCPs, is only able to record photoelectrons with projected momenta corresponding to $\sim$12 eV. This causes some issues in the inversion process as currently implemented: projected signal from high energy photoelectrons will appear over the entire MCP, but there are no basis functions at high enough energies to account for this contribution. Still, the inversion results in n=8 clear ATI peaks, as seen in fig. 3.17 (b).

A complex angular distribution with many interference fringes is also observed, and, since the number of photons contributing to the strong-field ionization process is ill-defined, it is difficult to define an $l_{\max}$ as in eq. (3.15). We see that the fit error, shown in fig. 3.17 (c), is dominated by a contribution from $P_10(\cos\theta)$ since the inversion only considered basis functions up to $l_{\max}$=8. Using eq. (3.83e) and the radii of the observed peaks, shown in fig. 3.17 (d), we find α=4.01$\times10^{-5}$ eV/pixels^2 and E_0=0.864 eV.

We can check this calibration using a more perturbative ionization scheme, notably non-resonant three photon ionization of Xenon with 265 nm light coming from the inline frequency tripler in the second beamline. This scheme produces two ionization peaks corresponding to the spin-orbit coupling split $^2\mathrm{P}_{3/2}$ and $^2\mathrm{P}_{1/2}$ spin-orbit coupling split states of Xe^+ ($5s^25p$), with ionization potentials of 12.13 and 13.43 eV, respectively [108]. While this is much less peaks than that obtained with ATI, there are no longer issues with the inversion due to high energy electrons and high order angular structure. Also, the resulting peaks are much sharper, increasing the accuracy of the calibration. The data for this calibration are shown in fig. 3.18, and result in a calibration parameter α=3.96$\times10^{-5}$ eV/pixels^2, in good agreement with the previous measurement.

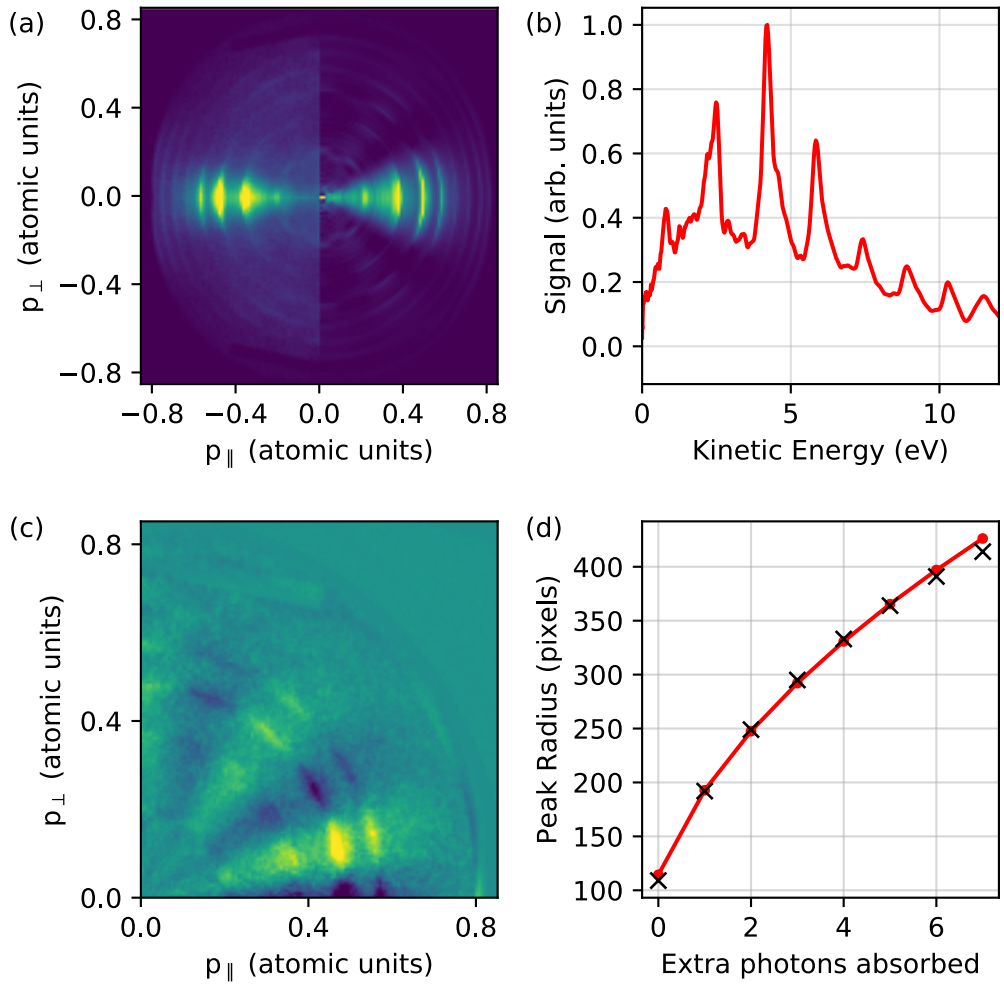

Figure 3.17: **Above Threshold Ionization of Krypton.** (a) Measured VMI data (left) and inversion (right) of the photoelectron distribution for above-threshold strong-field ionization of Krypton with the second beamline. The polarization of the light is horizontal. (b) Extracted photoelectron kinetic energy spectrum, showing 8 ATI peaks. (c) Residual of the inversion algorithm fit, showing angular structure which was lost due to the $l_{\max}$=8 cutoff of angular basis functions. (d) Peak positions (black crosses) and resultant calibration fit (red), giving the calibration parameter α=4.01×10^{-5} eV/pixels^2.

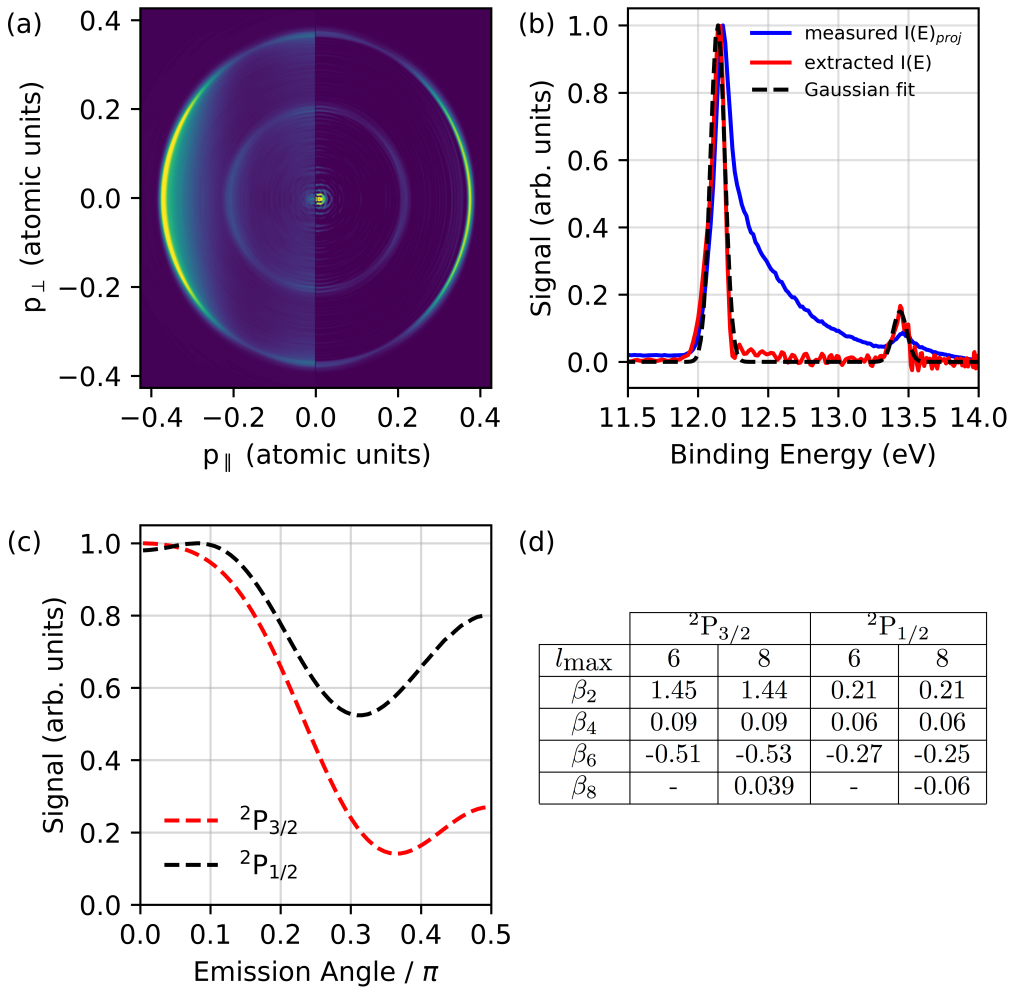

	$^2P_{3/2}$		$^2P_{1/2}$	
l_{max}	6	8	6	8
β_2	1.45	1.44	0.21	0.21
β_4	0.09	0.09	0.06	0.06
β_6	-0.51	-0.53	-0.27	-0.25
β_8	-	0.039	-	-0.06

Figure 3.18: **Xenon Ionization with Third Harmonic.** (a) Projected fit (left) and inversion (right) of the photoelectron distribution for three photon non-resonant ionization of Xenon with the third harmonic from the second beamline. The polarization of the light is horizontal. (b) The radial distribution of the measured projected data (blue), the extracted photoelectron kinetic energy spectrum (red), and Gaussian fits to the two observed ionization peaks (black, dashed). The VMI spectrometer can be calibrated energetically with the pixel radius of these peaks. (c) Angular distribution of the photoelectrons emitted for the $^2P_{3/2}$ ($\mathcal{E}$=12.13eV) and $^2P_{1/2}$ ($\mathcal{E}$=13.43eV) states. (d) Results of the fitting of the photoemission to each final state in the Legendre polynomial basis. Using even Legendre polynomials up to $l_{max}=2\times N_\gamma=6$ is enough to accurately describe the distribution.

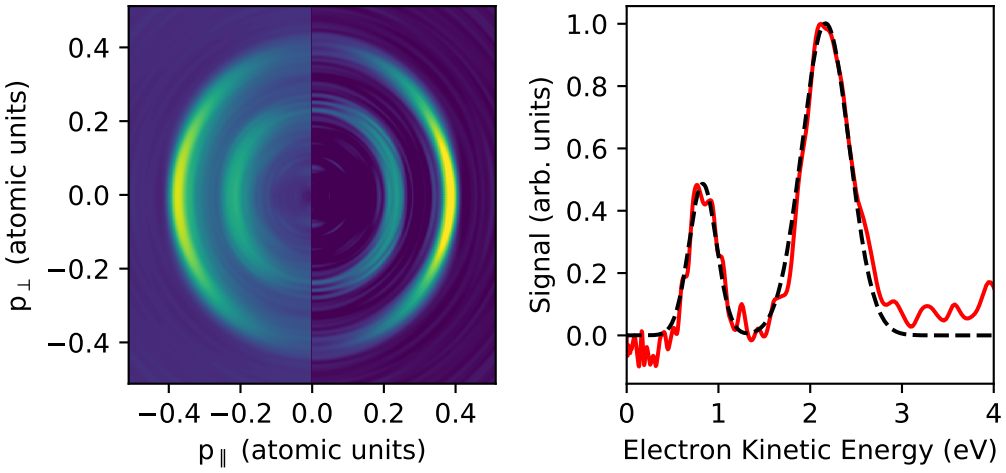

Figure 3.19: **Xenon Ionization with Ninth Harmonic.** Measured projected distribution and fitted inverted distribution (left) and spectrum (right) of photoelectrons from single photon ionization of Xenon with the ninth harmonic from the HHG source.

Also shown, in fig. 3.18 (c) are the extracted angular distributions of the photoelectrons for each final cation state. A Legendre fit up to either $l_{\max}$=6 or 8 gives similar results for β_2, β_4, and β_6, as expected from eq. (3.15). The widths of the measured peaks are 122 and 115 meV full-width-at-half-maximum for the $^2P_{3/2}$ and $^2P_{1/2}$ states, respectively. Although these widths are probably limited by the bandwidth of the light and not by the spectrometer, they set an upper bound for the spectrometer resolutions.

Single photon ionization using a high energy photon (such as a high order harmonic) is the simplest ionization scheme. However, as mentioned in fig. 2.12, the complete isolation of a single harmonic order is in general difficult. The best isolation is found by using a 100 nm Indium filter. The 9^{th} harmonic is able to efficiently ionize Xenon, resulting in two peaks as above, with the VMI images and photoelectron kinetic energy spectrum from this process shown in fig. 3.19. The resulting calibration parameter is α=4.04×10^{-5} eV/pixels^2, giving peaks at 0.8 and 2.1 eV which correspond to ionization with a $\hbar\omega_9$=14.2 eV photon ($9\hbar\omega_0$=14.3 eV).

Chapter 4

Non-Adiabatic Relaxation of Ethylene Following $\pi \rightarrow \pi^*$ Excitation

4.1 Introduction

The conversion of electronic photo-excitation energy into molecular vibrations or directed motion helps drive photochemical reactions, making it a fundamental process. Ultrafast non-adiabatic dynamics involving conical intersections have emerged as a dominant pathway for what has been argued as a majority of molecular systems[24]. While these singularities were initially considered theoretical curiosities[109], advances in the last few decades have established their important and widespread role in nature. Theoretically, progress in the computation of the potential energy surfaces of electronically excited states and in the approximate dynamical simulation of the system, including electronic surface hopping, following excitation has helped to reveal the reaction pathways for relaxation, dissociation, or isomerization in many systems. The validation of some of these theoretical methods has been possible experimentally with the possibility to follow these dynamics in real time using femtosecond laser technology.

Still, our understanding of ultrafast molecular dynamics is restricted due to limitations on both of these fronts. Experimentally, the main issues come down to the probing step: an ideal probe would allow for the measurement of both the electronic and nuclear wavefunction, but current available probing schemes fall short of this to varying degrees. On the theoretical side, the most precise methods are generally limited to molecules with just a few atoms due to the unfavorable computational scaling. Progress on both of these fronts is best tested through studying of model systems.

Ethylene is one such system, with studies involving its excited states dating back to over half a century ago[110, 111]. In its ground state, ethylene comprises nature's simplest carbon double bond and a textbook example of sp^2 hybridization[7], as seen in fig. 4.1. These traits appear in a slew of import complex systems found in both biological and industrial systems built from hydrocarbon chains or rings. In this regard, understanding of dynamics

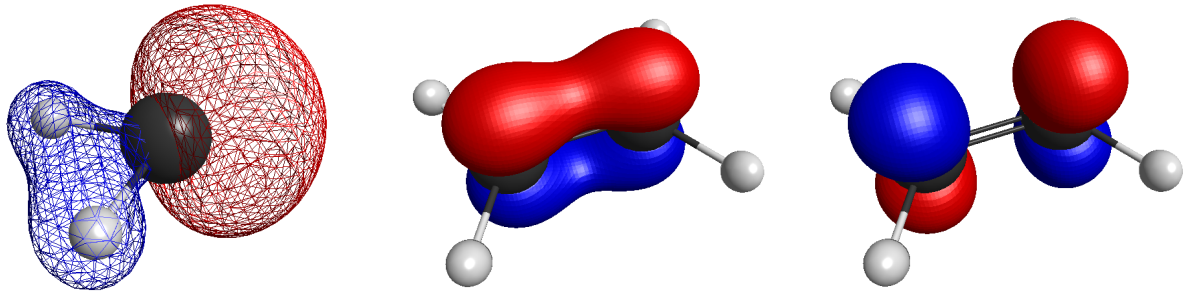

(a) (b) (c)

Figure 4.1: **Carbon Double Bond in Ethylene.** (a) The one $2s$ and two of the three $2p$ valence electron orbitals of carbon mix to create a hybridized sp^2 orbital in CH_2. These orbitals on each side of ethylene join to create a σ bond. The remaining out of plane $2p$ orbitals add in (b) or out (c) of phase to create the π (bonding) and π^* (anti-bonding) orbitals, respectively. These orbitals were calculated for CH_2 and C_2H_4 in their equilibrium geometries using the restricted Hartree-Fock method implemented in the GAMESS software[17].

in ethylene should lead to apprehension of mechanisms in hydrocarbons in general.

Ethylene's carbon double bond stiffens the molecule, keeping it rigid in a plane, in contrast to ethane (C_2H_6), which is much more free to spin about its carbon-carbon (C–C) bond due to the lack of π bonding orbital. Removal of one or both of the electrons filling this π orbital via promotion to the π^* orbital eliminates this planar rigidity. Due in large part to these properties, ethylene finds use in a large variety of processes both in nature[112] and industrially, where its production is greater than that of any other organic compound[113]. Beyond this, there has also been interest in studying the excited state dynamics of ethylene as a prototypical example of similar dynamics in more complex systems. In particular, $\pi \rightarrow \pi^*$ transitions in systems ranging from polyethylene chains to the famous retinal rhodopsin[6] also initially lead to torsion about a C–C bond due to the reduced bonding order and subsequently to rich isomerization and/or dissociation dynamics. More generally, ethylene has been an attractive candidate for learning about non-adiabatic excited state dynamics both experimentally and theoretically, as it seems to lie in some optimum between feasibility (not too large) and allure (rich dynamics, not too small).

Early experiments[114, 115, 116, 117, 118, 119, 120] were able to measure the photofragments and their relative yields following excitation, finding several decomposition channels, notably:

$$C_2H_4 \rightarrow C_2H_2 + 2H \tag{4.1}$$
$$\rightarrow C_2H_2 + H_2 \tag{4.2}$$
$$\rightarrow C_2H_3 + H \tag{4.3}$$

Both the atomic and molecular hydrogen elimination channels seemed to contribute mostly equally, as did the channels leading to acetylene (HCCH) and vinylidne (CCH_2). Further-

more, hydrogen migration across the C–C bond was found to play a role in the production of both the vinyl radical (C_2H_3) and molecular hydrogen. The studies of Y. T. Lee and coworkers helped push the understanding of ethylene's photolysis by measuring the final kinetic energies of the photofragments[121, 122] and also giving a detailed description of deuteration effects[123, 124]. Combined with theoretical calculations on the dissociation kinetics[125, 126, 127], a mostly complete picture of the photolysis of ethylene was constructed, with all of the dissociation pathways requiring the molecule to start on the ground electronic state and with a large amount of internal energy. Radiative decay from the initially excited $\pi \rightarrow \pi^*$ would remove the deposited electronic energy rather than convert it to vibrational energy, and thus an internal conversion mechanism was found to be necessary.

Subsequent studies[128, 25, 129, 130, 131] applied novel techniques including conical intersection localization and non-adiabatic dynamical simulation to ethylene, and constructed an electronic relaxation mechanism involving two conical intersections. The first occurs at a geometry where the molecule has twisted about its C–C bond (as mentioned above) and also undergone some pyradimilization, as seen in calculations of Ben-Nun et al. [128], shown in fig. 4.2. The second occurs near an ethylidene (CH_3CH) configuration, where one of the hydrogens has migrated across the molecule. The calculations predicted short lifetimes for the initially excited $\pi\pi^*$ state on the order of 100 fs.

Alongside these calculations came several experimental efforts to measure signatures of these non-adiabatic dynamics directly in the time domain [132, 133, 134]. These experiments measured the time-dependent photoionization ion yield following excitation to the $\pi\pi^*$ state using UV probe light. Despite a rather poor time resolution due to pulse durations in the hundreds of femtoseconds, these experiments were able to extract short times for the decay of their signal on the order of 20-40 fs. They attributed this timescale to the relaxation of the electronic excitation, in discrepancy with the theoretical predictions. The validity of this assignment, however, is complicated by what the "window effect" for excited state photoionization [130, 135]. While the loss of measured signal in such perturbative photoionization experiments can potentially be attributed to a change in electronic character and a subsequent loss in photoionization cross-section, an increase in the binding energy of the system's most valence electron, leading to energetically forbidden ionization, due to a separation of the potential energy surfaces of the excited state and the cation along the reaction coordinate is also possible.

Further experiments attempted to overcome this issue, using either a strong infrared field and multiphoton ionization [136, 137] or continuing with a perturbative probe at a higher energy of 7.7 eV [135]. Again, similar time scales were measured for the decay of the $C_2H_4^+$ signal in both cases. These experiments gained access to an additional channel, notably dissociative ionization to $C_2H_3^+$+H was possible. This channel was also found to decay on the 20-40 fs timescale, but appeared with a slight time delay of $\sim$10 fs.

Both of these probe schemes were subject to another detection windowing effect. Although ionization was still allowed energetically in either the infrared or VUV probe schemes, its cross-section is also largely dependent on nuclear geometry, and thus a decay in signal can be misinterpreted as electronic relaxation rather than only nuclear motion towards a conical

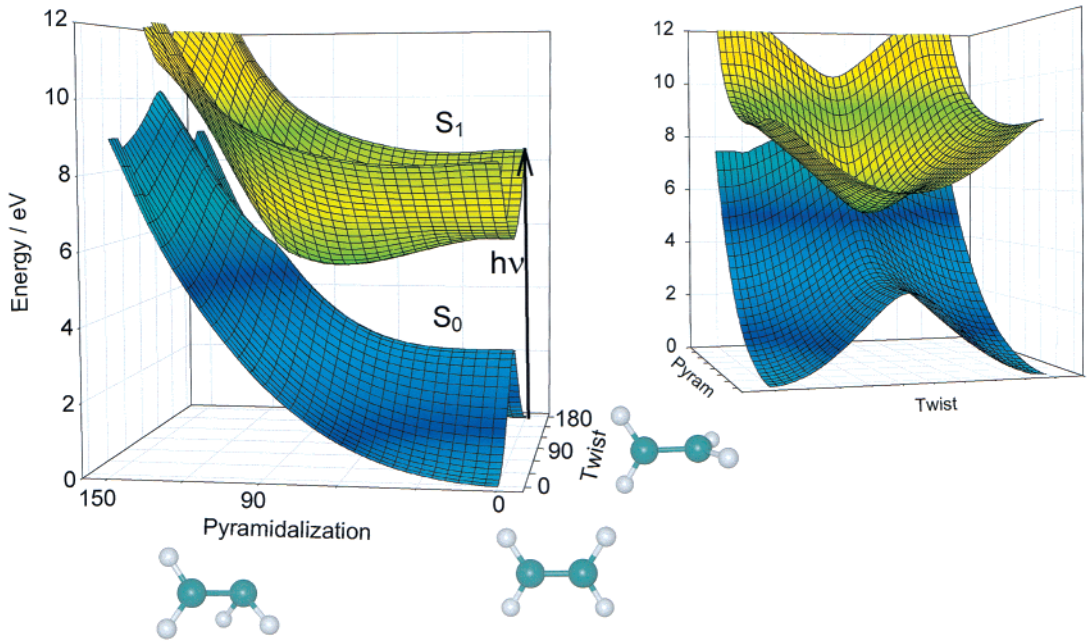

Figure 4.2: **Twist-Pyramidalization Conical Intersection.** Theoretical potential energy surfaces of ethylene adapted from [128]. Photoexcitation denoted by the black arrow initiates wavepacket dynamics on the upper electronic state. The molecule will quickly move along the twist coordinate. Subsequent motion along the pyramidalization coordinate will lead to the conical intersection with the ground state, converting the excess electronic energy of the excited state into vibrational energy on the ground state.

intersection. The multiphoton ionization scheme also suffers from its reliance on a strong field. This field can dress states via AC stark shifts [138] and even couple different states, altering the dynamics initiated by the perturbative pump before the ejection of the electron. Also, comparison with theory is difficult as modeling the interaction of this strong field with the molecule is difficult: besides wavepacket and non-adiabatic dynamics, the strong field interaction must also be simulated.

4.2 XUV probe experiments

To remedy the disagreement between these experiments and the theoretical predictions, our group (prior to my joining) conducted an experiment using an HHG source, extending their probe energy into the XUV, using the 11^{th}, 13^{th} and 15^{th} harmonics between 17 and 23 eV [88]. This high energy ionization scheme provided three main advantages. First, the photoreaction can be followed from the initial excitation all the way to the final relaxation to the ground electronic state: since the XUV probe is able to ionize the fully relaxed ground state as well as dissociated atomic and molecular hydrogen, there is no "ionization

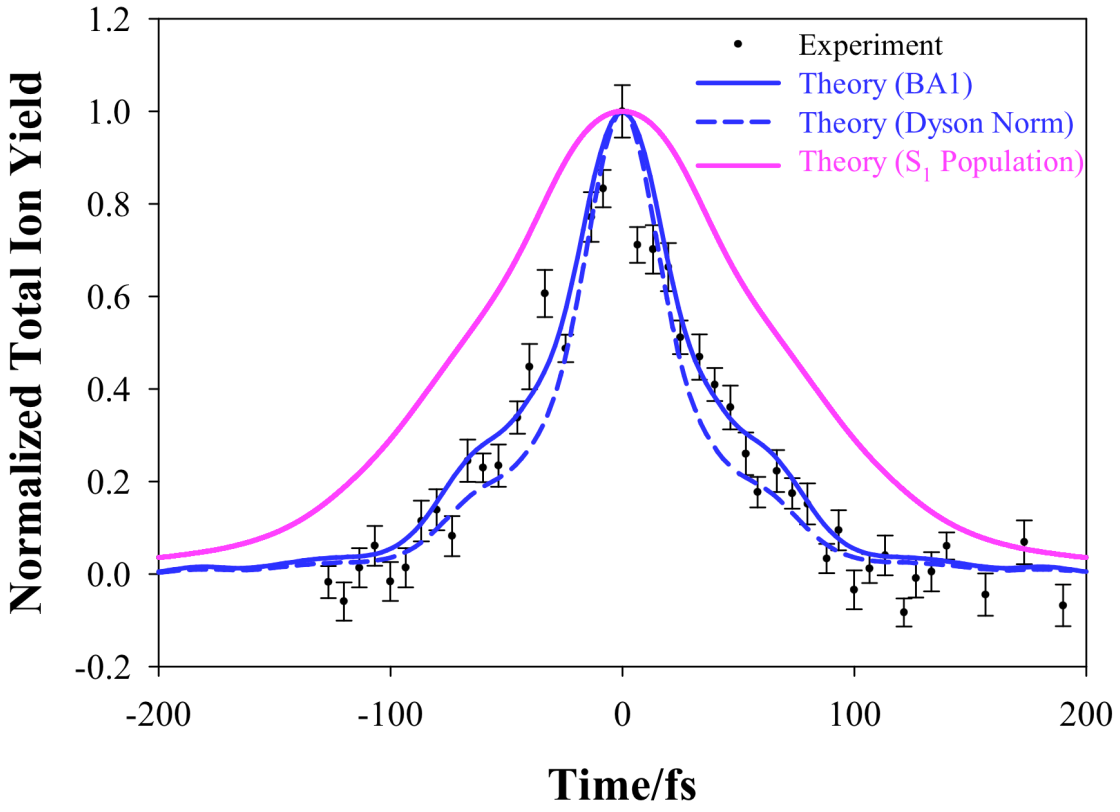

Figure 4.3: **Detection window effect in ethylene.** The experimental ion yield with a VUV probe (black) matches the predicted yield with various ionization models (blue), but greatly underestimates the predicted $\pi\pi^*$ state lifetime (pink). Figure adapted from [135].

window" effect. Next, the time-dependent ion yield measurement becomes more differential and thus potentially more informative as several new cationic dissociative limits become energetically allowed. Notably, at these high probe energies, the carbon to carbon (C–C) bond can be broken in the cation resulting in the observation of CH^+, CH_2^+, or CH_3^+. Production of these various cation products should be correlated with the instantaneous internal state of the neutral excited, dissociating molecule. For example, although cation dynamics may complicate the situation, the observation of CH_3^+ should be associated with hydrogen migration in the neutral. The available ionic fragmentation channels along with their thermodynamic limits are listed in table 4.1.

Finally, the one-photon probe scheme can be viewed as perturbative. This rules out any possibility that the probe pulse is affecting the measured dynamics, as could be the case for a strong-field IR probe. Also, theoretical simulation of the ionization step becomes much simpler and more accurate. Since comparison and eventual agreement between experiment and theory is one of the drivers for these studies, this is beneficial as it helps solve the problem of mapping the measurement (charged particles) to a detailed description of the

Table 4.1: **Ionic dissociation energies of ethylene.**, The dissociation channels and their appearance energies (relative to the ground state of the neutral molecule) for the ethylene cation are listed, with values from [139, 140, 141].

Ionic Fragment	Associated Product(s)	Thermodynamic Limit (eV)
$C_2H_4^+$	-	10.5
$C_2H_3^+$	H	13.3
$C_2H_2^+$	H_2, H+H	13.1, 17.7
CH_3^+	CH	16.9
CH_2^+	CH_2, CH+H	18.9, 22.3
CH^+	CH_3^+, CH_2+H	17.7, 22.5
H_2^+	C_2H_2	17.2
H^+	C_2H_3, C_2H_2+H	18.4, 19.9

state of the system.

The experiment observed transient signals of CH_3^+ and CH_2^+, delayed from the parent ion signal. These fragments and that of the parent ion decayed on a 100-200 fs timescale, in better agreement with the theoretical predictions. The CH_3^+ fragment appears at the latest time delays, indicating a hydrogen migration channel towards an ethylidene structure (CH_3CH). Atomic and molecular hydrogen ions were also measured, increasing in signal with ∼100 and ∼200 fs timescales, respectively. Measurement of these charged fragments was attributed to their formation in the neutral, especially since their signal does not decay at long time delays.

Beyond simulating the neutral excited state dynamics, the calculations also simulated the ionization step as well as simple cation dynamics that could lead to C–C bond breaking on the cation potential energy surfaces. These simulations found good agreement with the measurements and confirmed that the previous experiments had measured artificially shortened lifetimes for the $\pi\pi^*$ state.

4.3 Further evidence for cation C–C breakup

Using our VMI spectrometer discussed in chapter 3 and our HHG setup optimized for harmonic 15, we are able to repeat this experiment with a slightly more descriptive measurable. Instead of simply measuring ion yield, we can also resolve the kinetic energy release of the ionic fragmentation. Here, we look at the CH_2^++CH_2 channel. Since the high order harmonics are able to create CH_2^+ fragments without the presence of a pump photon, there is a bleach effect that must be separated from the excited state dynamics. This additional signal is taken into account using the same method from [88], although this more differential measurement requires subtraction of the full probe-early spectra rather than just a constant signal.

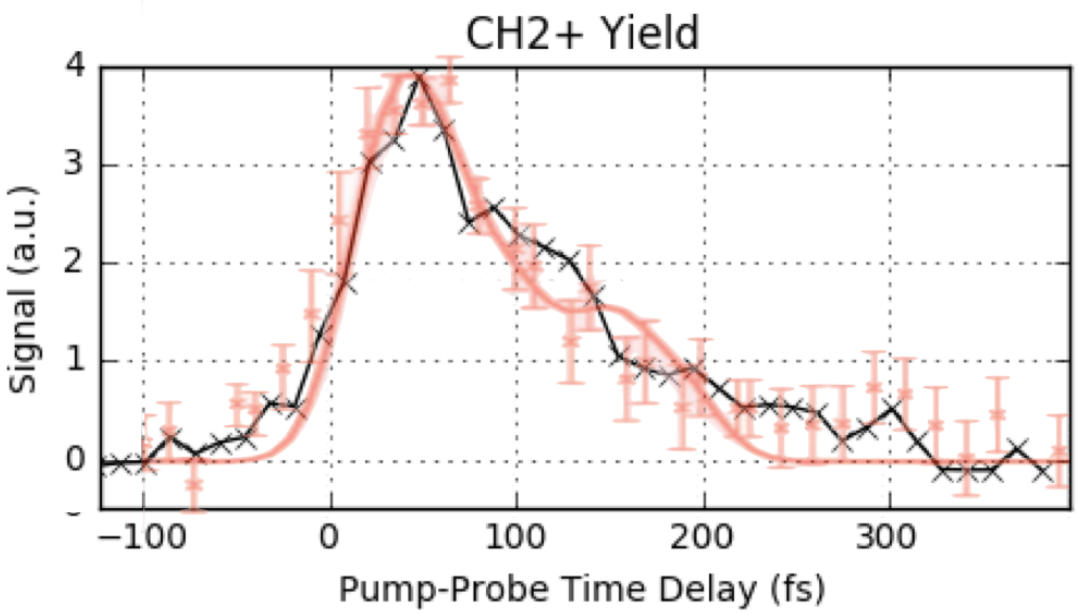

Figure 4.4: **CH_2^+ time-dependent ion yield.** Comparison of the measured VUV/XUV CH_2^+ time-dependent yield (black) with that of [88] (red ticks) and the AIMS theoretical predictions (red line).

The projection of the resulting spectra along the kinetic energy release is shown in fig. 4.4 in black, alongside the corresponding ion yield from the previous measurement shown in red. Qualitative agreement is achieved, with the a similarly delayed maximum followed by a slow decay giving a lifetime more coincident with that of the $\pi\pi^*$ state than the strong-field or UV probe measurements.

The full spectra are shown in fig. 4.5. Two different fragmentation channels are observed, corresponding to ionization to two different dissociative cation states. At the ground state equilibrium geometry and with a single photon, ionization to the C and D states of ethylene's cation leads to the population of vibrational states between 15.5 and 17 eV and 18.5 and 20 eV, respectively [142]. The cation asymptote for C–C bond break lies at ∼16 eV [143]. At small pump-probe delays, the peaks situated near 1 eV and 3.5 eV thus match what could be expected from these two states. The C state dissociation channels remains mostly at the same energy as the pump-probe time delay is increased. In contrast, the D state peak shifts to lower energies as a result of the neutral excited state dynamics discussed in [88]. These measurements bring further evidence to the theoretical analysis introduced above, which also predict predominant ionization to the C and D states [88].

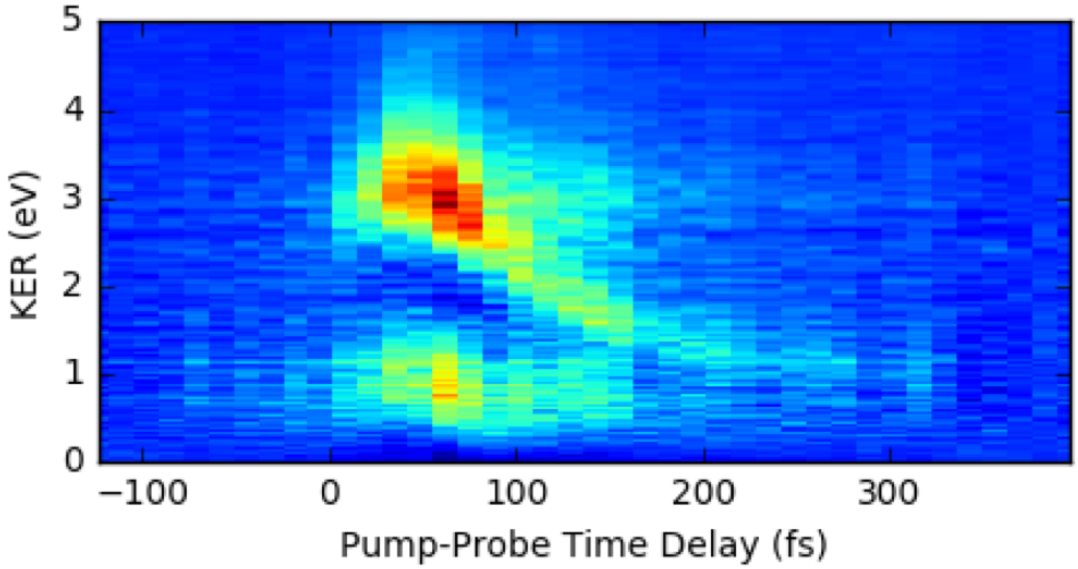

Figure 4.5: **CH_2^+ kinetic energy release spectra.** Kinetic energy release spectra of the CH_2^++CH_2 channel as a function of pump-probe delay. The 5^{th} harmonic at 7.95 eV serves as a pump, while the harmonic comb, notably the 13^{th} through 17^{th} harmonic, probe the evolving system, breaking the C–C bond.

4.4 Rydberg state

The conclusion of the combined theoretical and experimental study presented above was the identification of these two dominant relaxation pathways involving two conical intersections between the initially excited $\pi\pi^*$ state and the ground state and the observation of this electronic relaxation as well as of the ensuing atomic and molecular hydrogen dissociation channels in the time domain. However, the non-adiabatic dynamics calculations involved did not consider several excited states neighboring the $\pi\pi^*$ state energetically. Some of these are directly seen in the absorption spectrum of ethylene around 8 eV, where a broad feature associated to this short-lived $\pi\pi^*$ state is superimposed by a series of sharp absorption peaks. This spectrum adapted from [144] is shown in fig. 4.6. Spectral calculations have predicted that states corresponding to electronic excitations from the π to the empty and delocalized $3s$ and $3p_{x,y,z}$ orbitals should have energies in this region.

These molecular Rydberg states, in part due to their proximity to the $\pi\pi^*$ state, have also been a source of debate over the past several decades, in terms of their assignment and interactions with neighboring states as well as their role in photo-dynamics [145, 146, 35]. Expanding on the latter, the effect of such low-lying Rydberg states on the photo-dynamics of valence excited states has been an area of growing interest, again allowing for the use of ethylene as a base or model system.

Making use of the differing symmetries of the $\pi\pi^*$, π3s, and $\pi 3p_{x,y,z}$ states, magnetic circular dichroism measurements, two and three photon absorption studies, and resonance

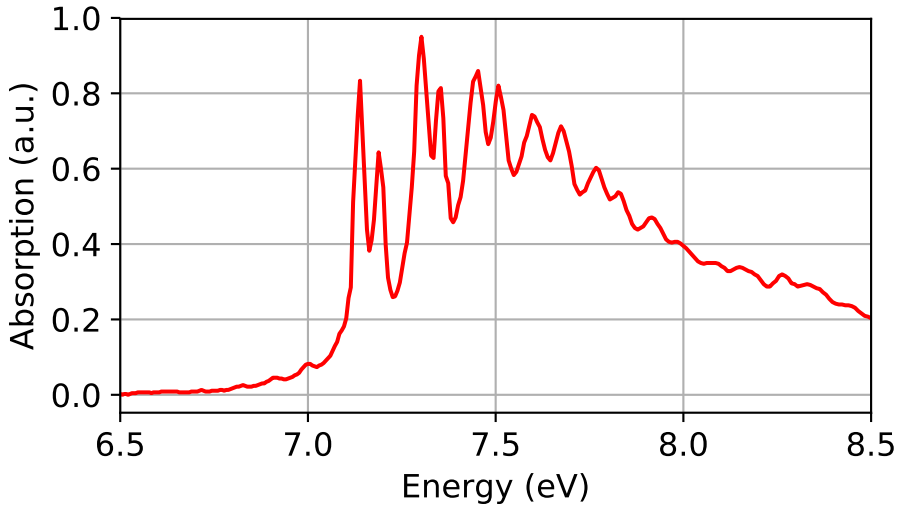

Figure 4.6: **Ethylene VUV absorption spectrum.** Ethylene's broad $\pi\pi^*$ absorption around 7 eV, with peaks arising from low-lying Rydberg states super-imposed. Data adapted from [144].

enhanced multiphoton ionization (REMPI) experiments, where one or more additional photons ionizes the resonantly populated intermediate state, have helped locate these Rydberg states in the FC region energetically[147, 148]. Though there are still various discrepancies between the many different experiments, the origins of the $\pi 3s$ and $\pi 3p$ states polarized in the y, z, and x directions were found to lie around 7.11 eV, 7.80 eV, 7.84 eV, and 8.20 eV, respectively. Strong vibronic progressions involving C–C bond stretching (ν_2) and torsion (ν_4) were also found for all of these states, with similar frequencies in each case. These vibrational frequencies are also similar to that of the ground state of the cation[144].

Although inspection of the excited orbital should be sufficient, another suitable definition of a molecular Rydberg state might be that this state has a PES that roughly parallels that of the cation, which would lead to these similar vibrational spectra. Since Rydberg orbitals are diffuse, there should be reduced correlation between an electron occupying one of them and the rest of the system's electrons. The resulting excited state PES should thus look similar to that belonging to the state in which the electron was fully removed instead of excited, corresponding to the ground state of the cation. PES calculations on these states does in fact show that they track each other and the $\tilde{X}^+$ state [149, 150].

The valence $\pi\pi^*$ state PES, however, has a different shape, leading to energy crossings in the adiabatic picture. Going back to the ultrafast relaxation of the photo-excited $\pi\pi^*$ state, the treatment of these Rydberg states as spectators to the dynamics was motivated by two factors[150, 151]. First, again due to the diffuse nature of the Rydberg orbitals, the coupling between the states may be weak. Second, the accurate inclusion of these states

in the dynamical calculations is difficult since, among other reasons, finding their electronic wavefunction accurately adds computational complexity by necessitating additional diffuse basis functions. Since these calculations were able to find agreement with the detailed experiments of [88], indicating that these assumptions may have been well founded. However, the other possibility was that probing the dynamics of the system through measuring the time-dependent ionic fragment yield following XUV ionization was not sensitive to the participation of these low-lying Rydberg states, just as probing through strong-field ionization was not sensitive to the depopulation of the $\pi\pi^*$ state.

To address this issue, the Martinez group revisited their dynamical simulations while including the $\pi 3s$ Rydberg state[150]. Energetically, they again found accessible crossings between the $\pi\pi^*$ and $\pi 3s$ states along both the C–C stretch and torsion coordinates. Dynamically, they predicted that upwards of 25% of the excitation is non-adiabatically coupled onto the Rydberg state within the first tens of femtoseconds, although this population is short-lived, with most of it coupling back onto the $\pi\pi^*$ and ground electronic states within 60 fs. While on this excited state surface, the molecule kept its rotational motion about the torsion coordinate, but pyramidalization was hampered. Several subsequent studies of these dynamics have drawn similar conclusions, indicating that the $\pi 3s$ does in fact participate in the non-adiabatic relaxation of the $\pi\pi^*$ state in ethylene [151]. Beyond the neutral excited state dynamics, Mori et al. also simulated the time-dependent ion signal expected from ionizing their time-evolving system with a second VUV photon and looked for differences depending on whether or not they the Rydberg state was included in the simulation. They found that the effects of this transient population of the Rydberg state on the ion-signal were small (see fig. 4.3), indicating that the previous description of ethylene's relaxation was still mostly accurate, though missing a small piece.

4.5 Observation of the π3s Rydberg state.

To confirm these predictions, experimental observation of the population of the $\pi 3s$ state following $\pi\pi^*$ excitation is needed. As shown above, measuring time-dependent ion yields with either strong-field or perturbative ionization, while sensitive to the part of the relaxation dynamics, is not a good probe of the system's electronic state. Time-resolved photoelectron spectroscopy, in contrast, has the ability to probe the excitation with electronic state specificity. Beyond the excited wavefunction's evolution using their AIMS method, Mori et al. also attempted to simulate a time-resolved photoelectron spectrum in order to see if this was the case for ethylene[150] Their method closely follows the ionization calculations they used to simulate time-dependent ion yields with several simplifying assumptions made. Most importantly, they assume that ionization is purely vertical[45], leaving the vibrational state of the molecule intact. With this assumption, ionization of a molecule in a given molecular geometry will result in a photoelectron with a distinct kinetic energy, given by the energy of the probe photon(s) minus the difference between the final cationic state and the populated neutral excited state at that geometry, as described in section 1.4.

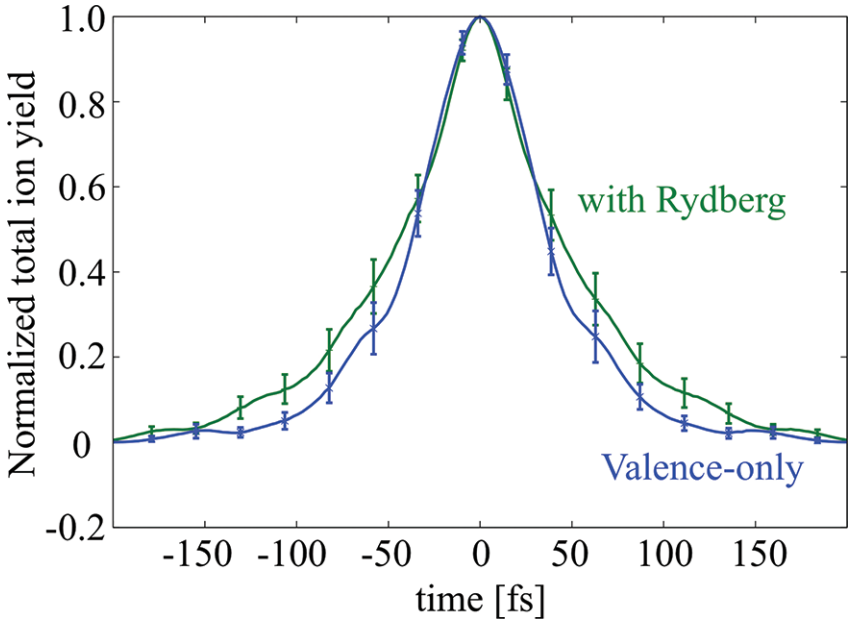

Figure 4.7: **Effect of π3s state on Ion Yield.** The inclusion of the π3s state has a mostly negligible effect on the measured ion yield. The detection window is increased by a small amount, as the population in this Rydberg state does not directly couple to the ground state, but coupling back to the $\pi\pi^*$ state is fast. Figure adapted from [150].

In their theoretical study, Mori et al. simulate their time-delayed ionization using 7.0 eV photons. Using our high harmonic beamline and VMI spectrometer, we measured the TRPES following $\pi\pi^*$ excitation using the third harmonic at 260 nm as the probe. A schematic of our experimental scheme is shown in fig. 4.8. This energy is lower than that used in the theory, but has several advantages. Notably, the combined energy of the pump and probe photons of 12.72 eV lies just barely above the first excited state of the cation, such that the majority of the measured spectrum will result from ionization to the ground state of the continuum alone. Second, this photon energy provides an advantage due to its efficient ionization of the Rydberg state. With the help of Dr. Thomas Rescigno at Lawrence Berkeley National Laboratory, we have performed calculations of the photoionization cross-section of both the $\pi\pi^*$ and π3s states at planar and twisted (15° and 30°) geometries as a function of the probe photon energy. An SCF calculation [11, 12, 13] was performed on the ground state, followed by an all singles CI calculation [14] to obtain 10 molecular orbitals (7 core orbitals and π, σ^*, and π^* orbitals associated with the ground state, Rydberg state, and $\pi\pi^*$ state, respectively) from which the target states are constructed. For the final states corresponding to an ion and a photoelectron, three ion states, corresponding to $\pi\pi^{-1}$, $\sigma^*\pi^{-2}$, and $\pi^*\pi^{-2}$, each coupled to an unbound electron, were constructed. A three-state close-coupling calculation using the complex Kohn method [152] was then performed, and the polarization dependent cross-sections were obtained from the dipole matrix elements between the initial neutral states

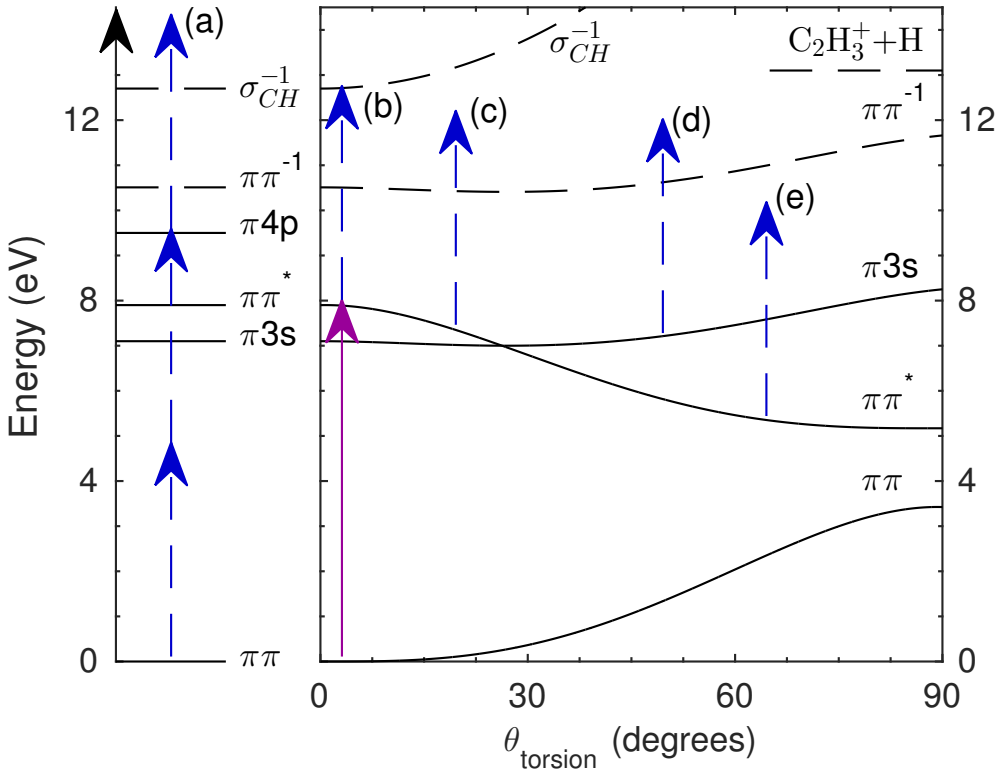

Figure 4.8: **Rydberg state detection scheme.** While (a) direct three-photon ionization at 260 nm leads to constant energy photoelectrons at the expected binding energies of the $\pi\pi^-1$ (X) or σ^-1_{CH} (A) states of the cation, the excited system can be ionized (b) directly after excitation, (c) after some torsion, or (d) after internal conversion to the π3s state, leading to a broad photoelectron spectra. (e) The detection window effect is also seen at 260 nm. Figure adapted from [51].

and the final continuum states. Since the $\pi \rightarrow \pi^*$ transition occurs only with light polarized along the C–C bond, we can expect the excited molecules to be aligned with respect to the polarization direction with a $\cos^2(\theta)$ distribution, and find the photoionization cross-section for a given state and a given geometry to go as:

$$\sigma = \frac{\sigma_x + \sigma_y + 3\sigma_z}{5}, \tag{4.4}$$

where $\hat{z}$ points along the C–C bond. A single energy shift was applied to match the calculated state energies to the measured values [147, 148]. As seen in fig. 4.9, we observe a large absolute photoionization cross-section of the Rydberg state and also a high ratio of the π3s to $\pi\pi^*$ cross-sections at $\hbar\omega_3$=4.77 eV. Both of these make detection of any population of the π3s state more probable, and could explain differences in these experimental measurements

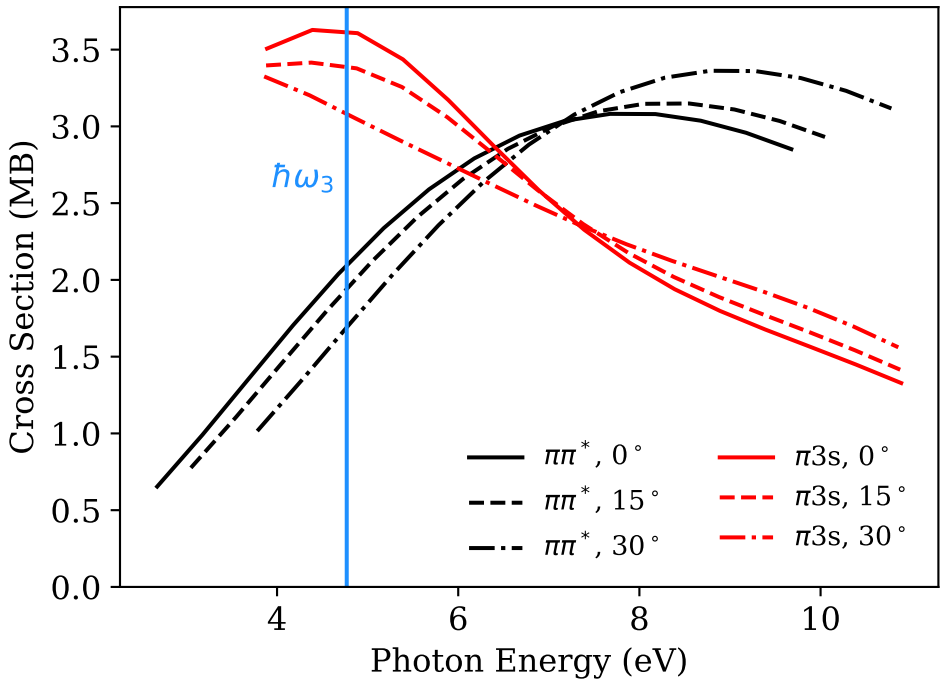

Figure 4.9: **Ethylene excited state photoionization cross-sections.** The ionization cross-sections of the $\pi\pi^*$ and π3s states of ethylene at planar and twisted geometries are shown as a function of the probe photon energy. Detection of population in the Rydberg state will be more probable at lower probe photon energies, where its cross-section is higher than that of the $\pi\pi^*$ state.

with similar experiments in ethylene employing a different probe photon energy [50]. The detection window should not play a role here, as the wanted dynamics should occur within roughly 1 eV of the initial excitation.

The spectra, retrieved using the pBASEX algorithm[1] [100], at several pump-probe time delays are shown in fig. 4.10. As a comparison, one-color photoelectron kinetic energy spectra obtained with 40.8 eV light or multiphoton ionization at 260 nm are also shown. The spectra are also plotted against the photoelectron binding energy $\mathcal{E}$, defined here as:

$$\mathcal{E} = \sum \hbar\omega - \mathrm{KE}_{e^-}. \tag{4.5}$$

This relabeling allows direct comparison between spectra obtained with differing probe wavelengths.

The one-color spectra show sharp peaks due to vertical ionization to the X and A states of the cation at binding energies 10.5 and 13 eV, respectively. The two-color spectra, however,

[1] See section 3.2.

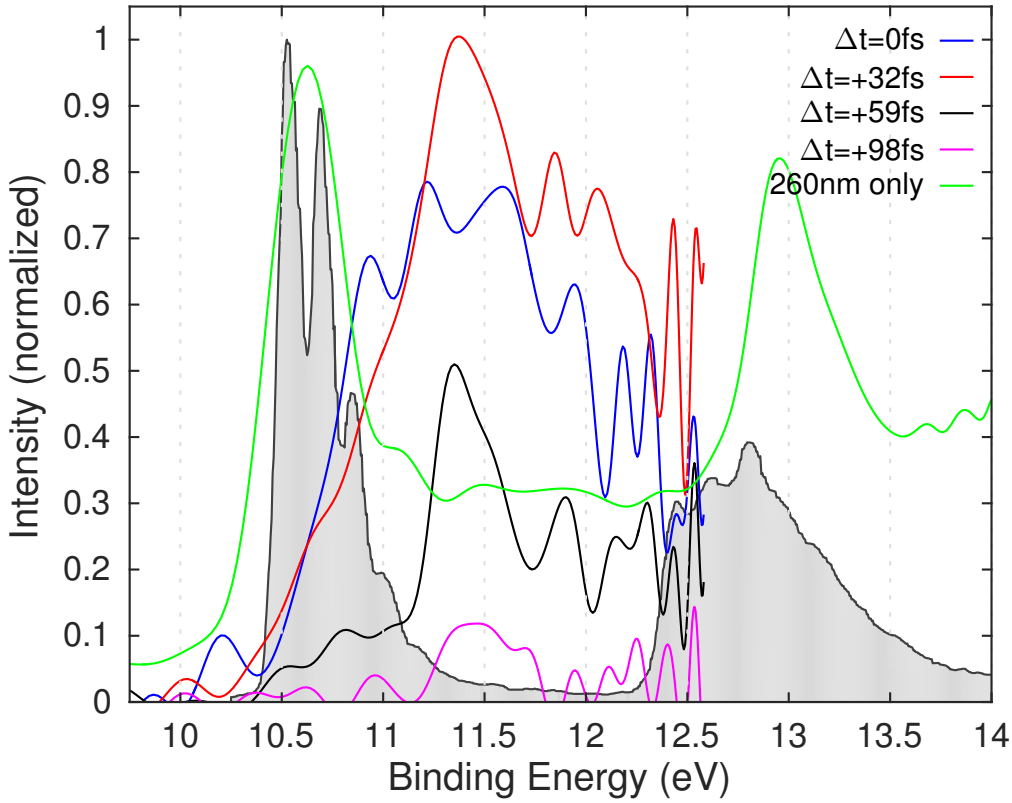

Figure 4.10: **Ethylene photoelectron kinetic energy spectra.** Energy spectra retrieved for one-color (260 nm in green, and 40.8 eV in grey) and two-color (156 nm and 260 nm in blue, red, black, and pink) ionization of ethylene at several pump-probe time delays. The one-color spectra show peaks at binding energies of 10.5 and 13 eV, corresponding to vertical ionization to the X and A cation states. The two-color spectra are broad, indicating the fast dynamics. The XUV spectrum is taken from [153]. Figure adapted from [51].

show no such peaks. This is due to the fast dynamics happening in ethylene following $\pi\pi^*$ excitation, notably the torsion discussed above. As shown in fig. 4.8, the binding energy of the $\pi\pi^*$ state quickly increases with even a moderate amount of torsion. The dynamical simulations[150, 151] predict a timescale for torsion on the order of 10 fs or less, which is below the widths of our pump and probe pulses. As a result, time-average smearing leads to these broad measured spectra, where the excitation is sampled at many different torsional nuclear geometries, even at the nominal pump-probe time overlap. Still, some of these torsion dynamics can be resolved. Notably, a shift of these broad spectra to higher binding energies is observed as the pump-probe time delay is increased. This will be further discussed in section 4.6.

Beyond this shifting dynamics, these spectra also reveal the population of the low-lying π3s Rydberg state. While not seen at the pump-probe time overlap, a sharp peak begins

to appear and becomes more prominent at the later time delays. The position of this peak remains constant in time at a binding energy of ∼11.4 eV, as expected for a feature attributed to ionization from a molecular Rydberg state. This peak is shifted by ∼0.9 eV from the ionization potential of 10.5 eV, which should correspond to the energy difference between the excitation energy and the energy of the Rydberg state in the equilibrium geometry. According to this measurement, the π3s should have a vertical excitation energy of ∼7.05 eV. There are various calculated energies for this state [150, 151], many of which lie between 7 and 7.5 eV. Since, in general, the methods used overestimate excitation energies [150], these values show decent agreement with the measurement.

Although the molecules are not aligned in the lab frame, we can expect some differences in the angular distributions of photoelectrons coming from the $\pi\pi^*$ and π3s states, as the polarization of the light can break the angular symmetry of the initial ethylene gas ensemble [102]. As mentioned above, the selection rules for the excitation should selectively excite ethylene molecules which have a C–C bond aligned with the polarization, resulting in a dipolar distribution of excited molecules. The ionization step is less strict, but we can also expect, and observe for the several geometries calculated above, different cross-sections for ionization with light polarized parallel or perpendicular to the molecular axis.

Since two photons are involved in the ionization, the experimental angular distributions should be representable using two parameters $\beta_2(E,t)$ and $\beta_4(E,t)$, such that the total energy and angular distribution of photoelectrons goes as:

$$I(E,\theta,t) = I(E,t)\left[1 + \beta_2(E,t)P_2(\cos\theta) + \beta_4(E,t)P_4(\cos\theta)\right], \tag{4.6}$$

where $P_i(x)$ represents the i-th order Legendre polynomial. The extracted anisotropy parameters $\beta_2(E,t)$ are shown in fig. 4.11. At binding energies below 11.3 eV, we find a positive and relatively constant anisotropy parameter of $\beta_2 \approx 0.5$. The highest anisotropies are found between binding energies of 11.3 and 11.7 eV, in the vicinity of the Rydberg feature seen above, with β_2 closer to 1. Since the Rydberg electron orbital can be approximately treated as an atomic s-orbital, we can expect photoelectrons ionized from it to exhibit a higher degree of anisotropy than those coming from the π^* orbital, which has a more complicated nodal structure [154]. The values of β_4 are near zero within the measurement error for all energies and time-delays measured.

The observation of the population of this low-lying Rydberg state has broader implications, as such states have generally been ignored in molecular dynamics simulations. The participation of such states has also been observed in other systems including methyl-substituted ethylenes [155], furans [36, 156], and pyrroles [157], indicating that ethylene may not be an isolated case.

4.6 Resolving the nuclear wavepacket

The full experimentally measured TRPES is shown in fig. 4.12. The Rydberg state peak at 11.4 eV at the later time delays is again apparent. This full TRPES also better shows the

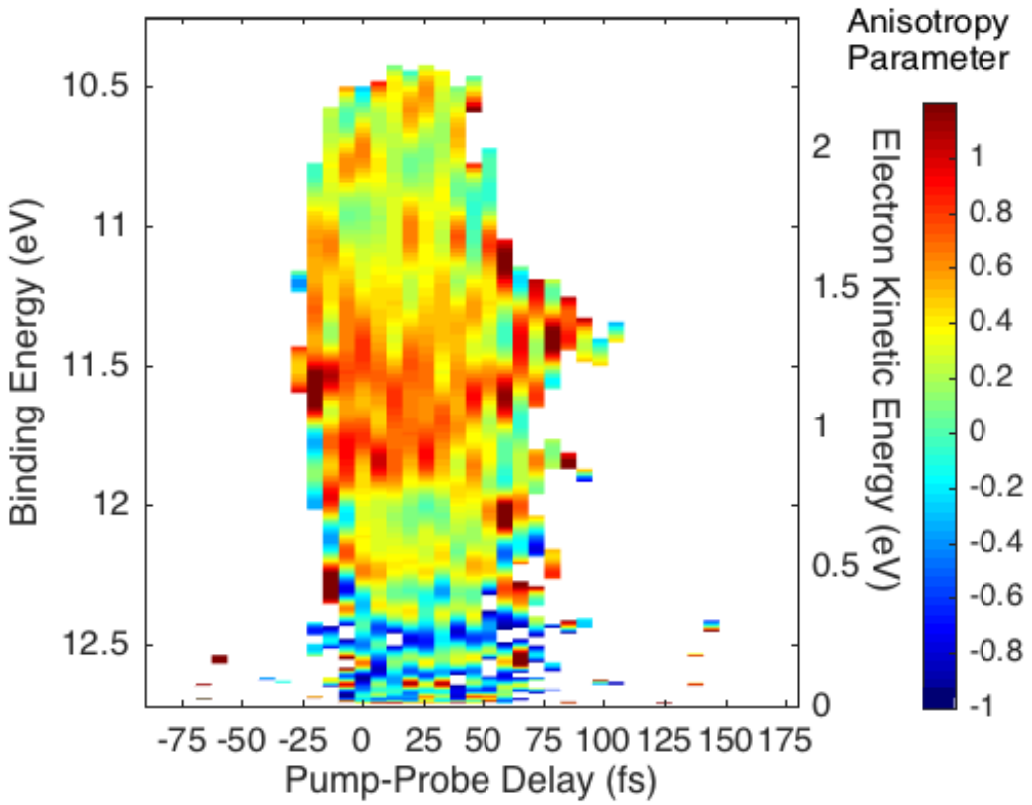

Figure 4.11: **Ethylene time-resolved photoelectron angular distribution.** The angular anisotropy parameter β_2 is shown as a function of energy and time delay. In time-energy bins where the total signal was less than 10% of the maximum signal, the measurement error becomes excessively large and the values were not plotted. Figure adapted from [51].

energy-shifting feature in the leading edge.

To better quantify this feature (as well as capture the ultrafast decay dynamics), a fitting procedure which allows for this shift is required. As a simple attempt, we will try to fit the full dataset $\mathrm{I}(\mathcal{E}, t)$ one energy slice at a time, such that:

$$\mathrm{I}(\mathcal{E}, t) \approx A(\mathcal{E}) f(t; \vec{p}(\mathcal{E})), \tag{4.7}$$

where $\vec{p}(\mathcal{E})$ represents some array of fit parameters which will depend continuously on the binding energy. The choice of $f(t; \vec{p}(\mathcal{E}))$ is not straight-forward, as this parametrized function must attempt to account for any time-dependence that the measured electron yield may take given the complex molecular dynamics occurring. For example, for ethylene, we might expect needing some oscillatory component due to potential revivals in the torsion coordinate, with some decay features as the other coordinates take the excitation away from the FC region. In practice, the data do not show these revivals, likely due to their short period as compared to the pulse widths of the experiment, and a simple model involving only exponential decay

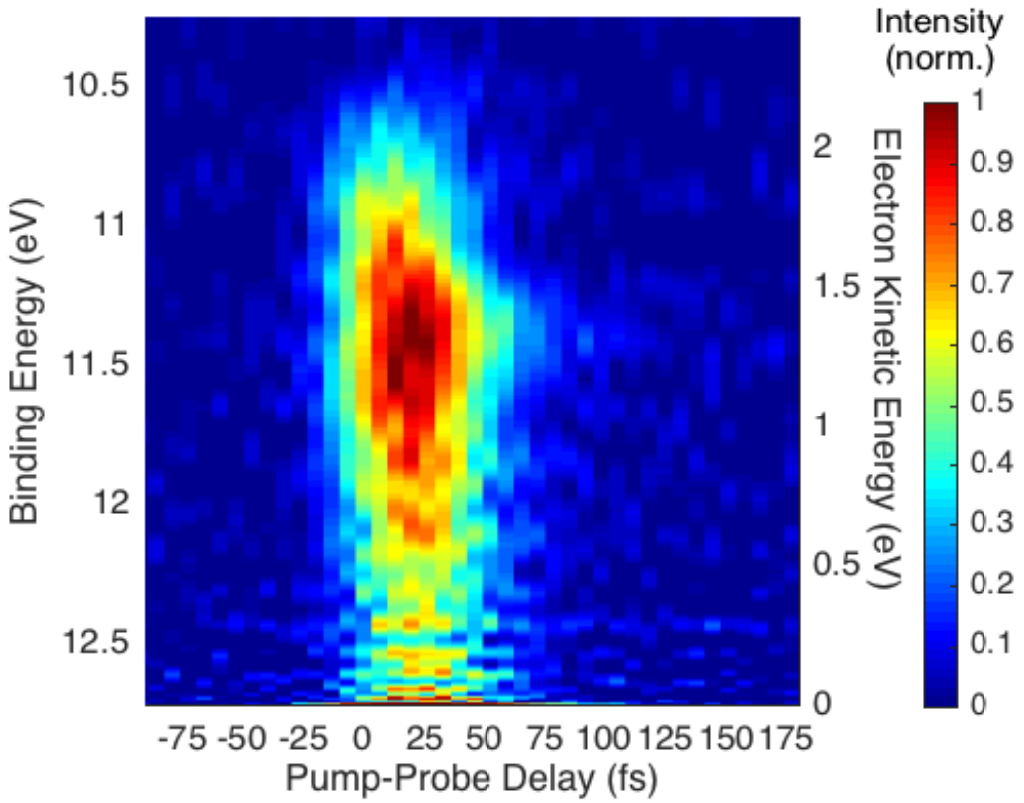

Figure 4.12: **Ethylene TRPES at 260 nm.** Broad spectra following $\pi\pi^*$ excitation indicates the fast motion happening on timescales faster than the instrument response time. The persistence of signal at binding energies of 11.4 eV indicates population of the π3s state. Figure adapted from [51].

is used, fitting the measured data decently. The energy-shifting feature is accounted for by adding a fit parameter $t_0(\mathcal{E})$, a signal onset time for the exponential decay. We thus turn to a function of the form:

$$I(\mathcal{E},t) = A(\mathcal{E})\left[H(t-t_0(\mathcal{E}))\times\exp\left(-\frac{t-t_0(\mathcal{E})}{\tau(\mathcal{E})}\right)\right]\otimes g(t-t_0(\mathcal{E});\sigma), \tag{4.8}$$

where $H(t)$ is a step function and $g(t;\sigma)$ represents a Gaussian function of width σ taking into account the instrument response as well as wavepacket broadening [51]. This Gaussian width can be fit independently for each energy slice, but can also be kept as a global fit parameter, yielding similar results. This model will extract the energy dependent signal onset times $t_0(\mathcal{E})$ and signal decay times $\tau(\mathcal{E})$, with the former quantifying the dynamical spectral shift and the latter specifying the ultrafast decay features (again, which are mainly due to a detection window effect and do not directly represent any lifetime of the system). The fit results are shown in fig. 4.13. The signal decay times are mostly constant across all

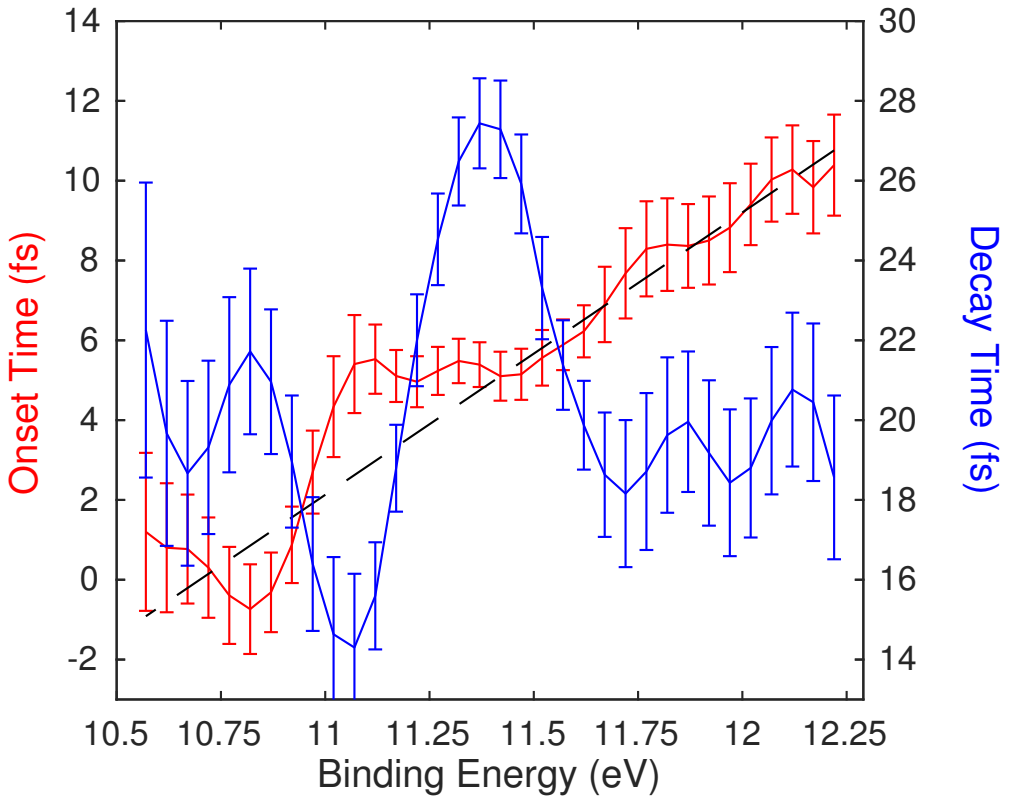

Figure 4.13: **Ethylene TRPES Onset and Decay Fit.** Results of the TRPES fit according to eq. (4.8): signal onset times (t_0, red, left) and signal decay times (τ, blue, right) for 100 meV slices of the full TRPES. The onset times show a monotonic, mostly linear increase going to higher binding energies, while the signal decay times show an increase at the energetic location of the Rydberg state. Figure adapted from [51].

binding energies, besides a region around 11.4 eV, where there is an increase from ∼20 fs to 28 fs. This is again due to the Rydberg state.

The signal onset times give a different piece of information. Notably, we can interpret them as a metric for nuclear dynamics. Reversing the dependence, we can go from $t_0(\mathcal{E})$ to $\mathcal{E}(t_0)$, and interpret this function as the time delay needed for part of the vibrational wavepacket to reach a nuclear geometry with binding energy $\mathcal{E}$. While revivals in signals for a given energy slice were not observed, mainly due to the time resolution allowed by the light pulses used in the experiment, this onset time analysis allows for the resolution of the first torsion motion of the molecule. As the molecule twists on the $\pi\pi^*$ PES, its binding energy quickly increases. Since this twisting motion dominates nuclear dynamics on the sub-10 fs timescale, we can approximate that any change in binding energy is due to motion along this torsion coordinate [150].

Going one step further, we can attempt to combine this onset time data with the PES

calculations along some identifiable reaction coordinate to track the excitation. Following the definition of eq. (4.5), we can similarly define the binding energy extracted from a PES calculation as:

$$\mathcal{E}_i(\vec{\mathbf{R}}) = \mathrm{E}_c(\vec{\mathbf{R}}) - \mathrm{E}_i(\vec{\mathbf{R}}) + \mathrm{E}_0, \tag{4.9}$$

where $\vec{\mathbf{R}}$ represents the nuclear geometry and $\mathrm{E}_c(\vec{\mathbf{R}})$ and E_0 represent the energy of the cation and the initial excitation energy, respectively. We see that the binding energy of 11.4 eV is reached in roughly 5 fs after excitation. The binding energy of the Rydberg state does not strongly depend on the torsion coordinate and can be assumed to be constant at this energy. The crossing of the π3s and $\pi\pi^*$ states must then occur at this energy as well, corresponding to a torsion angle of $\sim$27°. This geometry should be reached within 5 fs of excitation, in agreement with the dynamical simulations of [150]. The data also indicate that the maximally attainable binding energies of 12.72 eV, corresponding to the sum of the pump and probe photon energies, is attained in $\sim$10 fs. This binding energy, again ignoring other nuclear degrees of freedom, corresponds to a torsion angle of roughly $\sim$50° according to available curves [150, 151].

A higher energy probe photon would increase the experimental detection window. However, after 10 fs, other nuclear degrees of freedom, including the pyramidalization coordinate, are predicted to become active. The measurement of the time- and energy-dependent signal onset times is fundamentally a one-dimensional measurement and thus does not contain enough information to extract signatures of nuclear motion when two or more dimensions are involved. A possible solution to these limitations is presented in chapter 6.

Sub-pulse width resolution

As seen in fig. 4.13, the quantification of the energy-dependent photoelectron signal onset times $t_0(\mathcal{E})$ enables sensitivity to molecular configuration much below the experimental pulse widths. Small shifts in the appearance time of signal at nearby binding energies are seen at the one to a few femtosecond timescale. Since these shifts depend directly on changes in the molecular geometry, they enable the tracking of the excited state wavepacket with temporal sensitivity also on this sub-pulse width timescale.

Such super-resolution in time-resolved experiments has been argued for previously in many experiments also exploring ultrafast molecular dynamics [158, 132, 133]. In these, lifetimes much shorter than the pump-probe cross-correlation width are extracted by measuring slight changes to this cross-correlation signal when interacting with the molecular system of interest. As discussed previously, this measured lifetime may not represent the actual lifetime of an excited state due to detection window effects [135], but it will still depend on some dynamics of the system. Modeling the instrument response $g(t;\sigma)$ as a Gaussian of width σ and the system response $f(t;\tau)$ as a decaying exponential with lifetime τ, as is often

done [158, 132, 133], will lead to a measured signal $I(t)$ of the form:

$$I(t) = f(t;\tau) \otimes g(t;\sigma) \tag{4.10a}$$

$$= \int_{-\infty}^{+\infty} f(t';\tau) g(t'-t;\sigma) dt' \tag{4.10b}$$

$$= \frac{1}{2\tau} e^{\frac{1}{2}(\frac{\sigma}{\tau})^2 - \frac{t}{\tau}} \mathrm{erfc}(\frac{\frac{\sigma^2}{\tau} - t}{\sqrt{2}\sigma}) \tag{4.10c}$$

$$\simeq g\left(t-\tau; \sqrt{\tau^2+\sigma^2}\right), \tag{4.10d}$$

where erfc(t) is the complementary error function. The measured signal for an instrument response width of 340 fs and a system lifetime of 20 fs are shown in fig. 4.14. The measured signal is slightly offset and also slightly broadened as compared to the instrument response. If the instrument response is measured alongside the primary signal with high precision and accuracy, direct extraction of the system response is possible through deconvolution without the need for model functions. In practice, however, deconvolution will not be robust in this scenario where $\tau \ll \sigma$ for even small amounts of noise in the measurements. Instead, fitting to one of eqs. (4.10c) and (4.10d) is more favorable, with the latter directly extracting the system lifetime from either the measured delay or broadening. In these cases, the measurement accuracy of these delays and widths limits the sensitivity of the measurement of short lifetimes. If a high accuracy in the pump-probe delay can be achieved, then the measurement of femtosecond lifetimes can be achieved. In a similar way, energy-dependent onset times measured in a TRPES can clock dynamics shorter than the instrument response.

Central to this lifetime extraction analysis is the approximation of the system response with some parametrized function, in this case a simple decaying exponential. Since the goal of these experiments is to interrogate the excitation $\Psi(\vec{r}, \vec{R}; t)$, which we can expect to have some complex dependence on both the spatial and temporal coordinates, this approximation may fall short. However, assigning a simple lifetime to these complex dynamics holds some merit due to the analogy that can be made between internal conversion and the transition state [25]. The success of this treatment implies the appropriate usage of kinetic models to describe the measurements. But, these molecular kinetics arise from underlying molecular dynamics and are built off of some averaging of the excitation $\Psi(\vec{r}, \vec{R}; t)$, both in space and time, implying that the success of this lifetime extraction implies a lack of sensitivity to the underlying dynamics.

The TRPES measurement presented above shows similar limitations. A simple decaying exponential is enough to accurately represent the measured time-dependent signal at any given energy, or even the integrated signal from a range of energies. Torsional dynamics, among other complicated changes in $\Psi(\vec{r}, \vec{R}; t)$, should result in some more complicated form of the system response, but the lack of temporal resolution leads to the more simple exponential decay, with a lifetime we can attribute to a molecular rearrangement to geometries that can no longer be efficiently ionized. However, while subsequent molecular dynamics suf-

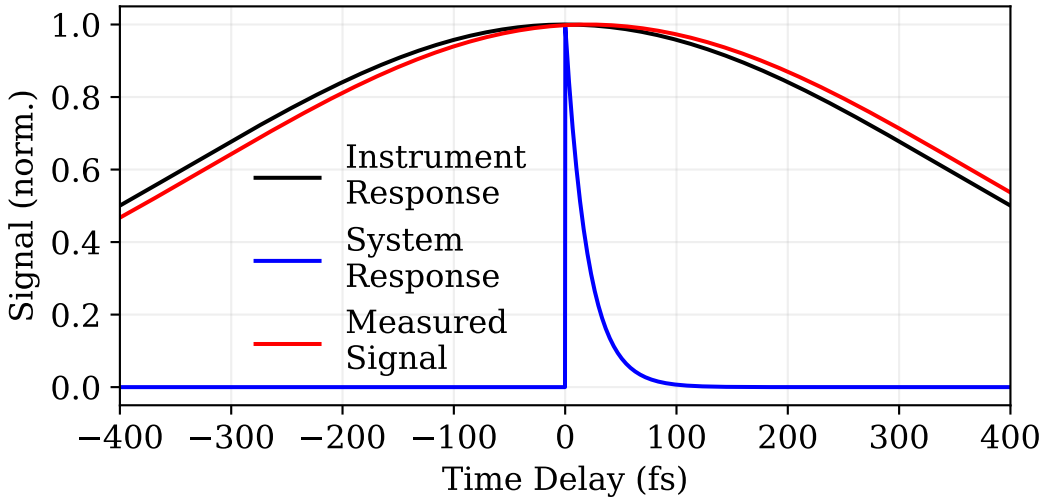

Figure 4.14: **Simulated short lifetime signal measured with long pulses.** A short system response (blue, 20 fs exponential decay) convolved with a long instrument response (black, Gaussian pulse with a 340 fs standard deviation) leads to a similarly long measured signal (red). Nevertheless, a small shift in the maximum of the signal is observed, which can reveal qualitative information of the ultrafast system lifetime.

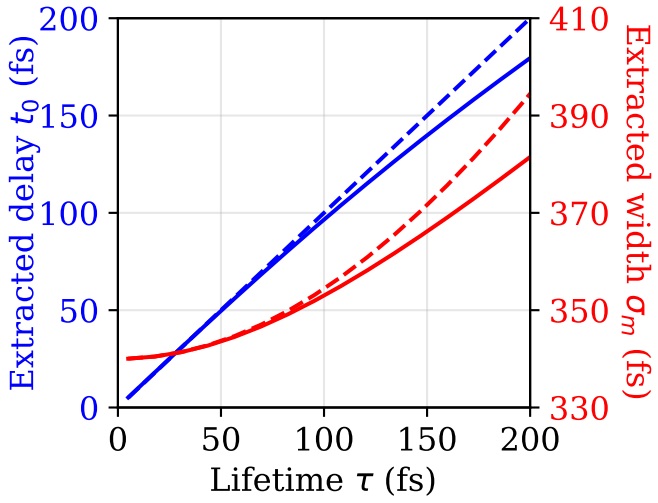

Figure 4.15: **Lifetimes from extracted signal delay and broadening.** Signal delays (solid blue) and widths (solid red) extracted from Gaussian fitting of the simulated measured signal for various system lifetimes. For short lifetimes, the delays directly follow the lifetimes (dashed blue), while the widths follow quadrature addition of the instrument response and the system lifetime (dashed red).

fer from time-average smearing, the onset time analysis in the TRPES allows for the direct observation of short timescale dynamics.

Chapter 5

Femtosecond scale non-adiabatic dynamics in neutral excited methanol

5.1 Excited State's of Methanol

To further explore our ability to resolve some ultrafast nuclear dynamics using TRPES, we also investigated excited state dynamics in methanol (CH_3OH). Methanol is found and has important applications in a broad range of areas, including chemical synthesis and solvation, astro- and atmospheric physics, energy transport, and alternative fuels [5, 159]. Like ethylene, methanol, being the simplest alcohol composed of two fundamental radicals, serves as an appealing polyatomic model system for studying excited state photochemistry involving non-adiabatic dynamics.

Methanol's first singlet excited state ($1\ ^1A''$, S_1) lies roughly 6.7 eV above the ground state (S_0) [160]. This excitation is comprised primarily of the promotion of an electron in belonging to an Oxygen out-of-plane lone pair molecular orbital to a delocalized molecular orbital with strong 3s character, as seen in fig. 5.1. This state was found to be dissociative along both the C–O and O–H bond coordinates, as seen in fig. 5.2(a-b) [161]. A concerted hydrogen breakup channel leading to CH_2O+H_2 also exists. A small barrier for C–O bond breaking leads to the domination of the other dissociation channels, which are direct and account for the ~ 30 nm wide absorption feature associated with this state [160, 162].

The absorption feature associated with S_2 photoexcitation spans from 160 to 151 nm and shows some vibrational progression [160], although the features are still broad and indicative of ultrafast dynamics. In contrast to photolysis at 185 nm through the S_1 state, many neutral dissociation channels have been observed following S_2 excitation [163, 164]. The C–O and O–H bond breaking channels, leading to CH_3+OH and CH_3O+H, respectively, are prominent at 157 nm excitation energies, with two breakup channels involving the methyl group (CH_2OH+H and CH_2O+H_2) also present. However, the S_2 state was found to be bound along both the C–O and O–H coordinates [161]. An apparent avoided crossing between the first two singlet excited states as the C–O bond is stretched from its equilibrium position of 1.42 Å

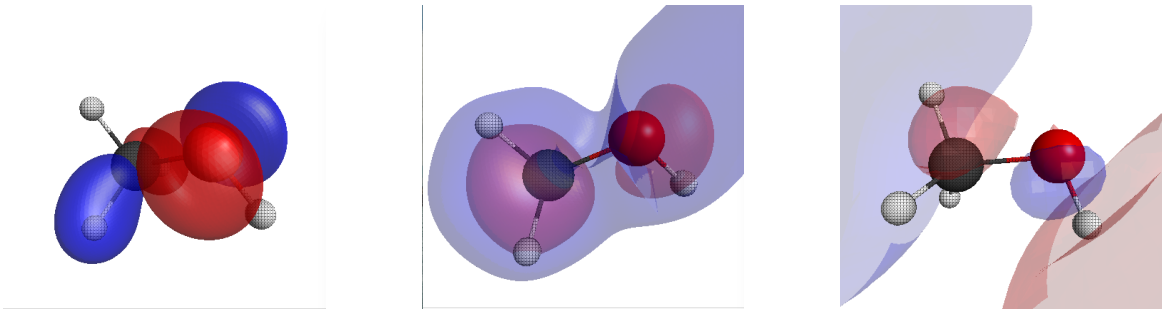

(a) (b) (c)

Figure 5.1: **Valence molecular orbitals of methanol.** (a) The highest occupied molecular orbital (HOMO) in neutral methanol corresponds primarily to an Oxygen out-of-plane lone pair which is antisymmetric with respect to the molecular plane. (b) The lowest unoccupied molecular orbital (LUMO) is composed primarily of delocalized 3s atomic orbitals on the Carbon and Oxygen sites. Although it is allowed by symmetry with a dipole perpendicular to the molecular plane, photoexcitation from the HOMO to this LUMO has a low cross-section due to the differing signs of the overlap integrals on these two atomic sites. (c) In contrast, promotion of an Oxygen out-of-plane lone pair electron to the next unoccupied orbital, corresponding to photoexcitation to the S_2 state, has a much larger cross-section.

helped explain these observed channels by invoking a non-adiabatic transition to and subsequent fragmentation on the S_1 PES [161, 163]. Along with their yields, these experiments also measured the kinetic energy release (KER) distributions of the photo-fragments [163, 164]. For the two main fragmentation channels, these distributions were relatively narrow and peaked just below the thermodynamically maximal measurable KERs for dissociations towards the joint S_0/S_1 asymptotic limits along both the C–O and O–H coordinates, further arguing for prompt dissociation on the S_1 surface after internal conversion from the initially excited S_2 state.

Similar experiments and excited state energy calculations were performed in the valence isoelectronic CH_3SH. Experimentally, photolysis studies at wavelengths corresponding to excitation of both the S_1 and S_2 states found qualitatively similar results to methanol, where the C–S and S–H bond breaking channels were prominent with most of the available energy going into kinetic energy release [165, 166, 167, 168]. Computationally, a conical intersection (rather than just an avoided crossing) between the S_1 and S_2 states was found using multiconfiguration self-consistent field configuration interaction wavefunctions requiring motion only along the C–S and S–H coordinates [169]. This conical intersection lies below the excitation energy of the S_2 state, making it energetically accessible and a candidate for explaining the observed dissociation dynamics. We also found this energetically accessible crossing using a coupled-cluster equation of motion routine in GAMESS on a two-dimensional grid of C–S and S–H bond lengths [17, 16]. Interestingly, performing an analogous calculation on methanol (as well as repeating it for several C–O–H bond angles as well as methyl geome-

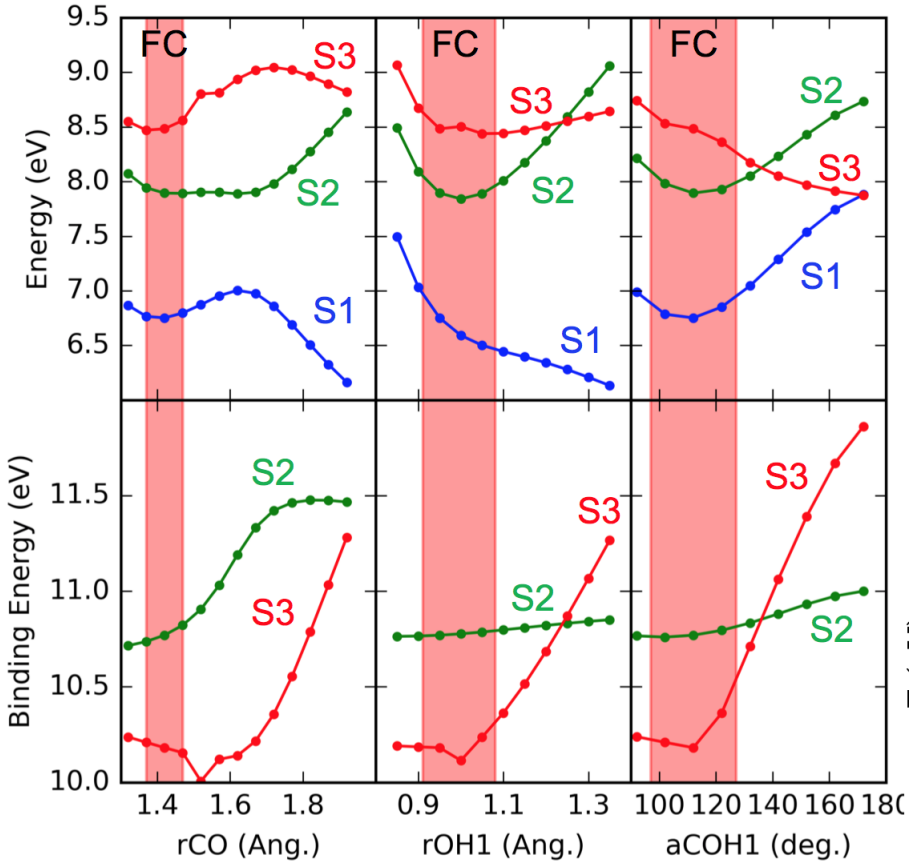

Figure 5.2: **Methanol excited state PES cuts.** The energies E_i (top) and binding energies $\mathcal{E}$ (bottom) of the first three singlet excited states (S_1, blue; S_2, green; and S_3, red) of methanol are shown as a function of the C–O bond (left), O–H bond (center), and C–O–H bond angle (right) coordinates, while holding the other nuclear degrees of freedom fixed to their equilibrium positions. Using the GAMESS package and an augmented CCD basis set, the ground, neutral excited, and ground cation state energies were calculated using coupled-cluster equation of motion methods [17, 16]. The Franck-Condon region, indicated by the pink shaded areas, were estimated by solving the Schrödinger equation for the vibrational ground state on the three-dimensional S_0 surface using a grid approach and the kinetic energy operator found in appendix A. The other nuclear degrees of freedom were ignored.

tries) could not reduce the S_1 and S_2 energetic separation below 0.6 eV at sampled geometries with energies below 8.5 eV (whereas the excitation lies near 8 eV).

5.2 Dynamic energy shifts in the TRPES

With a scheme similar to that employed in the previous chapter [170], the 5^{th} and 3^{rd} harmonics generated in the gas cell were selected to study methanol's excited state dynamics directly in the time domain. The 5^{th} harmonic, centered at 156 nm, efficiently photoexcites the system to the S_2 state to a broad feature lying slightly above the onset of absorption at 161 nm. The 3^{rd} harmonic serves as a photoionizing probe with a detection window of 1.87 eV large enough to follow the initial dynamics. A higher energy probe could be desirable to increase this window and give access to follow the H and H_2 formation channels directly, as described in section 4.2. However, a 4.77 eV probe beam limits the amount of final cation states available while also improving signal-to-noise since it is not energetic enough to ionize ground state population with a single photon.

Experimentally, vaporized methanol from a liquid cell at room temperature (98 Torr vapor pressure) flowed through a variable leak valve and reached the interaction region through a 100 μm diameter needle. The splitting of the beam into a pump and probe arm was scanned by translation of the second XUV-IR separation mirror, which translated the beam on the split-mirror. At each position, the total electron count rate was recorded at pump-probe temporal overlap and at a delay corresponding to the probe pulse arriving 230 fs early, as shown in fig. 5.3. While the "pump-probe count rate," defined as the count rate at pump-probe time overlap minus the count rate with the probe pulse arriving early, could be increased by adding more 3^{rd} harmonic at the expense of energy in the pump arm, the amount of background due to multi-photon ionization with the probe only increased at a faster rate. To improve signal-to-noise, the "pump-probe to background ratio," defined as the pump-probe count rate divided by the count rate with the probe pulse arriving early, was instead maximized by moving the beam 1.75 mm towards the 5^{th} harmonic coated mirror. The experiment was also conducted at a beam offset of 2.25 mm to verify that the acquired time-dependent data did not contain unwanted nonlinear effects by further reducing the intensity of the 3^{rd} harmonic.

The full TRPES data is shown in fig. 5.4. As was the case for ethylene, we observe broad spectra spanning binding energies from the ionization potential of 10.85 eV to the maximally measurable 12.72 eV, with signal decaying on time-scales of 10s to 100s of fs. Focusing first on the few-femtosecond dynamics, the signal onset times again shift to later times as the binding energy is increased, as shown in fig. 5.5. In order to quantify this shifting feature as well as the ultrafast signal decays, we fit these individual slices to exponential decays multiplied by a step function and convolved with a global Gaussian function, as in section 4.6:

$$I(\mathcal{E},t) = A(\mathcal{E})\left[H(t-t_0(\mathcal{E}))\times\exp\left(-\frac{t-t_0(\mathcal{E})}{\tau(\mathcal{E})}\right)\right]\otimes g(t-t_0(\mathcal{E});\sigma), \tag{5.1}$$

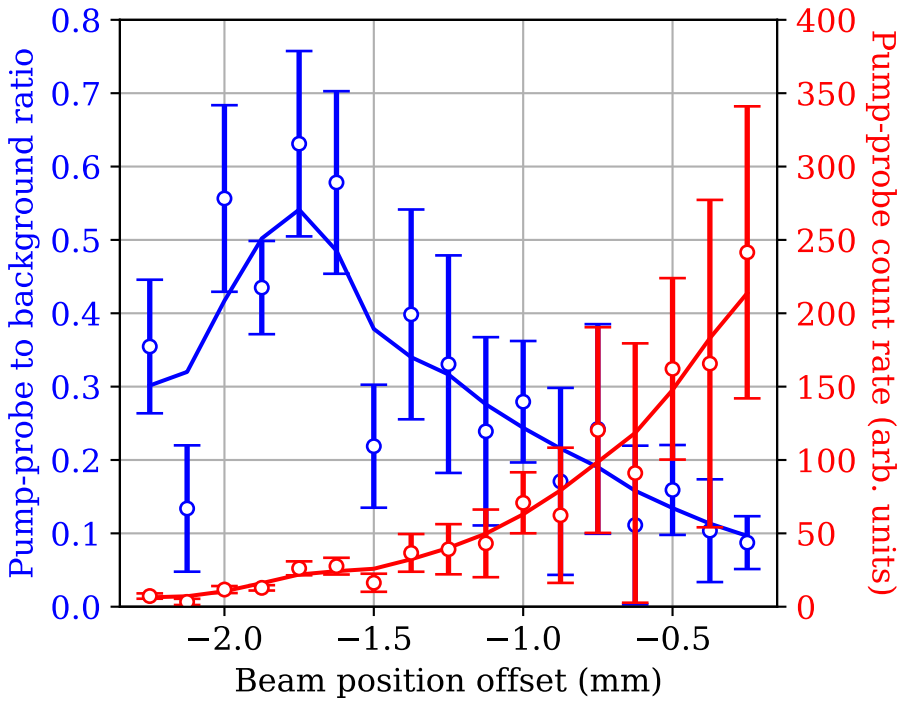

Figure 5.3: **Pump-probe energy splitting optimization.** The position of the beam on the split-mirror can be optimized depending on the experiment to achieve the best signal-to-noise ratio. In this experiment, multiphoton ionization from the pump and probe arm early presents an unwanted background signal alongside a spurious signal from electrons created by the interaction of stray photons with the spectrometer plates. Although it does not coincide with the highest rate of time-dependent counts, a beam position offset from center by 1.75 mm yields the highest ratio of time-dependent counts to background counts.

where $t_0(\mathcal{E})$ and $\tau(E)$ again represent the binding energy dependent signal onset and signal decay times. Although we can expect the evolving vibrational wavepacket to have some complex dependence on both the nuclear and temporal coordinates, which will lead to a similarly complex measured time-dependent signal, the relatively simple parametrized function above is selected for its ability to appropriately fit the data and avoid overfitting while still quantifying both the energy-shifting and ultrafast decay features. The signal onset times, shown in fig. 5.6 along with the signal decay times) retrieved from this model fit indicate that the excited wavepacket is born in the Franck-Condon region with a binding energy close to the ionization potential of 10.85 eV at the nominal experimental t_0. As indicated by the increase of the extracted signal onset times, this wavepacket evolves towards nuclear geometries of higher binding energies at later times. By changing from the retrieved binding energy dependent signal onset times $t_0(\mathcal{E})$ to a time delay dependent binding energy $\mathcal{E}(t)$,

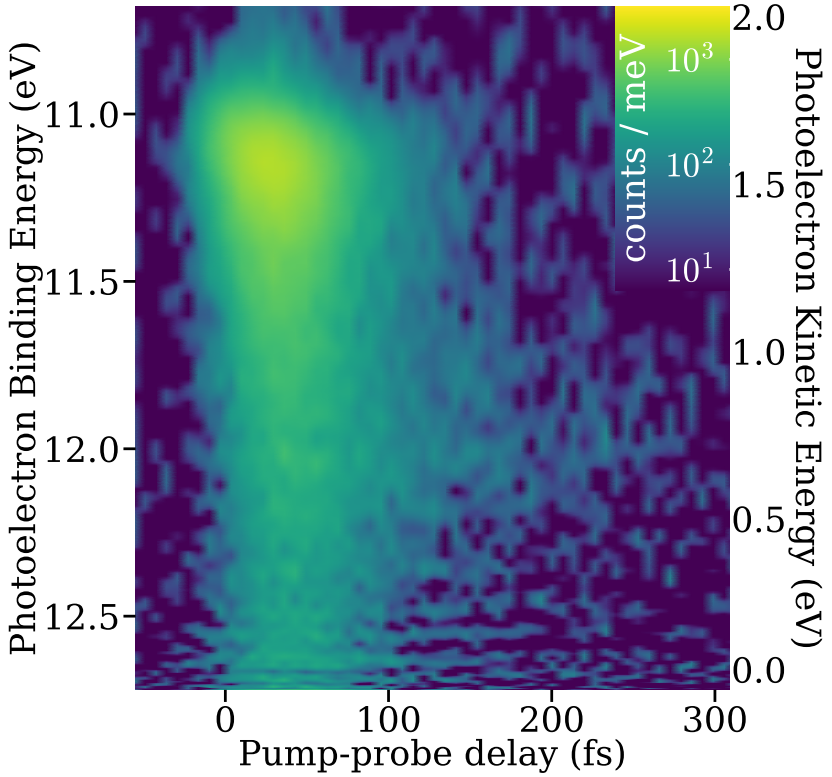

Figure 5.4: **TRPES of methanol excited at 156 nm.** Experimental TRPES data from ionization of the excited wavepacket with 260 nm light, taken in 6.57 fs delay steps. The background signal due to single pulse multiphoton ionization (2×5^{th} or 3×3^{rd} harmonic photons) was removed by subtracting the averaged spectra taken with the probe pulse arriving between 50 and 150 fs early. Photoelectrons are measured with kinetic energies up to ~1.9 eV, corresponding to direct vertical ionization from the Franck-Condon region and a photoelectron binding energy of 10.85 eV. Figure adapted from [170].

we observe a relatively constant rate of change of the binding energy of 0.045 eV/fs until 11.3 eV, at which point the rate abruptly increases to 0.3 eV/fs until the maximally measurable binding energy of 12.72 eV is reached. Later dynamics on the excited PES become difficult to resolve due to the ~20 fs pulse durations and are instead appropriately modeled by simple exponential decays. However, the measurement of these energy shifts overcomes this time-average smearing, enabling temporal resolution beyond the pulse width for the initial dynamics [171].

We also conducted a similar fit to extract energy-dependent signal onset times using the decay associated spectra (DAS) analysis used in many TRPES experiments [40, 35, 41], where the sum of a small number of global exponential decays is used to fit each energy slice

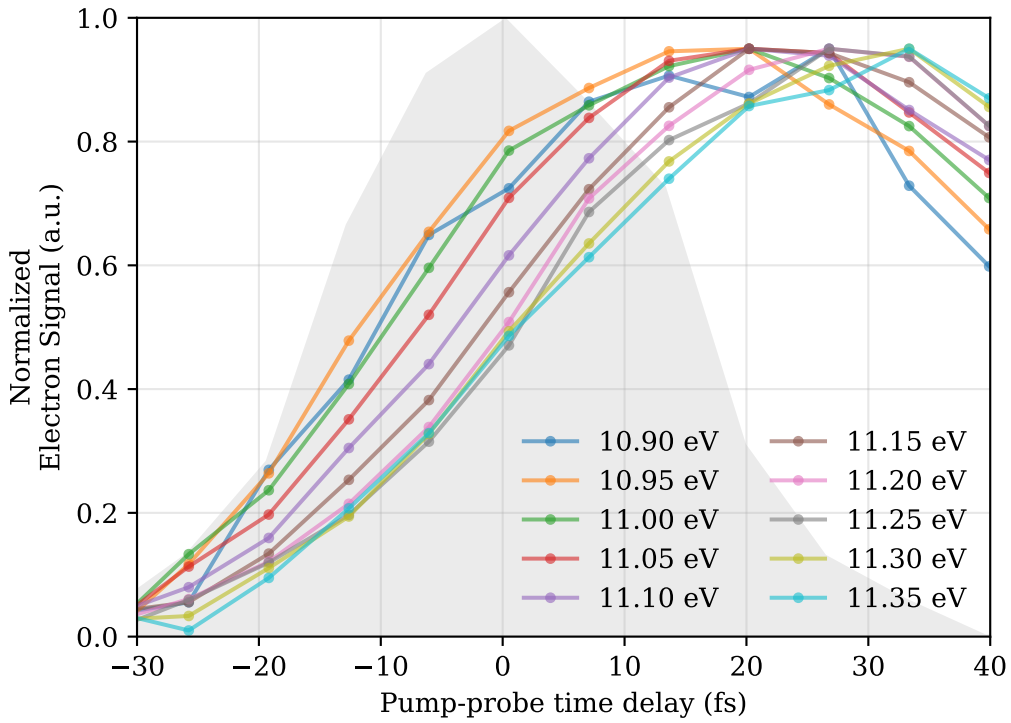

Figure 5.5: **Onset times of photoelectron energy slices.** The time-delay dependence of normalized 50 meV energy slices centered at binding energies between 10.90 and 11.35 eV reveals the dynamical spectral shift associated with the femtosecond scale nuclear motion induced by photoexcitation. The instrument response, measured by non-resonant two photon ionization of Xenon and shown as the shaded gray region, is much wider than the observed shifts.

rather than a single local exponential decay:

$$I(\mathcal{E},t) = \sum_{i}^{N} A_i(\mathcal{E}) \times \exp(\frac{t - t_0(\mathcal{E})}{\tau_i}) \otimes g(t - t_0(\mathcal{E}); \sigma). \tag{5.2}$$

Only $N = 2$ DAS are required to fit the experimental data accurately, yielding decay times of 25 and 72 fs with amplitudes $A_i(\mathcal{E})$ shown in fig. 5.7 along with the signal onset times $t_0(\mathcal{E})$. Focusing on the latter, we see good agreement between the extracted shifting onset times using either method. The two extracted lifetimes can be compared to the measured decay times for signals of the measured ionic fragments (which will be further discussed below), with relatively poor agreement. Since signal detection windows and large amplitude vibrational wavepacket motion are expected to play an important role, it is difficult to assign these lifetimes to some specific mechanism in a kinetic model representing the molecular dynamics, and the signal onset and decay times of fig. 5.6 will instead be referred to in the

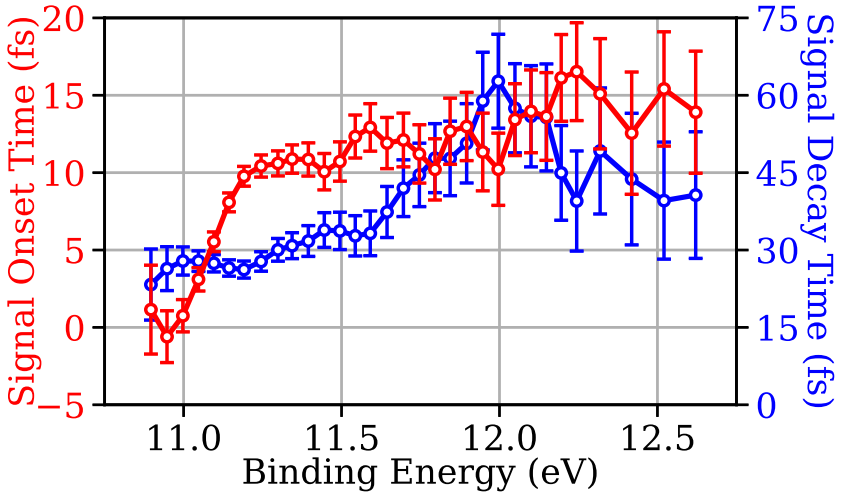

Figure 5.6: **Extracted binding energy dependent signal onset and decay times for methanol.** The onset times (red, left axis) monotonically increase with increasing binding energy, indicating nuclear motion towards geometries where the excited state is more bound. The signal decay times (blue, right axis) are relatively constant besides an increase localized around 12.0 eV. The slice widths are increased from 50 to 100 meV above 12.25 eV due to the reduced count rate at these energies. The error bars represent one standard deviation uncertainties found by estimating the covariance matrix of the parameters involved in the non-linear fit. This fit accounted for the uncertainties in the binned TRPES data, which were estimated by analyzing the variance in the signals of the 175 scans done at each time delay step. Figure adapted from [170].

following discussion.

The time-resolved measurements of shifts in the photoelectron binding energy are understood using previously calculated cuts of the excited state PESs [161, 169, 160] as well as those presented in fig. 5.2. The minima of the PES cuts along the O–H bond and C–O–H bond angle coordinates are coincident with the center of the Franck-Condon region. In contrast, the C–O bond should stretch from its equilibrium distance of 1.42 Å towards the minimum of the S_2 potential along this coordinate at 1.65 Å. If purely limited to this coordinate, this nuclear motion should shift the binding from the ionization potential of 10.85 eV to ∼11.3 eV. An abrupt change in the rate of change of the measured binding energy is observed near 11.3 eV, and we assign the shifts below this binding energy, which occur in the first 10 fs following excitation, to this C–O bond stretching on the S_2 excited PES. As discussed in the previous chapter, the low dimensionality of the measurement compared to that of the molecule makes it difficult to completely ignore the other nuclear degrees of freedom. However, the calculations of fig. 5.2 reveal a negligible dependence of the S_2 excited state's binding energy on the O–H bond and C–O–H bond coordinates. The photoelectron spectroscopy scheme employed here would not be sensitive to any nuclear motion along these

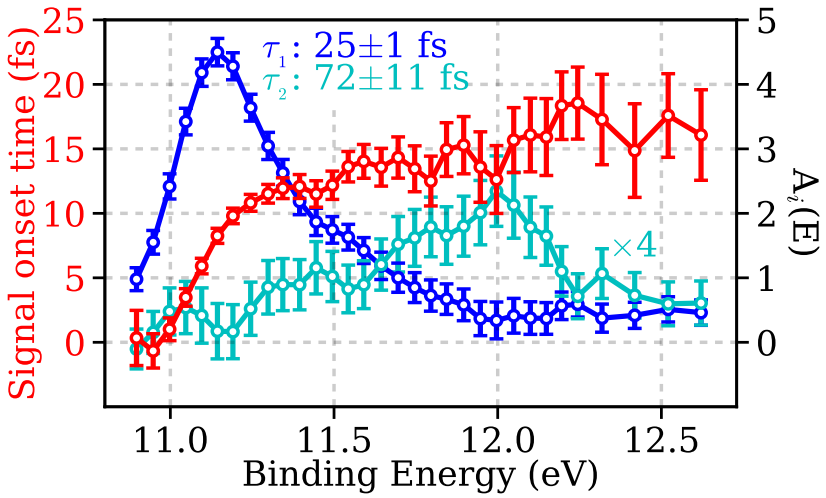

Figure 5.7: **Decay associated spectra analysis with onset times.** A DAS analysis returns similar signal onset times (red, left axis) as the single exponential decay model. The full TRPES is fit with a fast decay (25 fs, blue) localized at low binding energies and a slow decay (72 fs, cyan) predominantly at binding energies around 12.0 eV, coinciding with the peak observed in fig. 5.6.

internal coordinates. Instead, measured changes in the binding energy can be assigned almost exclusively in this picture to the C–O bond stretch, which affects the binding energy of the S_2 state more strongly.

After the excited wavepacket has reached the S_2 minimum, a non-adiabatic transition to a dissociative electronic state explains the increase in the rate of change of the measured binding energy beyond 11.3 eV. As previously mentioned, the S_1 state has been predicted to play a role due to its appropriate C–O and O–H dissociative limits, its apparent avoided crossing with the S_2 state, and the presence of a conical intersection which is energetically accessible without a barrier following S_2 excitation in the valence isoelectronic CH_3SH [161, 163, 164, 169]. In methanol, we performed a high-dimensional search for a conical intersection between the two lowest ^{1}A" excited states. While close degeneracies were located between the states at energies beyond $\sim$ 9 eV, no geometries were found with energies below or in the vicinity of the $\sim$ 8 eV energy of the S_2 state at the equilibrium geometry and energetic separations between the S_1 and S_2 states below 0.6 eV. Since states with energies much closer to degeneracy are typically needed for strong non-adiabatic couplings [21, 24, 25], we extended our search to conical intersections involving other excited singlet states. As seen in fig. 5.2, we observe a crossing between the S_2 and 2 ^{1}A' (S_3) states at an energy below 8.5 eV by simply opening the C–O–H bond angle from its equilibrium 109° to 135°, which was not considered in the previous calculations [161, 160]. This S_3 excited state is well described in the Franck-Condon region as the promotion of an Oxygen in-plane lone pair electron (rather than an out-of-plane lone pair electron for S_1) to the lowest unoccupied molecular

orbital. While the S_3 state does not appear clearly dissociative in the one-dimensional PES cuts presented in fig. 5.2 (unlike the S_1 state), the opening of the C–O–H bond angle brings the S_1 and S_3 states together as the distinction between the in- and out-of-plane lone pairs is lost. For large C–O or O–H bond distances, this angle should not affect the electronic state energies and we can expect the S_3 state to share the S_1 dissociative limits since they are degenerate for geometries with C–O–H angles of 180°. The measured KERs for the various dissociation channels following 157 nm excitation to the S_2 state [163, 164] can thus also be explained by dissociation following internal conversion on the S_3 state rather than S_1.

While the one-dimensional potential in fig. 5.2 indicates an energetically uphill path to C–O–H bond opening, small stretching of the C–O bond, as is expected, enables this bond opening. Without optimization of any other nuclear coordinates, we find a small range of barrierless linear pathways in the two-dimensional C–O bond and C–O–H bond angle PES from the ground state equilibrium geometry to a geometry where the S_2 and S_3 states are degenerate. These crossing geometries are localized with C–O bond lengths near the 1.65 Å minimum for the one-dimensional PES cut and have binding energies between 11.3 and 11.4 eV, in agreement with the location of the abrupt increase in the rate of change of the measured photoelectron binding energy of fig. 5.6. Since no such geometries are found between the S_1 and S_2 states, we assign the dominant dissociation channels of methanol following S_2 excitation to dynamics involving the S_3 state rather than the S_1 state mentioned in previous studies [163, 164].

As previously mentioned, the C–O–H bond opening has only a small effect on the binding energy and so the changes of the binding energy along these two-dimensional paths are almost identical to those along the one-dimensional C–O stretching pathway. Using the calculated binding energy curves, we can interpret the shift from binding energies of 10.85 to 11.3 eV over 10 fs as a C–O stretch from the equilibrium 1.42 to 1.65 Å. With the simplest model assuming a constant bond stretch velocity of $v = \frac{\Delta R_{\text{C–O}}}{\Delta t}$ and using the reduced mass $\mu = \frac{m_{\text{CH}_3} m_{\text{OH}}}{m_{\text{CH}_3} + m_{\text{OH}}}$, we find a kinetic energy associated with this initial stretching motion of ~ 200 meV, which is in rough agreement with the various calculated values of the difference between the energies of the S_2 state at methanol's equilibrium geometry and at the S_2 state minimum geometry [161, 160]. Once on the S_3 PES, which is strongly dissociative along both the C–O and O–H bond coordinates when the C–O–H bond angle is opened, the binding energy will increase at a greater rate, as measured.

5.3 Signal decay and photoelectron–photoion correlations

The photoelectron signal at all energies decays on ultrafast timescales. For the TRPES at photoelectron binding energies associated with the S_2 state, the time-dependent data is well characterized by a single decaying exponential with parameters $\tau(\mathcal{E})$ between 25 and 30 fs. This timescale reflects the time needed for most of the initially excited wavepacket to move

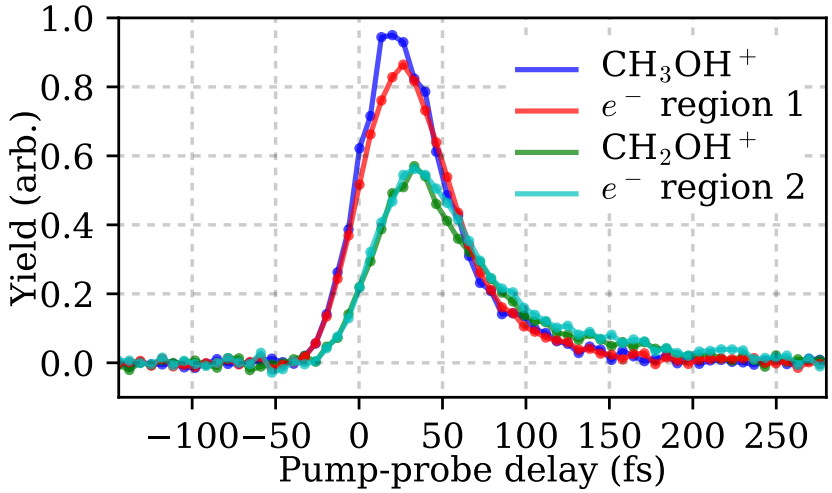

Figure 5.8: **Ion and electron correlations.** The pump-probe time dependence of the various ion and photoelectron channels reveals two correlations. The two e^- regions correspond to photoelectrons with binding energies below (red, fast decay) and above (cyan, slow decay) 11.6 eV. Since the detection efficiencies and the total experimental integration times were different for the ion and electron measurements, the total photoelectron and photoion yields were normalized. Figure adapted from [170].

away from the Franck-Condon region towards nuclear geometries with lower energies and higher binding energies, adding to the information supplied by the signal onset times. The vibrational structure seen in methanol's absorption spectrum at 156 nm has a $\sim$ 100 meV width [160], which, assuming static phase, corresponds to a $\sim$ 26 fs lifetime that is consistent with this measurement. Beyond this region associated with the S_2 state, the timescale for decay increases only slightly to $\sim$ 30 fs until binding energies between 11.6 and 12.25 eV are reached where we observe larger signal decay times between 30 and 60 fs.

Although there are many neutral dissociation channels following S_2 excitation, the combined pump and probe photon energies of 12.72 eV can only access the CH_2O^++H and CH_2O^++H_2 channels, with appearance energies of 11.6 and 12.4 eV, respectively[172]. Since this first energy of 11.6 eV closely matches the lower binding energy edge of the window of photoelectrons with longer signal decay times, we also measured the time-dependent fragment ion yields in the same experimental conditions besides the spectrometer voltages. We observed CH_3OH^+ (parent ion) and CH_2OH^+ (fragment ion) yields with fast rises near the pump-probe time overlap. There was no time-dependent CH_2O^+ signal observed above the noise levels. The signals of the observed parent and fragment ion yields decayed on ultrafast timescales, as expected from the associated photoelectron measurements and seen in fig. 5.8. Decay times of 30 and 45 fs were extracted for the parent and fragmented ion signals using the ansatz of eq. (5.1) without the energy dependence, with the onset of the CH_3OH^+ coinciding with the nominal t_0 and that of CH_2OH^+ signal being delayed by 7 fs.

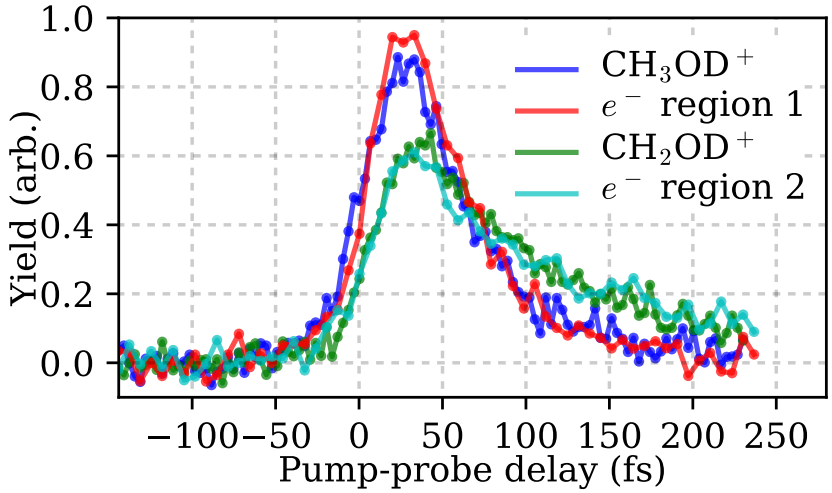

Figure 5.9: **Ion and electron correlations in hydroxyl-deuterated methanol.** As in fig. 5.8, correlations between the parent ion (blue) and low binding energy electrons (red) as well as between the fragment ion (green) and high binding energy electrons (teal) are observed. The total ion and electron yields are normalized to each other. The decay time for the CH_2OD^+ channel is much larger than that of the associated CH_2OH^+ channel in undeuterated methanol.

Table 5.1: **Correlated decay times.** Exponential decay times, in femtoseconds, extracted for the various ion and electron channel signals for the different isotopes, with errors representing the retrieved one standard deviation uncertainties in the fitting. The two photoelectron regions correspond to binding energies below and above 11.6 eV. NM indicates a channel that was not measured.

Channel	CH_3OH	CH_3OD	CD_3OH
Parent ion	30±3	43±6	36±6
e^- region 1	29±2	39±9	NM
Fragment ion	45±4	91±8	56±6
e^- region 2	48±4	97±16	NM

Although the electron and ion measurements were not performed in coincidence, fig. 5.8 reveals that the yield of the parent ion correlates well with that of all photoelectrons with binding energies below 11.6 eV, with the fragment ion and high binding energy (>11.6 eV) photoelectrons yields also matching. The experiments were repeated with both hydroxyl (CH_3OD, fig. 5.9) and methyl (CD_3OH) deuterated methanol and similar correlations were observed, as seen in the mono-exponential decay fit parameters for the various channels and samples reported in table 5.1. Deuteration did not strongly affect the extracted photoelectron onset times nor the appearance time of the fragmented species. This further indicates that the stretching of the C–O bond controls the rate of the initial dynamics

rather than hydrogen motion. In contrast, deuteration of either side of the molecule leads to substantial increases of the measured decay times, with hydroxyl deuteration having the largest effect even though fragmentation occurs on the methyl side of the molecule.

Although dissociation dynamics on the cation PES can also play a role and complicate our conclusions, we explain the feature in the TRPES with longer decay times around 12 eV with the CH_2OH+H neutral dissociation channel due to the measured correlation with the CH_2OH^+ fragment. With theory help from Dr. Loren Greenman at the University of California at Davis and Lawrence Berkeley National Laboratory, we again make use of cuts of the excited state PES and define a linear reaction coordinate involving the stretching of the C–H bond opposite to the hydroxyl hydrogen and an opening of the C–O–H bond, as before. Interpolating from the equilibrium geometry of the ground state towards towards the fragment, we calculate the energies of the first few excited states using equation of motion coupled-cluster theory with single and double excitations (EOM-CCSD) as well as the ground state of the cation using spin restricted open-shell coupled cluster theory, from which the binding energies could also be extracted. At geometries where the C–H bond was largely stretched, additional calculations with unrestricted reference functions (UHF-EOM-CCSD) ensured that multireference correlations did not significantly change the results. These calculations reveal a flat region along this reaction coordinate for the S_3 state and for C–H bond stretches beyond 2.0 Å on which the energy needed to ionize the system also does not increase, leading to a large detection-window as compared to the directly dissociative pathways of S_3 along the C–O and O–H bond coordinates. Many other two-dimensional linear cuts are possible, and we note that the one selected here is only representative rather than uniquely significant. Also, we expect further conformational changes involving other degrees of freedom along this fragmentation channel. Selective optimization of internal coordinates perpendicular to the combined C–H bond and C–O–H bond angle coordinate used here at several points did reveal a lowering of the S_3 excited state energy, but this change was roughly constant and was also reflected in the energy of the ground state of the cation. The binding energies of the S_3 state along this pathway remain relatively constant at a value of 12 eV coincident with the largest extracted decay times as seen in fig. 5.6. This reaction coordinate also explains the strong hydroxyl deuteration effect on the measured fragment ion lifetimes since it is enabled in part by this large opening of the C–O–H bond angle.

5.4 Summary and further work

As in ethylene, the dynamics of methanol immediately following photoexcitation involve considerable nuclear motion towards a conical intersection. Using TRPES and by extracting the shifts in the onset times of the time-dependent signal of photoelectrons at various binding energies, we are able to resolve this initial motion away from the equilibrium geometry with few-femtosecond sensitivity. Using calculated PESs for the involved excited states, a mapping can be made from nuclear geometries to binding energies. Although this mapping is not complete due to the high dimensionality of the system, the weak dependence of the

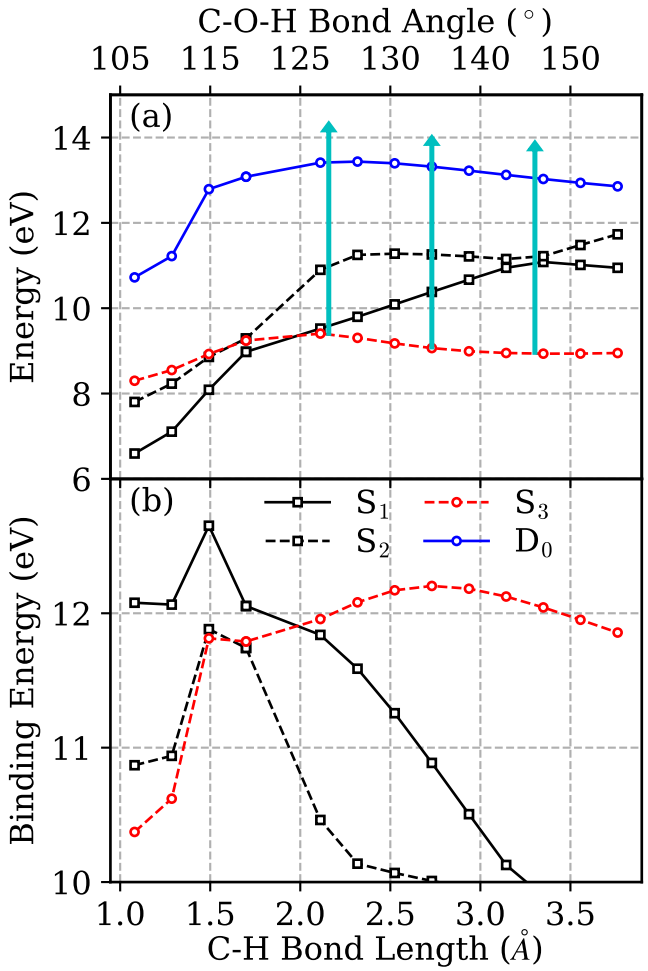

Figure 5.10: **Methyl hydrogen-loss coordinate.** The energies (a) and binding energies (b) of the S_3 state, shown alongside those of the S_1 and S_2 states as well as of the cation state (D_0), along a concerted C–H stretch and C–O–H bond opening coordinate reveal a reaction pathway that can lead to the observed CH_2OH^+ fragments when ionized by the probe (shown pictorially in teal). Beyond an initial stretch to 1.5 Å, the energy and binding energy of the S_3 state remain roughly constant, enabling ionization of the system at longer pump-probe time delays. Figure adapted from [170].

binding energy on certain molecular degrees of freedom (such as the O–H bond length and C–O–H bond angle) enable the localization of the excitation along the C–O coordinate with sub-Angstrom resolution.

While the 3^{rd} harmonic is well suited to track the evolution of the vibrational wavepacket shortly after excitation with the energy-resolved signal onset times of the TRPES measurement, it is not energetic enough to follow the full photochemical reaction as the final products (methyl, methoxy, and hydroxyl radicals as well as atomic and molecular hydrogen) will have ionization potentials above the 4.75 eV available here. Use of an XUV photon with energy beyond ∼15 eV as the probe, as was done in section 4.3 and elsewhere [173, 88, 48, 174], would enable a complete observation of the dissociation dynamics. Although this one-to-one mapping is not always valid and further analysis involving possible cationic dissociation would be needed, a measurement of the time-resolved yield of the ions associated with the final products mentioned above should help map out the full dissociation dynamics, beyond the first steps involving nuclear motion towards a conical intersection observed here. Additionally, high level ab initio molecular dynamics calculations [128] of methanol following its excitation to the S_2 state, which should be feasible and trustworthy given their agreement with measurements in ethylene presented above, would provide additional evidence for the role of the S_3 state in the dissociation dynamics.

Chapter 6

Conclusion and Outlook

6.1 Summary

Time-resolved experiments are a powerful tool for studying the femtosecond electronic and nuclear dynamics of molecules that often govern the outcome of photochemical reactions. The extension of pump-probe spectroscopy beyond the UV [175, 36, 37] extends the available probing schemes and also makes the excited states of small molecules, including ethylene [51], methanol [170], and carbon dioxide [174], accessible. The present work demonstrates progress in this direction, starting with the design and implementation of a bright HHG beamline that can provide spectrally and temporally tunable pump and probe pulses in the VUV/XUV. The 1 kHz repetition rate of this bright source required several engineering solutions to withstand both the high peak and average intensities, but enabled the more differential measurements of photoion and photoelectron imaging. These measurements were made in a VMI spectrometer with several optimizations specific to pump-probe experiments with potentially ionizing photons [106].

Ultrafast excited state dynamics in both ethylene [51] and methanol [170] were studied using time-resolved photoelectron spectra obtained with the 5^{th} harmonic as a pump and the 3^{rd} harmonic as a probe. Ultrafast processes involving hydrogen motion in both of these systems could be followed due in part to the ~ 20 fs duration and relative temporal stability of these pulses. Ultrafast decay of both photoion and energy dependent photoelectron signal was observed from which characteristic lifetimes for various relaxation processes could be extracted. Beyond these decay measurements and the kinetic models that they entail, dynamical spectral shifts were observed in the TRPES and assigned to vibrational wavepacket motion on the excited state PES [171]. Quantifying these shifts through the fitting of energy-dependent onset times of the photoelectron signal revealed the few-femtosecond sensitivity of these measurements. In ethylene, this sensitivity allowed the tracking of torsional motion on sub-10 fs time scales and the observation of the population of a low-lying Rydberg state in $\sim$5 fs, as predicted by theory [150, 151]. In the more complex methanol, combination of the experimental data with theoretical calculations of the excited state PES led to the identifi-

cation of an ultrafast reaction pathway towards a conical intersection leading to dissociation. This conical intersection was also found to be reached within 15 fs of excitation.

6.2 Outlook

Attosecond Dynamics: Electronic decoherence due to nuclear motion

Since it is the coupled motion of electrons and nuclei that leads to non-adiabatic dynamics, resolving such vibrational wavepackets created by impulsive photoexcitation is needed to form a more complete picture of molecular dynamics near conical intersections. However, observing such motion on femtosecond time scales has further applications. While coherent vibrational wavepackets evolve on the femtosecond time scale, coherent superpositions of electronic states created, for example, through excitation with broadband attosecond pulses or strong-field ionization exhibit dynamics on the attosecond (10^{-18}) time scale [176, 177, 178]. It has been postulated that the charge motion resulting from this electronic wavepacket could be used to control molecular reactions on the femtosecond timescale [179, 180, 181]. However, the simple picture of the beating of two or more electronic states could quickly deteriorate once the nuclear degrees of freedom become active. Decoherence of the electronic wavepacket has been predicted in several systems to be caused by sub-10 fs nuclear motion [182, 183]. Resolving this ultrafast nuclear motion alongside electronic decoherence would be an important step to further our understanding of attosecond molecular physics. Although it is not the only mechanism for decoherence, theoretical studies [182, 183] indicate that electronic states that undergo large energy changes due to motion along certain nuclear coordinates are most susceptible to this decoherence. Since it is these same energy changes that are measured and that few femtosecond resolution has been found to be necessary for the systems studied so far, the experimental techniques presented in this work could find use in these studies.

Channel-Resolved Photoelectron Spectra

Coincidence-type spectrometers described in chapter 3, which are limited to low data rates to avoid false coincidences, can yield fragmentation channel-resolved photoelectron spectra. However, a detector simultaneously collecting a photoelectron momentum spectrum and a photoion time-of-flight spectrum at higher signal rates [184, 185] should also have this capability by using covariance analysis and analyzing the correlated shot-to-shot variations in the measured photoelectron distribution and photoions [186, 187]. The yield of photoelectrons $f_m(r_j)$ associated with mass m can be estimated using:

$$f_m(r_j) = \mathbb{E}[(n_{e^-}(r_j) - \langle n_{e^-}(r_j)\rangle)(n_m - \langle n_m\rangle)], \tag{6.1}$$

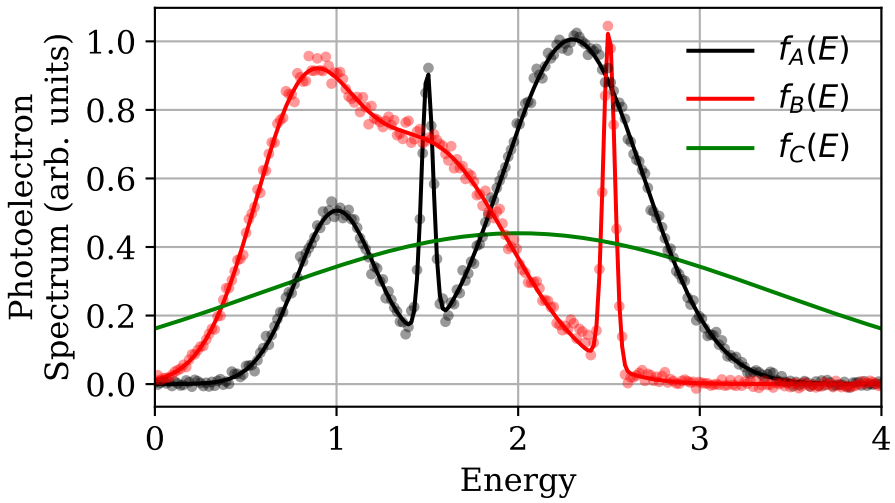

Figure 6.1: **Simulated and Extracted Channel Resolved Spectra.** Using covariance analysis, the photoelectron spectra corresponding to two real channels (black and red) and one background channel (green) can be separated. The sampled distributions are shown as solid lines and the associated extracted distributions are shown as dots. The simulation parameters used here are 25 counts/shot/channel, collection efficiencies of .7 and .6 for ions and electrons, respectively, and 10^6 shots.

where $n_{e^-}(r_j)$ is the number of electrons found at a radius r_j and n_m the number of ions of mass m found on a given shot. For small count rates, we can make the approximations $n_{e^-}(r_j) = \delta_{r_j}$ and $\langle n_{e^-}(r_j)\rangle \approx 0$.

The extraction of channel-resolved photoelectron spectra using simulated data is investigated below. Three channels with average per-shot count rates of μ_1, μ_2, and μ_3 are simulated, with channels A and B corresponding to the creation of both an ion with mass m_A or m_B and a photoelectron sampled from the distributions $f_A(E)$ or $f_B(E)$, as seen in fig. 6.1. Channel C corresponds to a background channel, with the creation of only an electron sampled from the broad $f_C(E)$. We see that the covariance analysis allows not only the separation of channels A and B, but also successfully rejects the background electron counts not associated with a target photoionization event.

The simulation runs on a shot by shot basis, where, for each shot: (1) the number of events in each channel is found sampling from a Poisson distribution, (2) the number of ions corresponding to channels A and B and electrons corresponding to channels A, B, and C are calculated by sampling a binomial distribution with the number of trials found from above and the success probability estimated to be 0.7 for ions and 0.6 for electrons (due to the non-unity detection efficiency of an MCP), and (3) the energies of each detected electron is found by sampling the appropriate distribution $f_i(E)$. With this data, the matrices $\mathbb{C}_A$

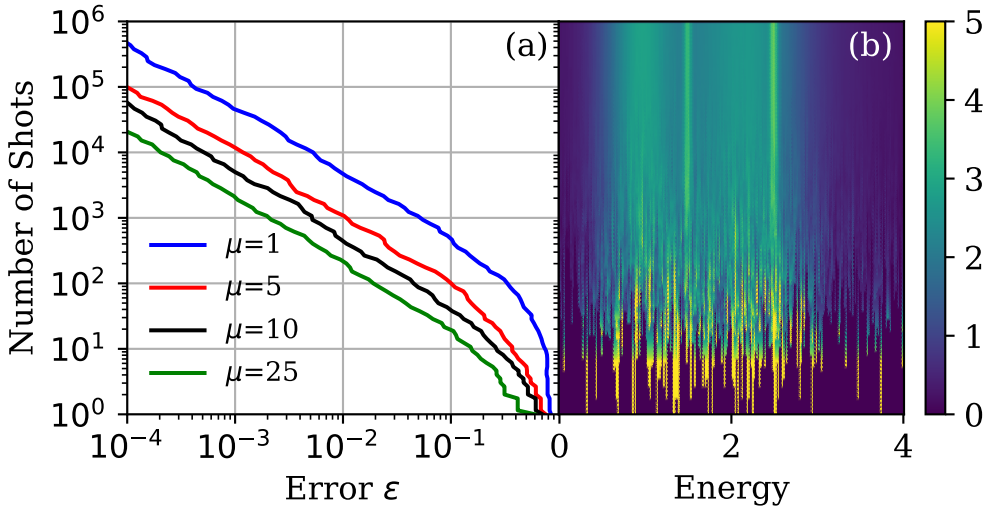

Figure 6.2: **Convergence of Measured Total Photoelectron Spectrum.** (a) The convergence of the measured total photoelectron spectrum, averaged over all three channels, to the sampled spectrum, using the error metric defined in the text, for varying experimental signal channel rates $\mu_1 = \mu_2 = \mu_3 = \mu$. (b) The evolution of the simulated spectrum as the number of shots increases for μ=5.

and $\mathbb{C}_B$ can be constructed and the distributions $f_A(E)$ and $f_B(E)$ extracted. In fig. 6.2, we show the simple convergence with an increasing number of shots of the total measured photoelectron distribution for several count rates. The error metric ϵ, varying between 0 and 1, between measured ($f_m(E)$) and expected ($f_e(E)$) distributions is defined as:

$$\epsilon = 1 - \frac{\int f_m(E) f_e(E) dE}{\sqrt{\int f_m(E)^2 dE \int f_e(E)^2 dE}}. \tag{6.2}$$

As expected, higher count rates lead to a faster convergence following the signal-to-noise ratio trend of the square root of the number of events. The convergence of the extracted channel-resolved photoelectron spectra, shown in fig. 6.3, have a different trend, with a relatively constant number of shots needed for convergence irrespective of count rate μ, at least for the range of parameters simulated here. Instead of needing more and more counts, as did the total photoelectron spectrum, the channel-resolved spectra are extracted by comparison of more and more shots, each with correlated fluctuations. For VUV/XUV pump-probe experiments, experimental considerations, such as photon flux and maximum target gas pressures, limit the signal rates rather than acquisition. Higher rates of acquisition for the same time-averaged signal rate would not improve the measure of the total photoelectron spectrum but would be beneficial for this channel-resolved spectra method. For example, a camera operating at 1 kHz of the laser rather than the ∼37 Hz used in the experiments

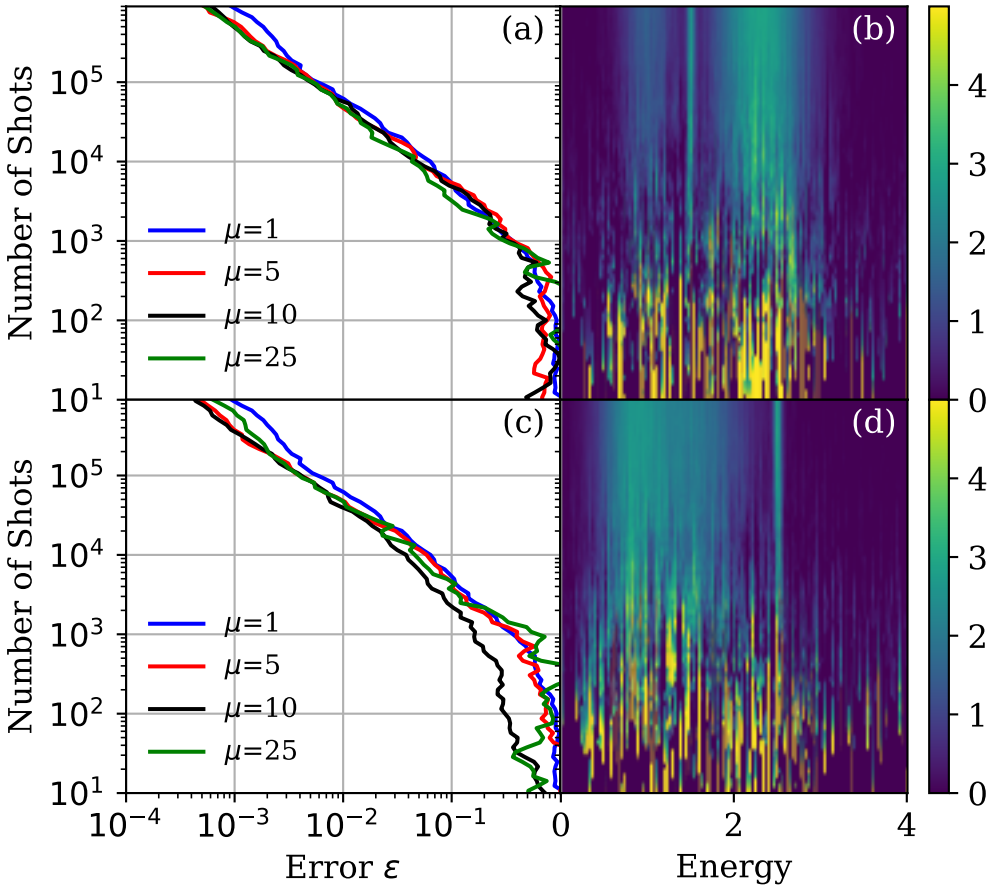

Figure 6.3: **Convergence of Measured Channel-Resolved Photoelectron Spectra.** (a) The convergence of the extracted photoelectron spectrum for channel A for varying signal rates. (b) The evolution of the extracted channel-resolved spectrum for channel A and μ=5. (c-d) Same as above, but for channel B.

described in chapters 4 and 5 would reduce total acquisition time for such an experiment by a factor of 27.

Increased Dimensionality through Multiple Continua

As discussed in the previous two chapters, the quantification of spectral shifts in the TRPES is a one-dimensional measurement and can therefore only be used to extract signatures of an evolving vibrational wavepacket if the motion is limited to (or at least dominated by) one nuclear degree of freedom. In ethylene, the torsion mode is found to dominate on the sub-10 fs time scale. In methanol, a new coordinate involving simultaneous C–O bond stretching and C–O–H bond angle opening had to be defined to describe the reaction pathway towards a conical intersection. However, even if motion along other coordinates plays a limited but non-

negligible role, it was found that, at least near the Franck-Condon region, the close energetic tracking of the initially excited S_2 and cation state reached through photoionization along the O–H bond length and C–O–H bond angle coordinates allowed to follow the vibrational wavepacket along the C–O coordinate.

Extension of this method to higher degrees of freedom is possible by making use of multiple ionization continua. The electron binding energy, as defined in this text, depends on the geometry dependent cation state energy. Using photons with higher energy to ionize the evolving excited state could give access to excited states of the cation, which would lead to additional binding energy measurements. As an example, the first two binding energies in methanol are shown in fig. 6.4. As previously seen, the 1^{st} binding energy corresponding to ionization to the ground state of the cation reveals information about the C–O bond length while being mostly insensitive to the O–H bond length and C–O–H bond angles. However, the 2^{nd} binding energy, corresponding to ionization to the first excited state of the cation, has a strong dependence on the C–O–H bond angle. While there is also a dependence on the C–O bond length, simultaneous measurements of both of these binding energies using a high energy photon now becomes a two-dimensional measurement which can be properly mapped to a two-dimensional (C–O bond length and C–O–H bond angle) nuclear geometry.

Although there are limitations, including the large variation in cross-sections expected for ionization to different ionic continua and the photon source itself, this method can be pushed much beyond two dimensions as we can expect at least $n_{e^-}/2$ ionic states to be directly accessible in the simple molecular orbital picture[38] with a high enough energy photon. Energy shifts due to the ultrafast evolution of the nuclear geometry can be expected even for core orbitals, as has been shown in several recent studies focusing on X-ray transient absorption using broadband sources rather than photoelectron spectroscopy [188, 189]. Due to their atomic localization, the use of core orbitals may actually be an advantage, as compared to valence ionization, for observing changes in nuclear geometry [190]. Monitoring of the concerted shifts of several photoelectron and/or absorption peaks can lead to an accurate movie of the highly dimensional evolving vibrational wavepacket alongside that of the electronic excitation.

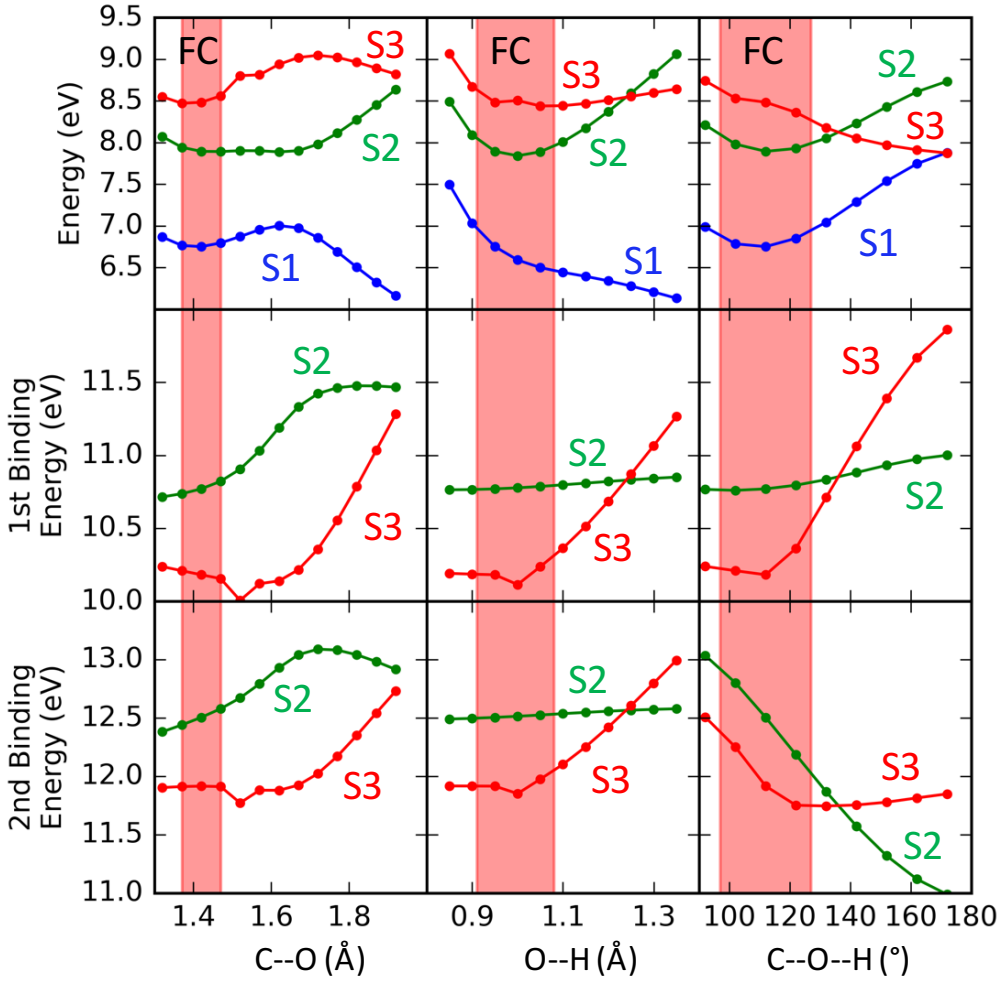

Figure 6.4: **Second Binding Energy in Methanol.** The state energies (top) as well as the first (center) and second (bottom) binding energies, corresponding to ionization to the ground and first excited state of the cation, respectively, are shown for the first three singlet excited states of methanol along the C–O (left) and O–H (center) bond and C–O–H (right) bond angle coordinates. The pink shaded area indicate the Franck-Condon region along each coordinate. The first and second binding energies have different dependences on the nuclear geometry and the simultaneous measurement of both could make it possible to resolve the nuclear wavepacket in two dimensions instead of one. The calculations were done as described in fig. 5.2.

Bibliography

[1] International Energy Agency. *Key world energy statistics*. International Energy Agency, 2015.

[2] M. Wackernagel et al. "Tracking the ecological overshoot of the human economy". In: *Proceedings of the national Academy of Sciences* 99.14 (2002), pp. 9266–9271.

[3] D. A. Bryant and N.-U. Frigaard. "Prokaryotic photosynthesis and phototrophy illuminated". In: *Trends in microbiology* 14.11 (2006), pp. 488–496.

[4] S. Styring. "Artificial photosynthesis for solar fuels". In: *Faraday discussions* 155 (2012), pp. 357–376.

[5] G. A. Olah. "Beyond oil and gas: the methanol economy". In: *Angewandte Chemie International Edition* 44.18 (2005), pp. 2636–2639.

[6] R. W. Schoenlein, L. A. Peteanu, et al. "The first step in vision: femtosecond isomerization of rhodopsin". In: *Science* 254.5030 (1991), p. 412.

[7] N. J. Tro. *Principles of chemistry: a molecular approach*. Pearson, 2015.

[8] H. Eyring and M. Polanyi. "Uber einfache gasreaktionen". In: *Z Phys Chem Abt B* 12 (1931), pp. 279–311.

[9] E. Wigner. "The transition state method". In: *Transactions of the Faraday Society* 34 (1938), pp. 29–41.

[10] W. Kohn. "Nobel Lecture: Electronic structure of matter-wave functions and density functionals". In: *Reviews of Modern Physics* 71.5 (1999), p. 1253.

[11] C. C.J. Roothaan. "New developments in molecular orbital theory". In: *Reviews of modern physics* 23.2 (1951), p. 69.

[12] G. G. Hall. "The molecular orbital theory of chemical valency. VIII. A method of calculating ionization potentials". In: *Proceedings of the Royal Society of London A: Mathematical, Physical and Engineering Sciences*. Vol. 205. 1083. The Royal Society. 1951, pp. 541–552.

[13] C. C.J. Roothaan. "Self-consistent field theory for open shells of electronic systems". In: *Reviews of modern physics* 32.2 (1960), p. 179.

[14] C. D. Sherrill and H. F. Schaefer. "The configuration interaction method: Advances in highly correlated approaches". In: *Advances in quantum chemistry* 34 (1999), pp. 143–269.

[15] M. E. Casida and M. Huix-Rotllant. "Progress in time-dependent density-functional theory". In: *Annual review of physical chemistry* 63 (2012), pp. 287–323.

[16] A. I. Krylov. "Equation-of-motion coupled-cluster methods for open-shell and electronically excited species: The hitchhiker's guide to Fock space". In: *Annual Review of Physical Chemistry* 59 (2008).

[17] M. W. Schmidt et al. "General atomic and molecular electronic structure system". In: *Journal of computational chemistry* 14.11 (1993), pp. 1347–1363.

[18] D. J. Tannor. *Introduction to quantum mechanics: a time-dependent perspective*. University Science Books, 2007.

[19] L. D. Landau. "Zur theorie der energieubertragung. II". In: *Phys. Z. Sowjetunion* 2.46 (1932), pp. 1–13.

[20] C. Zener. "Non-adiabatic crossing of energy levels". In: *Proceedings of the Royal Society of London A: Mathematical, Physical and Engineering Sciences*. Vol. 137. 833. The Royal Society. 1932, pp. 696–702.

[21] D. R. Yarkony. "Diabolical conical intersections". In: *Reviews of Modern Physics* 68.4 (1996), p. 985.

[22] H. A. Jahn and E. Teller. "Stability of polyatomic molecules in degenerate electronic states. I. Orbital degeneracy". In: *Proceedings of the Royal Society of London A: Mathematical, Physical and Engineering Sciences*. Vol. 161. 905. The Royal Society. 1937, pp. 220–235.

[23] E. Teller. "The Crossing of Potential Surfaces." In: *Journal of Physical Chemistry* 41.1 (1937), pp. 109–116.

[24] D. R. Yarkony. "Conical intersections: The new conventional wisdom". In: *The Journal of Physical Chemistry A* 105.26 (2001), pp. 6277–6293.

[25] B. G. Levine and T. J. Martinez. "Isomerization through conical intersections". In: *Annu. Rev. Phys. Chem.* 58 (2007), pp. 613–634.

[26] C. E. Crespo-Hernández et al. "Ultrafast excited-state dynamics in nucleic acids". In: *Chemical reviews* 104.4 (2004), pp. 1977–2020.

[27] A. Zewail. "Laser femtochemistry". In: *Science* 242.4886 (1988), pp. 1645–1653.

[28] R. Berera, R. van Grondelle, and J. T.M. Kennis. "Ultrafast transient absorption spectroscopy: principles and application to photosynthetic systems". In: *Photosynthesis research* 101.2-3 (2009), pp. 105–118.

[29] J. L. McHale. *Molecular spectroscopy*. CRC Press, 2017.

[30] J. Berkowitz. *Photoabsorption, photoionization, and photoelectron spectroscopy*. Academic Press, 2012.

[31] A. Stolow, A. E. Bragg, and D. M. Neumark. "Femtosecond time-resolved photoelectron spectroscopy". In: *Chemical reviews* 104.4 (2004), pp. 1719–1758.

[32] D. R. Cyr and C. C. Hayden. "Femtosecond time-resolved photoionization and photoelectron spectroscopy studies of ultrafast internal conversion in 1, 3, 5-hexatriene". In: *The Journal of chemical physics* 104.2 (1996), pp. 771–774.

[33] V. Blanchet et al. "Discerning vibronic molecular dynamics using time-resolved photoelectron spectroscopy". In: *Nature* 401.6748 (1999), p. 52.

[34] S. Ullrich et al. "Electronic relaxation dynamics in DNA and RNA bases studied by time-resolved photoelectron spectroscopy". In: *Physical Chemistry Chemical Physics* 6.10 (2004), pp. 2796–2801.

[35] O. Schalk, A. E. Boguslavskiy, and A. Stolow. "Substituent effects on dynamics at conical intersections: Cyclopentadienes". In: *The Journal of Physical Chemistry A* 114.12 (2010), pp. 4058–4064.

[36] R. Spesyvtsev et al. "Excited-state dynamics of furan studied by sub-20-fs time-resolved photoelectron imaging using 159-nm pulses". In: *The Journal of chemical physics* 143.1 (2015), p. 014302.

[37] S. Adachi, M. Sato, and T. Suzuki. "Direct observation of ground-state product formation in a 1, 3-cyclohexadiene ring-opening reaction". In: *The journal of physical chemistry letters* 6.3 (2015), pp. 343–346.

[38] T. Koopmans. "Über die Zuordnung von Wellenfunktionen und Eigenwerten zu den einzelnen Elektronen eines Atoms". In: *Physica* 1.1-6 (1934), pp. 104–113.

[39] S. Lochbrunner et al. "Methods and applications of femtosecond time-resolved photoelectron spectroscopy". In: *Journal of Electron Spectroscopy and Related Phenomena* 112.1 (2000), pp. 183–198.

[40] U. Liebl et al. "Ultrafast ligand rebinding in the heme domain of the oxygen sensors FixL and Dos: general regulatory implications for heme-based sensors". In: *Proceedings of the National Academy of Sciences* 99.20 (2002), pp. 12771–12776.

[41] C. Slavov et al. "Ultrafast coherent oscillations reveal a reactive mode in the ring-opening reaction of fulgides". In: *Physical Chemistry Chemical Physics* 17.21 (2015), pp. 14045–14053.

[42] P. Hockett et al. "Probing ultrafast dynamics with time-resolved multi-dimensional coincidence imaging: butadiene". In: *Journal of Modern Optics* 60.17 (2013), pp. 1409–1425.

[43] H. Marciniak and S. Lochbrunner. "On the interpretation of decay associated spectra in the presence of time dependent spectral shifts". In: *Chemical Physics Letters* 609 (2014), pp. 184–188.

[44] M. H. Elkins, H. L. Williams, and D. M. Neumark. "Isotope effect on hydrated electron relaxation dynamics studied with time-resolved liquid jet photoelectron spectroscopy". In: *The Journal of chemical physics* 144.18 (2016), p. 184503.

[45] H. R. Hudock et al. "Ab initio molecular dynamics and time-resolved photoelectron spectroscopy of electronically excited uracil and thymine". In: *The Journal of Physical Chemistry A* 111.34 (2007), pp. 8500–8508.

[46] Y.-I. Suzuki et al. "Time-resolved photoelectron imaging of $S_2 \rightarrow S_1$ internal conversion in benzene and toluene". In: *The Journal of chemical physics* 134.18 (2011), p. 184313.

[47] T. Fuji et al. "Excited-State Dynamics of CS_2 Studied by Photoelectron Imaging with a Time Resolution of 22 fs". In: *Chemistry–An Asian Journal* 6.11 (2011), pp. 3028–3034.

[48] T. Horio et al. "Full observation of ultrafast cascaded radiationless transitions from S_2 ($\pi\pi^*$) state of pyrazine using vacuum ultraviolet photoelectron imaging". In: *The Journal of chemical physics* 145.4 (2016), p. 044306.

[49] S. B. King et al. "Time-resolved radiation chemistry: Dynamics of electron attachment to uracil following UV excitation of iodide-uracil complexes". In: *The Journal of chemical physics* 141.22 (2014), p. 224310.

[50] T. Kobayashi, T. Horio, and T. Suzuki. "Ultrafast Deactivation of the $\pi\pi^*$(V) State of Ethylene Studied Using Sub-20 fs Time-Resolved Photoelectron Imaging". In: *The Journal of Physical Chemistry A* 119.36 (2015), pp. 9518–9523.

[51] E. G. Champenois et al. "Involvement of a low-lying Rydberg state in the ultrafast relaxation dynamics of ethylene". In: *The Journal of chemical physics* 144.1 (2016), p. 014303.

[52] A. E. Siegman. *Lasers*. University Science Books, 1986.

[53] R. W. Boyd. *Nonlinear optics*. Academic press, 2003.

[54] C. Spielmann et al. "Generation of coherent X-rays in the water window using 5-femtosecond laser pulses". In: *Science* 278.5338 (1997), pp. 661–664.

[55] T. Brabec and F. Krausz. "Intense few-cycle laser fields: Frontiers of nonlinear optics". In: *Reviews of Modern Physics* 72.2 (2000), p. 545.

[56] P. A. Franken et al. "Generation of optical harmonics". In: *Physical Review Letters* 7.4 (1961), p. 118.

[57] M. V. Ammosov, N. B. Delone, and V. P. Krainov. "Tunnelling ionization of complex atoms and of atomic ions in an alternating electromagnetic field". In: *Journal of Experimental and Theoretical Physics* 64.6 (1986), pp. 1191–1194.

[58] L. V. Keldysh et al. "Ionization in the field of a strong electromagnetic wave". In: *Sov. Phys. JETP* 20.5 (1965), pp. 1307–1314.

[59] P. H. Bucksbaum et al. "Role of the ponderomotive potential in above-threshold ionization". In: *Journal of the Optical Society of America B Optical Physics* 4.5 (1987), pp. 760–764.

[60] A. McPherson et al. "Studies of multiphoton production of vacuum-ultraviolet radiation in the rare gases". In: *Journal of the Optical Society of America B Optical Physics* 4.4 (1987), pp. 595–601.

[61] J. L. Krause, K. J. Schafer, and K. C. Kulander. "High-order harmonic generation from atoms and ions in the high intensity regime". In: *Physical Review Letters* 68.24 (1992), p. 3535.

[62] P. B. Corkum. "Plasma perspective on strong field multiphoton ionization". In: *Physical Review Letters* 71.13 (1993), p. 1994.

[63] A. Baltuška et al. "Attosecond control of electronic processes by intense light fields". In: *Nature* 421.6923 (2003), pp. 611–615.

[64] Z. Chang. *Fundamentals of Attosecond Optics*. Taylor & Francis, 2011.

[65] M. Lewenstein et al. "Theory of high-harmonic generation by low-frequency laser fields". In: *Physical Review A* 49.3 (1994), p. 2117.

[66] P. Balcou et al. "Generalized phase-matching conditions for high harmonics: The role of field-gradient forces". In: *Physical Review A* 55.4 (1997), p. 3204.

[67] E. Constant et al. "Optimizing high harmonic generation in absorbing gases: Model and experiment". In: *Physical Review Letters* 82.8 (1999), p. 1668.

[68] D. C. Yost et al. "Vacuum-ultraviolet frequency combs from below-threshold harmonics". In: *Nature Physics* 5.11 (2009), pp. 815–820.

[69] R. R. Freeman et al. "Above-threshold ionization with subpicosecond laser pulses". In: *Physical review letters* 59.10 (1987), p. 1092.

[70] P. Balcou and A. L Huillier. "Phase-matching effects in strong-field harmonic generation". In: *Physical Review A* 47.2 (1993), p. 1447.

[71] J. A. Hostetter et al. "Semiclassical approaches to below-threshold harmonics". In: *Physical Review A* 82.2 (2010), p. 023401.

[72] P. F. Moulton. "Spectroscopic and laser characteristics of Ti:Al_2O_3". In: *Journal of the Optical Society of America B Optical Physics* 3 (1986), pp. 125–133. DOI: 10.1364/JOSAB.3.000125.

[73] K. F. Wall and A. Sanchez. "Titanium sapphire lasers". In: *The Lincoln laboratory journal* 3.3 (1990), pp. 447–462.

[74] R. Trebino et al. "Measuring ultrashort laser pulses in the time-frequency domain using frequency-resolved optical gating". In: *Review of Scientific Instruments* 68.9 (1997), pp. 3277–3295.

[75] H. Stapelfeldt and T. Seideman. "Colloquium: Aligning molecules with strong laser pulses". In: *Reviews of Modern Physics* 75.2 (2003), p. 543.

[76] E. T.J. Nibbering et al. "Determination of the inertial contribution to the nonlinear refractive index of air, N_2, and O_2 by use of unfocused high-intensity femtosecond laser pulses". In: *Journal of the Optical Society of America B Optical Physics* 14.3 (1997), pp. 650–660.

[77] D. Clark. *Thermal Conductivity of Helium*. Tech. rep. Fermi National Accelerator Laboratory (FNAL), Batavia, IL, 1992.

[78] A. Sullivan. "Propagation of High-Intensity Ultrashort Laser Pulses in Plasmas." In: (1993).

[79] O. Kornilov, R. Wilcox, and O. Gessner. "Nanograting-based compact vacuum ultraviolet spectrometer and beam profiler for *in situ* characterization of high-order harmonic generation light sources". In: *Review of Scientific Instruments* 81.6 (2010), p. 063109.

[80] B. L. Henke, E. M. Gullikson, and J. C. Davis. *X-ray interactions-photoabsorption, scattering, transmission and reflection at E= 50-30,000 eV, Z= 1-92*. 1993.

[81] E. Allaria et al. "Highly coherent and stable pulses from the FERMI seeded free-electron laser in the extreme ultraviolet". In: *Nature Photonics* 6.10 (2012), pp. 699–704.

[82] S. Ackermann et al. "Generation of coherent 19-and 38-nm radiation at a free-electron laser directly seeded at 38 nm". In: *Physical review letters* 111.11 (2013), p. 114801.

[83] L. Poletto, Paolo Villoresi, and Fabio Frassetto. "Diffraction gratings for the selection of ultrashort pulses in the extreme-ultraviolet". In: *Advances in Solid State Lasers Development and Applications*. InTech, 2010.

[84] T. K. Allison et al. "Separation of high order harmonics with fluoride windows". In: *Optics express* 17.11 (2009), pp. 8941–8946.

[85] K. A. Larsen et al. "VUV and XUV reflectance of optically coated mirrors for selection of high harmonics". In: *Optics express* 24.16 (2016), pp. 18209–18216.

[86] J. I. Larruquert and R. A.M. Keski-Kuha. "Multilayer coatings with high reflectance in the extreme-ultraviolet spectral range of 50 to 121.6 nm". In: *Applied optics* 38.7 (1999), pp. 1231–1236.

[87] M. Vidal-Dasilva et al. "Electron-beam deposited boron coatings for the extreme ultraviolet". In: *Applied optics* 47.16 (2008), pp. 2926–2930.

[88] T. K. Allison et al. "Ultrafast internal conversion in ethylene. II. Mechanisms and pathways for quenching and hydrogen elimination". In: *The Journal of chemical physics* 136.12 (2012), p. 124317.

[89] M. Kurka et al. "Two-photon double ionization of Ne by free-electron laser radiation: a kinematically complete experiment". In: *Journal of Physics B: Atomic, Molecular and Optical Physics* 42.14 (2009), p. 141002.

[90] B. Manschwetus et al. "Two-photon double ionization of neon using an intense attosecond pulse train". In: *Physical Review A* 93.6 (2016), p. 061402.

[91] U. Fano. "Effects of configuration interaction on intensities and phase shifts". In: *Physical Review* 124.6 (1961), p. 1866.

[92] J. L. Wiza. "Microchannel plate detectors". In: *Nuclear Instruments and Methods* 162.1-3 (1979), pp. 587–601.

[93] W. C. Wiley and I. H. McLaren. "Time-of-flight mass spectrometer with improved resolution". In: *Review of Scientific Instruments* 26.12 (1955), pp. 1150–1157.

[94] C. R. Gebhardt et al. "Slice imaging: A new approach to ion imaging and velocity mapping". In: *Review of Scientific Instruments* 72.10 (2001), pp. 3848–3853.

[95] D. Townsend, M. P. Minitti, and A. G. Suits. "Direct current slice imaging". In: *Review of scientific instruments* 74.4 (2003), pp. 2530–2539.

[96] O. Jagutzki et al. "Fast position and time resolved read-out of micro-channelplates with the delay-line technique for single particle and photon detection". In: *Proc. SPIE*. Vol. 3438. 1998, pp. 322–334.

[97] R. Dorner et al. "Cold target recoil ion momentum spectroscopy: a momentum microscope to view atomic collision dynamics". In: *Physics Reports* 330.2 (2000), pp. 95–192.

[98] A. T.J.B. Eppink and D. H. Parker. "Velocity map imaging of ions and electrons using electrostatic lenses: Application in photoelectron and photofragment ion imaging of molecular oxygen". In: *Review of Scientific Instruments* 68.9 (1997), pp. 3477–3484.

[99] T. W. Wright. *Ultrafast Molecular Dynamics Studied with Vacuum Ultraviolet Pulses*. University of California, Davis, 2015.

[100] G. A. Garcia, L. Nahon, and I. Powis. "Two-dimensional charged particle image inversion using a polar basis function expansion". In: *Review of Scientific Instruments* 75.11 (2004), pp. 4989–4996.

[101] D. A. Dahl, J. E. Delmore, and A. D. Appelhans. "SIMION PC/PS2 electrostatic lens design program". In: *Review of Scientific Instruments* 61.1 (1990), pp. 607–609.

[102] J. Cooper and R. N. Zare. "Angular distribution of photoelectrons". In: *The Journal of Chemical Physics* 48.2 (1968), pp. 942–943.

[103] P. Hockett et al. "Time-resolved imaging of purely valence-electron dynamics during a chemical reaction". In: *Nature Physics* 7.8 (2011), p. 612.

[104] E. Hecht. "Optics". In: *Addison Wesley* 997 (1998), pp. 213–214.

[105] S. Behnel et al. "Cython: The Best of Both Worlds". In: *Computing in Science Engineering* 13.2 (2011), pp. 31–39. ISSN: 1521-9615. DOI: 10.1109/MCSE.2010.118.

[106] N. Shivaram et al. "Focal overlap gating in velocity map imaging to achieve high signal-to-noise ratio in photo-ion pump-probe experiments". In: *Applied Physics Letters* 109.25 (2016), p. 254101.

[107] P. Agostini et al. "Free-free transitions following six-photon ionization of xenon atoms". In: *Physical Review Letters* 42.17 (1979), p. 1127.

[108] T. E.H. Walker and J. T. Waber. "Spin-orbit coupling photoionization". In: *Journal of Physics B: Atomic and Molecular Physics* 7.6 (1974), p. 674.

[109] J. von Neumann and E. P. Wigner. "Über das Verhalten von Eigenwerten bei adiabatischen Prozessen". In: *The Collected Works of Eugene Paul Wigner*. Springer, 1993, pp. 294–297.

[110] P. G. Wilkinson and R. S. Mulliken. "Far Ultraviolet Absorption Spectra of Ethylene and Ethylene-d 4". In: *The Journal of Chemical Physics* 23.10 (1955), pp. 1895–1907.

[111] A. J. Merer and R. S. Mulliken. "Ultraviolet spectra and excited states of ethylene and its alkyl derivatives". In: *Chemical Reviews* 69.5 (1969), pp. 639–656.

[112] Z. Lin, S. Zhong, and D. Grierson. "Recent advances in ethylene research". In: *Journal of experimental botany* 60.12 (2009), pp. 3311–3336.

[113] Intratec. *Propylene Production from Methanol*. Intratec Solutions, 2012. ISBN: 0615648118.

[114] A. B. Callear and R. J. Cvetanović. "Isotopic Effects and Collisional Deactivation in the Mercury Photosensitized Decomposition of Ethylene". In: *The Journal of Chemical Physics* 24.4 (1956), pp. 873–878.

[115] M. C. Sauer Jr. and L. M. Dorfman. "Molecular detachment processes in the vacuum UV photolysis of gaseous hydrocarbons. I. Ethylene. II. Butane". In: *The Journal of Chemical Physics* 35.2 (1961), pp. 497–502.

[116] H. Okabe and J. R. McNesby. "Vacuum Ultraviolet Photochemistry. II. Photolysis of Ethylene". In: *The Journal of Chemical Physics* 36.3 (1962), pp. 601–604.

[117] P. Ausloos and R. Gorden Jr. "Hydrogen Formation in the γ Radiolysis of Ethylene". In: *The Journal of Chemical Physics* 36.1 (1962), pp. 5–9.

[118] R. A. Back and D. W.L. Griffiths. "Flash photolysis of ethylene". In: *The Journal of Chemical Physics* 46.12 (1967), pp. 4839–4843.

[119] H. Hara and I. Tanaka. "Photolysis of Ethylene at 1634 Å and 1849 Å". In: *Bulletin of the Chemical Society of Japan* 46.10 (1973), pp. 3012–3015.

[120] H. Hara and I. Tanaka. "Energized Vinyl Radical Formation in the Photolysis of Ethylene". In: *Bulletin of the Chemical Society of Japan* 47.6 (1974), pp. 1543–1544.

[121] B. A. Balko, J. Zhang, and Y. T. Lee. "Photodissociation of ethylene at 193 nm". In: *The Journal of Chemical Physics* 97.2 (1992), pp. 935–942.

[122] E. F. Cromwell et al. "Dynamics of ethylene photodissociation from rovibrational and translational energy distributions of H_2 products". In: *The Journal of chemical physics* 97.6 (1992), pp. 4029–4040.

[123] J. J. Lin et al. "Site-specific dissociation dynamics of ethylene at 157 nm: Atomic and molecular hydrogen elimination". In: *The Journal of Chemical Physics* 113.21 (2000), pp. 9668–9677.

[124] S.-H. Lee, Y. T. Lee, and X. Yang. "Dynamics of photodissociation of ethylene and its isotopomers at 157 nm: Branching ratios and kinetic-energy distributions". In: *The Journal of chemical physics* 120.23 (2004), pp. 10983–10991.

[125] R. J. Buenker, V. Bonačić-Koutecký, and L. Pogliani. "Potential energy and dipole moment surfaces for simultaneous torsion and pyramidalization of ethylene in its lowest-lying singlet excited states: A CI study of the sudden polarization effect". In: *The Journal of Chemical Physics* 73.4 (1980), pp. 1836–1849.

[126] J. H. Jensen, K. Morokuma, and M. S. Gordon. "Pathways for H2 elimination from ethylene: A theoretical study". In: *The Journal of chemical physics* 100.3 (1994), pp. 1981–1987.

[127] A. H.H. Chang et al. "Ab initio calculations of potential energy surface and rate constants for ethylene photodissociation at 193 and 157 nm". In: *Chemical physics letters* 287.3 (1998), pp. 301–306.

[128] M. Ben-Nun, J. Quenneville, and T. J. Martinez. "Ab initio multiple spawning: Photochemistry from first principles quantum molecular dynamics". In: *The Journal of Physical Chemistry A* 104.22 (2000), pp. 5161–5175.

[129] H. Tao, B. G. Levine, and T. J. Martinez. "Ab initio multiple spawning dynamics using multi-state second-order perturbation theory". In: *The Journal of Physical Chemistry A* 113.49 (2009), pp. 13656–13662.

[130] M. Barbatti et al. "Semiempirical molecular dynamics investigation of the excited state lifetime of ethylene". In: *Chemical physics letters* 401.1 (2005), pp. 276–281.

[131] M. Barbatti, M. Ruckenbauer, and H. Lischka. "The photodynamics of ethylene: A surface-hopping study on structural aspects". In: *The Journal of chemical physics* 122.17 (2005), p. 174307.

[132] P. Farmanara, V. Stert, and W. Radloff. "Ultrafast internal conversion and fragmentation in electronically excited C_2H_4 and C_2H_3Cl molecules". In: *Chemical physics letters* 288.2 (1998), pp. 518–522.

[133] P. Farmanara et al. "Ultrafast internal conversion and photodissociation of molecules excited by femtosecond 155 nm laser pulses". In: *The Journal of chemical physics* 111.14 (1999), pp. 6264–6270.

[134] J. M. Mestdagh et al. "Prereactive evolution of monoalkenes excited in the 6 eV region". In: *The Journal of Chemical Physics* 113.1 (2000), pp. 237–248.

[135] H. Tao et al. "Ultrafast internal conversion in ethylene. I. The excited state lifetime". In: *The Journal of chemical physics* 134.24 (2011), p. 244306.

[136] V. Stert et al. "Femtosecond time-resolved dynamics of the electronically excited ethylene molecule". In: *Chemical physics letters* 388.1 (2004), pp. 144–149.

[137] K. Kosma et al. "Ultrafast dynamics and coherent oscillations in ethylene and ethylene-d 4 excited at 162 nm". In: *The Journal of Physical Chemistry A* 112.33 (2008), pp. 7514–7529.

[138] B. H. Bransden and C. J. Joachain. *Quantum mechanics*. Pearson Education, 2000.

[139] G. Herzberg. "The ionization potential of CH_2". In: *Canadian Journal of Physics* 39.10 (1961), pp. 1511–1513.

[140] K. M. Ervin et al. "Bond strengths of ethylene and acetylene". In: *Journal of the American Chemical Society* 112.15 (1990), pp. 5750–5759.

[141] H. Shiromaru et al. "Determination of the carbon-hydrogen bond dissociation energies of ethylene and acetylene by observation of the threshold energies of proton formation by synchrotron radiation". In: *Journal of Physical Chemistry* 91.1 (1987), pp. 17–19.

[142] R. A. Mackie et al. "A photoionization mass spectrometric study of acetylene and ethylene in the VUV spectral region". In: *International Journal of Mass Spectrometry* 223 (2003), pp. 67–79.

[143] V. Barone and S. Fliszár. "Theoretical energies of representative carbon–carbon bonds". In: *International Journal of Quantum Chemistry* 55.6 (1995), pp. 469–476.

[144] K. Alnama et al. "Neutral excited radicals formed by ethylene photodissociation in the 8–24 eV region". In: *Physical Chemistry Chemical Physics* 6.9 (2004), pp. 2093–2100.

[145] Q. Zhong, L. Poth, and A. W. Castleman Jr. "Ultrafast dissociation dynamics of acetone: A revisit to the S_1 state and 3s Rydberg state". In: *The Journal of chemical physics* 110.1 (1999), pp. 192–196.

[146] C. P. Schick and P. M. Weber. "Ultrafast dynamics in superexcited states of phenol". In: *The Journal of Physical Chemistry A* 105.15 (2001), pp. 3725–3734.

[147] R. A. Rijkenberg and W. J. Buma. "High-resolution excited-state photoelectron spectroscopy of the lower Rydberg states of jet-cooled C_2H_4 and C_2D_4". In: *The Journal of Physical Chemistry A* 106.15 (2002), pp. 3727–3737.

[148] K. Alnama et al. "Excited states of C_2H_4 studied by (3+1) and (3+2) REMPI spectroscopy: disentangling the lowest Rydberg series from the strong π–π^* V←N transition". In: *Molecular Physics* 105.11-12 (2007), pp. 1743–1756.

[149] M. Barbatti, J. Paier, and H. Lischka. "Photochemistry of ethylene: A multireference configuration interaction investigation of the excited-state energy surfaces". In: *The Journal of chemical physics* 121.23 (2004), pp. 11614–11624.

[150] T. Mori et al. "Role of Rydberg states in the photochemical dynamics of ethylene". In: *The Journal of Physical Chemistry A* 116.11 (2012), pp. 2808–2818.

[151] B. Sellner et al. "Ultrafast non-adiabatic dynamics of ethylene including Rydberg states". In: *Molecular Physics* 111.16-17 (2013), pp. 2439–2450.

[152] W. H. Miller and B. M.D.D. Jansen op de Haar. "A new basis set method for quantum scattering calculations". In: *The Journal of chemical physics* 86.11 (1987), pp. 6213–6220.

[153] D. M.P. Holland et al. "A photoabsorption, photodissociation and photoelectron spectroscopy study of C_2H_4 and C_2D_4". In: *Chemical physics* 219.1 (1997), pp. 91–116.

[154] D. Khuseynov et al. "Photoelectron angular distributions for states of any mixed character: An experiment-friendly model for atomic, molecular, and cluster anions". In: *The Journal of chemical physics* 141.12 (2014), p. 124312.

[155] G. Wu et al. "Ultrafast non-adiabatic dynamics of methyl substituted ethylenes: The π 3s Rydberg state". In: *The Journal of chemical physics* 135.16 (2011), p. 164309.

[156] S. Oesterling et al. "Substituent effects on the relaxation dynamics of furan, furfural and β-furfural: a combined theoretical and experimental approach". In: *Physical Chemistry Chemical Physics* 19.3 (2017), pp. 2025–2035.

[157] T. Geng et al. "Dynamics in higher lying excited states: Valence to Rydberg transitions in the relaxation paths of pyrrole and methylated derivatives". In: *The Journal of Chemical Physics* 146.14 (2017), p. 144307.

[158] T. Freudenberg et al. "Ultrafast Fragmentation AND Ionisation Dynamics in Ammonia Clusters". In: *Editor I* (1996), p. 255.

[159] J. Kothandaraman et al. "Conversion of CO_2 from air into methanol using a polyamine and a homogeneous ruthenium catalyst". In: *Journal of the American Chemical Society* 138.3 (2016), pp. 778–781.

[160] B.-M. Cheng et al. "Experimental and theoretical studies on vacuum ultraviolet absorption cross sections and photodissociation of CH_3OH, CH_3OD, CD_3OH, and CD_3OD". In: *The Journal of chemical physics* 117.4 (2002), pp. 1633–1640.

[161] R. J. Buenker et al. "Photolysis of methanol at 185 nm. Quantum-mechanical calculations and product study". In: *Journal of the American Chemical Society* 106.16 (1984), pp. 4362–4368.

[162] C. C. Marston et al. "Product selectivity of vibrationally mediated photofragmentation of methanol". In: *The Journal of Chemical Physics* 98.6 (1993), pp. 4718–4727.

[163] S. Harich et al. "Photodissociation dynamics of methanol at 157 nm". In: *The Journal of Physical Chemistry A* 103.49 (1999), pp. 10324–10332.

[164] S.-H. Lee, H.-I. Lee, and Y. T. Lee. "Distributions of angular anisotropy and kinetic energy of products from the photodissociation of methanol at 157 nm". In: *The Journal of chemical physics* 121.22 (2004), pp. 11053–11059.

[165] L. J. Rogers et al. "Photolysis of CH_3SH and H_2S at 243.1 nm studied by photofragment ion imaging". In: *Journal of the Chemical Society, Faraday Transactions* 92.24 (1996), pp. 5181–5183.

[166] J. G. Izquierdo et al. "Velocity map imaging study of the photodissociation of CH_3SH: Internal energy distribution of the SH fragment". In: *ChemPhysChem* 7.8 (2006), pp. 1682–1686.

[167] G. A. Amaral et al. "Imaging the photodissociation of CH_3SH in the first and second absorption bands: The CH_3 ($\tilde{X}^2A_1$) + SH ($X^2\Pi$) channel". In: *The Journal of chemical physics* 126.2 (2007), p. 024301.

[168] Z. Chen et al. "Imaging CH_3SH photodissociation at 204 nm: the SH + CH_3 channel". In: *Physical Chemistry Chemical Physics* 13.18 (2011), pp. 8531–8536.

[169] D. R. Yarkony. "On the role of conical intersections of two potential energy surfaces of the same symmetry in photodissociation. I. $CH_3SH \rightarrow CH_3S$ + H and CH_3 + SH". In: *The Journal of chemical physics* 100.5 (1994), pp. 3639–3644.

[170] E. G. Champenois et al. "Non-adiabatic femtosecond scale dynamics of neutral excited methanol with super-resolution time-resolved photoelectron spectroscopy". Manuscript in preparation. 2017.

[171] E. G. Champenois et al. "Onset Times in Time-Resolved Photoelectron Spectra to Measure Ultrafast Non-Adiabatic Dynamics in Small Molecular Systems". In: *International Conference on Ultrafast Phenomena*. Optical Society of America. 2016, UTh4A–3.

[172] K. M.A. Refaey and W. A. Chupka. "Photoionization of the lower aliphatic alcohols with mass analysis". In: *The Journal of Chemical Physics* 48.11 (1968), pp. 5205–5219.

[173] D. Strasser, F. Goulay, and S. R. Leone. "Transient photoelectron spectroscopy of the dissociative $Br_2(^1\Pi_u)$ state". In: *The Journal of chemical physics* 127.18 (2007), p. 184305.

[174] T. W. Wright et al. "Ultrafast dynamics of the lowest-lying neutral states in carbon dioxide". In: *Physical Review A* 95.2 (2017), p. 023412.

[175] T. K. Allison. "Femtosecond Molecular Dynamics Studied With Vacuum Ultraviolet Pulse Pairs". PhD thesis. University of California, Berkeley, 2010.

[176] P. B. Corkum and F. Krausz. "Attosecond science". In: *Nature physics* 3.6 (2007), p. 381.

[177] J. Mauritsson et al. "Attosecond electron spectroscopy using a novel interferometric pump-probe technique". In: *Physical review letters* 105.5 (2010), p. 053001.

[178] S. Haessler et al. "Attosecond imaging of molecular electronic wavepackets". In: *Nature Physics* 6.3 (2010), p. 200.

[179] R. Weinkauf et al. "Nonstationary electronic states and site-selective reactivity". In: *The Journal of Physical Chemistry A* 101.42 (1997), pp. 7702–7710.

[180] F. Lépine, M. Y. Ivanov, and M. J.J. Vrakking. "Attosecond molecular dynamics: fact or fiction?" In: *Nature Photonics* 8.3 (2014), pp. 195–204.

[181] F. Calegari et al. "Ultrafast electron dynamics in phenylalanine initiated by attosecond pulses". In: *Science* 346.6207 (2014), pp. 336–339.

[182] M. Vacher et al. "Electron Dynamics upon Ionization of Polyatomic Molecules: Coupling to Quantum Nuclear Motion and Decoherence". In: *Physical Review Letters* 118.8 (2017), p. 083001.

[183] C. Arnold, O. Vendrell, and R. Santra. "Electronic decoherence following photoionization: Full quantum-dynamical treatment of the influence of nuclear motion". In: *Physical Review A* 95.3 (2017), p. 033425.

[184] D. Rolles et al. "A velocity map imaging spectrometer for electron–ion and ion–ion coincidence experiments with synchrotron radiation". In: *Nuclear Instruments and Methods in Physics Research Section B: Beam Interactions with Materials and Atoms* 261.1 (2007), pp. 170–174.

[185] A. Zhao, P. Sándor, and T. Weinacht. "Coincidence velocity map imaging using a single detector". In: *The Journal of Chemical Physics* 147.1 (2017), p. 013922.

[186] J. Mikosch and S. Patchkovskii. "Coincidence and covariance data acquisition in photoelectron and-ion spectroscopy. I. formal theory". In: *Journal of Modern Optics* 60.17 (2013), pp. 1426–1438.

[187] L. J. Frasinski. "Covariance mapping techniques". In: *Journal of Physics B: Atomic, Molecular and Optical Physics* 49.15 (2016), p. 152004.

[188] Y. Pertot et al. "Time-resolved x-ray absorption spectroscopy with a water window high-harmonic source". In: *Science* 355.6322 (2017), pp. 264–267.

[189] A. R. Attar et al. "Femtosecond x-ray spectroscopy of an electrocyclic ring-opening reaction". In: *Science* 356.6333 (2017), pp. 54–59.

[190] S. P. Neville et al. "Beyond structure: ultrafast X-ray absorption spectroscopy as a probe of non-adiabatic wavepacket dynamics". In: *Faraday discussions* 194 (2016), pp. 117–145.

Appendix A

Triatomic Hamiltonian

Armed with the potentials $V_i(\vec{R})$ found from solving the electronic Hamiltonian $H_e(\vec{r};\vec{R})$ at fixed nuclear geometries, it becomes possible to explore the nuclear part of the Hamiltonian. In this single molecule picture, working in internal coordinates is desirable. While changing from one coordinate system to the other for the potentials is simple, finding the correct expression for the kinetic energy operator is more difficult. In this appendix, we derive this operator in the internal coordinates for a triatomic system with the three internal coordinates x, y, and θ. This derivation closely follows and extends that of Marston et al. for a triatomic with a fixed inter-bond angle [162].

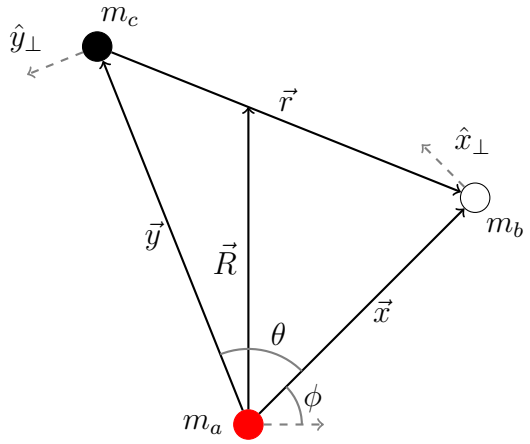

Figure A.1: **Internal and Jacobi coordinates for a triatomic system.** The Jacobi vectors $\vec{R}$ and $\vec{r}$ can be found from the internal coordinates x, y, and θ.

The nuclear kinetic energy is easily expressed in Jacobi coordinates[1] with reduced masses:

$$2T = \mu_{a,bc}|\dot{\vec{R}}|^2 + \mu_{bc}|\dot{\vec{r}}|^2, \tag{A.1}$$

[1]In this derivation, $\vec{r}$ and $\vec{R}$ represent the two Jacobi vectors of the triatomic system as opposed to the electronic and nuclear coordinate vectors as before.

where the reduced masses and Jacobi vectors are obtained from the nuclear masses and bond vectors:

$$\mu_{ij} = \frac{m_i m_j}{m_i + mj} \tag{A.2}$$

$$\mu_{i,jk} = \frac{m_i \left(m_j + m_k\right)}{m_i + m_j + m_k} \tag{A.3}$$

$$\vec{r} = \vec{x} - \vec{y} \tag{A.4}$$

$$\vec{R} = \frac{\mu_{bc}}{m_c}\vec{x} + \frac{\mu_{bc}}{m_b}\vec{y}. \tag{A.5}$$

Using these definitions, we obtain an expression for the nuclear kinetic energy in terms of the time-derivatives of the bond vectors:

$$|\dot{\vec{r}}|^2 = |\dot{\vec{x}}|^2 + |\dot{\vec{y}}|^2 - 2\dot{\vec{x}}\cdot\dot{\vec{y}} \tag{A.6}$$

$$|\dot{\vec{R}}|^2 = \left(\frac{\mu_{bc}}{m_c}\right)^2 |\dot{\vec{x}}|^2 + \left(\frac{\mu_{bc}}{m_b}\right)^2 |\dot{\vec{y}}|^2 + 2\frac{\mu_{bc}^2}{m_b m_c}\dot{\vec{x}}\cdot\dot{\vec{y}} \tag{A.7}$$

$$\begin{aligned} 2T &= \left[\mu_{a,bc}\left(\frac{\mu_{bc}}{m_c}\right)^2 + \mu_{23}\right]|\dot{\vec{x}}|^2 + \left[\mu_{a,bc}\left(\frac{\mu_{bc}}{m_b}\right)^2 + \mu_{23}\right]|\dot{\vec{y}}|^2 + 2\left[\mu_{a,bc}\frac{\mu_{bc}^2}{m_b m_c} - \mu_{23}\right]\dot{\vec{x}}\cdot\dot{\vec{y}} \\ &= \mu_{b,ac}|\dot{\vec{x}}|^2 + \mu_{c,ab}|\dot{\vec{y}}|^2 - 2\frac{\mu^2}{m_a}\dot{\vec{x}}\cdot\dot{\vec{y}} \\ &= \mu^2\left[\frac{1}{\mu_{ac}}|\dot{\vec{x}}|^2 + \frac{1}{\mu_{ab}}|\dot{\vec{y}}|^2 - \frac{1}{m_a}\dot{\vec{x}}\cdot\dot{\vec{y}}\right], \end{aligned} \tag{A.8}$$

where μ is defined such that

$$\mu^2 = \frac{m_a m_b m_c}{m_a + m_b + m_c} \left(= \mu_{i,jk}\mu_{jk}\ \forall\ i,j,k\right). \tag{A.9}$$

Next, the bond vectors can be parametrized using the internal coordinates x, y, and θ as well as the Eulerian angle ϕ orienting the molecule:

$$\vec{x} = x\hat{x},\ \vec{y} = y\hat{y} \tag{A.10}$$

$$\dot{\vec{x}} = \dot{x}\hat{x} + x\dot{\phi}\hat{x}_\perp \tag{A.11}$$

$$\dot{\vec{y}} = \dot{y}\hat{y} + y\left(\dot{\phi} + \dot{\theta}\right)\hat{y}_\perp \tag{A.12}$$

$$|\dot{\vec{x}}|^2 = \dot{x}^2 + x^2\dot{\phi}^2 \tag{A.13}$$

$$|\dot{\vec{y}}|^2 = \dot{y}^2 + y^2\left(\dot{\phi} + \dot{\theta}\right)^2 \tag{A.14}$$

$$\dot{\vec{x}}\cdot\dot{\vec{y}} = \dot{x}\dot{y}\cos\theta + \sin\theta\ \left(x\dot{y} - y\dot{x}\right) - y\sin\theta\ \dot{x}\dot{\theta} + xy\cos\theta\ \left(\dot{\phi}\dot{\theta} + \dot{\phi}^2\right). \tag{A.15}$$

With the following definitions:

$$\beta = \sin\theta,\ \alpha = \cos\theta \tag{A.16}$$

$$\Gamma(x,y) = \frac{x^2}{\mu_{ac}} + \frac{y^2}{\mu_{ab}} - \frac{2\alpha xy}{m_a} \tag{A.17}$$

$$\Omega(x,y) = y\left(\frac{\alpha x}{m_a} - \frac{y}{\mu_{ab}}\right), \tag{A.18}$$

insertion of eqs. (A.13) to (A.15) into eq. (A.8) yields

$$\begin{aligned} 2T = \mu^2\{&\frac{\dot{x}^2}{\mu_{ac}} + \frac{\dot{y}^2}{\mu_{ab}} - \frac{2\alpha}{m_a}\dot{x}\dot{y} + \Gamma(x,y)\,\dot{\phi}^2 \\ &- 2\left[\Omega(x,y)\,\dot{\theta} + \frac{\beta}{m_a}(x\dot{y} - y\dot{x})\right]\dot{\phi} + \frac{2\beta y}{m_a}\dot{x}\dot{\theta} + \frac{y^2}{\mu_{ab}}\dot{\theta}^2\}. \end{aligned} \tag{A.19}$$

Since we are interested in the internal energy, ϕ and $\dot{\phi}$ can be eliminated by setting by setting the canonical momentum associated with the molecular rotation to zero:

$$\begin{aligned} p_\phi = \frac{\partial T}{\partial \dot{\phi}} &= 0 \\ &= \Gamma(x,y,\theta)\,\dot{\phi} - \left[\Omega(x,y)\,\dot{\theta} + \frac{\beta}{m_a}(x\dot{y} - y\dot{x})\right] \end{aligned} \tag{A.20}$$

$$\dot{\phi} = \frac{\Omega(x,y)\,\dot{\theta} + \frac{\beta}{m_a}(x\dot{y} - y\dot{x})}{\Gamma(x,y,\theta)} \tag{A.21}$$

$$\begin{aligned} 2T &= \mu^2\{\frac{\dot{x}^2}{\mu_{ac}} + \frac{\dot{y}^2}{\mu_{ab}} + \frac{y^2}{\mu_{ab}}\dot{\theta}^2 - \frac{2\alpha}{m_a}\dot{x}\dot{y} + \frac{2\beta y}{m_a}\dot{x}\dot{\theta} \\ &\quad - \frac{\left[\Omega(x,y)\,\dot{\theta} + \frac{\beta}{m_a}(x\dot{y} - y\dot{x})\right]^2}{\Gamma(x,y,\theta)}\} \\ &= \mu^2\{\left(\frac{1}{\mu_{ac}} - \frac{\beta^2 y^2}{m_a^2\Gamma(x,y,\theta)}\right)\dot{x}^2 + \left(\frac{1}{\mu_{ab}} - \frac{\beta^2 x^2}{m_a^2\Gamma(x,y,\theta)}\right)\dot{y}^2 \\ &\quad + 2\left(\frac{\beta^2 xy}{m_a^2\Gamma(x,y,\theta)} - \frac{\alpha}{m_a}\right)\dot{x}\dot{y} + \left[\frac{y^2}{\mu_{ab}} - \frac{\Omega(x,y,\theta)^2}{\Gamma(x,y,\theta)}\right]\dot{\theta}^2 \\ &\quad + 2\frac{\beta y}{m_a}\left[1 + \frac{\Omega(x,y,\theta)}{\Gamma(x,y,\theta)}\right]\dot{x}\dot{\theta} - 2\frac{\beta x\Omega(x,y,\theta)}{m_a\Gamma(x,y,\theta)}\dot{y}\dot{\theta}\} \end{aligned} \tag{A.22}$$

Using a more compact notation:

$$2T = \mu^2\begin{pmatrix}\dot{x} & \dot{y} & \dot{\theta}\end{pmatrix}\begin{bmatrix}T_{xx} & T_{xy} & T_{x\theta} \\ T_{xy} & T_{yy} & T_{y\theta} \\ T_{x\theta} & T_{y\theta} & T_{\theta\theta}\end{bmatrix}\begin{pmatrix}\dot{x} \\ \dot{y} \\ \dot{\theta}\end{pmatrix}. \tag{A.23}$$

$$T_{xx} = \frac{1}{\mu_{ac}} - \frac{\beta^2 y^2}{m_a^2 \Gamma(x,y,\theta)} \tag{A.24}$$

$$T_{yy} = \frac{1}{\mu_{ab}} - \frac{\beta^2 x^2}{m_a^2 \Gamma(x,y,\theta)} \tag{A.25}$$

$$T_{\theta\theta} = \frac{y^2}{\mu_{ab}} - \frac{\Omega(x,y,\theta)^2}{\Gamma(x,y,\theta)} \tag{A.26}$$

$$T_{xy} = \frac{\beta^2 xy}{m_a^2 \Gamma(x,y,\theta)} - \frac{\alpha}{m_a} \tag{A.27}$$

$$T_{x\theta} = \frac{\beta y}{m_a}\left[1 + \frac{\Omega(x,y,\theta)}{\Gamma(x,y,\theta)}\right] \tag{A.28}$$

$$T_{y\theta} = -\frac{\beta x \Omega(x,y,\theta)}{m_a \Gamma(x,y,\theta)}. \tag{A.29}$$

For quantum mechanical calculations, we will want to express $\dot{x}$, $\dot{y}$, and $\dot{\theta}$ in terms of the canonical momenta p_i (which can in turn be replaced by $-i\hbar\partial/\partial q_i$):

$$p_i = \frac{\partial T}{\partial \dot{q}_i} \tag{A.30}$$

$$\begin{pmatrix} p_x \\ p_y \\ p_\theta \end{pmatrix} = \mu^2 \begin{bmatrix} T_{xx} & T_{xy} & T_{x\theta} \\ T_{xy} & T_{yy} & T_{y\theta} \\ T_{x\theta} & T_{y\theta} & T_{\theta\theta} \end{bmatrix} \begin{pmatrix} \dot{x} \\ \dot{y} \\ \dot{\theta} \end{pmatrix} \tag{A.31}$$

$$2T = \frac{1}{\mu^2} \begin{pmatrix} p_x & p_y & p_\theta \end{pmatrix} \begin{bmatrix} T_{xx} & T_{xy} & T_{x\theta} \\ T_{xy} & T_{yy} & T_{y\theta} \\ T_{x\theta} & T_{y\theta} & T_{\theta\theta} \end{bmatrix}^{-1} \begin{pmatrix} p_x \\ p_y \\ p_\theta \end{pmatrix}. \tag{A.32}$$

After inverting the coefficient matrix and going through some algebra:

$$2T = \begin{pmatrix} p_x & p_y & p_\theta \end{pmatrix} \begin{bmatrix} \tilde{T}_{xx} & \tilde{T}_{xy} & \tilde{T}_{x\theta} \\ \tilde{T}_{xy} & \tilde{T}_{yy} & \tilde{T}_{y\theta} \\ \tilde{T}_{x\theta} & \tilde{T}_{y\theta} & \tilde{T}_{\theta\theta} \end{bmatrix} \begin{pmatrix} p_x \\ p_y \\ p_\theta \end{pmatrix} \tag{A.33}$$

$$\tilde{T}_{xx} = \frac{1}{\mu_{ab}} \tag{A.34}$$

$$\tilde{T}_{yy} = \frac{1}{\mu_{ac}} \tag{A.35}$$

$$\tilde{T}_{\theta\theta} = \frac{\Gamma(x,y,\theta)}{x^2 y^2} \tag{A.36}$$

$$\tilde{T}_{xy} = \frac{\alpha}{m_a} \tag{A.37}$$

$$\tilde{T}_{x\theta} = -\frac{\beta}{m_a y} \tag{A.38}$$

$$\tilde{T}_{y\theta} = -\frac{\beta}{m_a x} \tag{A.39}$$

$$\begin{aligned} \frac{2}{\hbar^2}\hat{T} = &-\frac{1}{\mu_{ab}}\frac{\partial^2}{\partial x^2} - \frac{1}{\mu_{ac}}\frac{\partial^2}{\partial y^2} + \frac{\cos\theta}{m_a}\left(\frac{1}{y}\frac{\partial}{\partial x} + \frac{1}{x}\frac{\partial}{\partial y} - 2\frac{\partial^2}{\partial x \partial y}\right) \\ &+ \frac{2\sin\theta}{m_a}\left(\frac{1}{y}\frac{\partial}{\partial x} + \frac{1}{x}\frac{\partial}{\partial y} - \frac{1}{xy}\right)\frac{\partial}{\partial\theta} - \left(\frac{1}{\mu_{ab}x^2} + \frac{1}{\mu_{ac}y^2} - \frac{2\cos\theta}{m_a xy}\right)\frac{\partial^2}{\partial\theta^2} \end{aligned} \tag{A.40}$$